AMERICAN UNIVERSITY OF BEIRUT

P-Y CURVES FOR RIGID WALLS RETAINING GRANULAR
SOIL

by
IMAD WADIH EL-CHITI

A dissertation
submitted in partial fulfillment of the requirements
for the degree of Doctor in Philosophy
to the Department of Civil and Environmental Engineering
of the Faculty of Engineering and Architecture
at the American University of Beirut

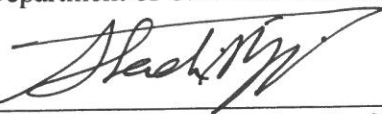Beirut, Lebanon
August 2020

# AMERICAN UNIVERSITY OF BEIRUT

## P-Y CURVES FOR RIGID WALLS RETAINING GRANULAR SOIL
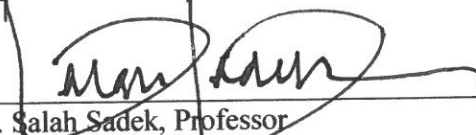
by

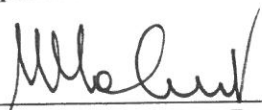## IMAD WADIH EL-CHITI

Approved by:

_____          Advisor

Dr. George Saad, Associate Professor
Department of Civil and Environmental Engineering

_____          Co-Advisor

Dr. Shadi Najjar, Associate Professor
Department of Civil and Environmental Engineering

_____          Chair of Committee

Dr. Salah Sadek, Professor
Department of Civil and Environmental Engineering

_____          Member of Committee

Dr. Mounir Mabsout, Professor
Department of Civil and Environmental Engineering

_____          Member of Committee

Dr. Jacques Harb, Professor
Department of Civil Engineering
Notre Dame University

c/o Dr FADI HAGE CHEHADE

_____          Member of Committee

Dr. Fadi Hage Chehade, Professor
Department of Civil Engineering
Lebanese University

Date of thesis/dissertation defense: September 8, 2020

AMERICAN UNIVERSITY OF BEIRUT

THESIS, DISSERTATION, PROJECT RELEASE FORM

Student Name: _Wadih_____ _El Chefi_____ _Imad_____
                    Middle                    Last                    First

○ Master's Thesis        ○ Master's Project        ⊗ Doctoral Dissertation

☐        I authorize the American University of Beirut to: (a) reproduce hard or electronic copies of my thesis, dissertation, or project; (b) include such copies in the archives and digital repositories of the University; and (c) make freely available such copies to third parties for research or educational purposes.

☒        I authorize the American University of Beirut, to: (a) reproduce hard or electronic copies of it; (b) include such copies in the archives and digital repositories of the University; and (c) make freely available such copies to third parties for research or educational purposes after:

**One ---- year from the date of submission of my thesis, dissertation, or project.**
**Two ✗ years from the date of submission of my thesis, dissertation, or project.**
**Three ---- years from the date of submission of my thesis, dissertation, or project.**

_____        _Sept 17, 2020_____
Signature                                    Date

This form is signed when submitting the thesis, dissertation, or project to the University Libraries

# ACKNOWLEDGMENTS

# AN ABSTRACT OF THE THESIS OF

Imad El Chiti     for          Doctor of Philosophy
                              Major: Civil Engineering


Title: P-Y Curves for Rigid Walls Retaining Granular Soils

The mobilization of lateral stresses behind retaining walls constitutes a typical soil structure interaction problem particularly under cyclic loading conditions. There is interest in quantifying the relationship between the lateral earth pressure and the wall displacement. One of the methods used for this purpose is the p-y method, which is widely used in the analysis of piles. Soil-structure interaction methods that are based on the p-y curves method aim at replacing the soil behind the wall by a series of springs that mimic the soil behavior. The use of p-y curves in complex numerical analyses of buildings with underground stories is gaining interest in the structural engineering community. This poses a significant challenge in relation to the selection of realistic and simplified p-y models to be used as input in the structural numerical model. This study aims at investigating lateral earth pressure behind rigid walls in the context of p-y curves. The main target is to advance knowledge of the main mechanisms that govern the p-y response of basement walls supporting granular backfill.

The objective is achieved using robust numerical and experimental tools. The numerical program entails developing active and passive p-y curves using a finite element model of a rigid wall retaining granular backfill. For the at-rest to active p-y response, the numerical results were used to derive a simplified hyperbolic p-y model for non-frictional walls and a bilinear model for the development of frictional shear stresses at the soil-wall interface. For the at-rest to passive p-y response, numerically-derived passive p-y curves were used to propose a truncated hyperbolic p-y model that is defined by a limit state passive pressure and an initial slope that is expressed using a depth-dependent soil stiffness model. Validation experiments indicated that the utilization of the proposed simple p-y models for both active and passive states provides realistic estimates of the p-y response of frictional walls supporting sands.

P-y curves were also determined using an experimental program that involved building a large-scale rectangular soil-retaining-system in the laboratory. One side of the retaining system was specifically designed to act as a rigid wall that is hinged at its bottom and free to translate horizontally at its top. Friction forces at the sidewall were carefully addressed, measured, and minimized. Pressure sensors and LVDTs were mounted on the retaining system to measure wall displacements and soil pressures. Experimental p-y curves for static and cyclic loading conditions were determined and analyzed.  The experimentally derived p-y curves were highly nonlinear and cannot be adequately represented by existing simple elastic-perfectly plastic models in the literature. More importantly, repeated cycles of loading resulted in a process of densification that affected the p-y response by significantly increasing the stiffness and maximum passive pressure after 10 loading cycles. These cyclic p-y curves are the first

in the literature and will provide the basis for future studies that target the development of p-y curves for soil-structure interaction problem involving buildings with basements.

# TABLE OF CONTEN`TS

# LIST OF ILLUSTRATIONS

xvi

# LIST OF TABLES

# CHAPTER I

# INTRODUCTION

**A. Introduction**

In its broad term, soil-structure-interaction (SSI) refers to the "static and dynamic phenomena mediated by a compliant soil and a stiffer super-structure" (Kausel 2010). SSI problems includes free-field problems (the response of soil to vibration), kinematic interaction (the response of rigid structure to ground-born waves), inertial interaction (the response of nearby soil to inertial forces of a rigid structure), and static or dynamic stiffness (the response of a soil-embedded structure subjected to static or dynamic loading).

The mobilization of lateral stresses behind rigid walls constitutes a typical soil structure interaction (SSI) problem. For structures with underground basement walls, the soil-structure-interaction between the side soil and the walls affects the response of the system, particularly under cyclic loading conditions. In the context of performance-based design, there has been interest in quantifying the relationship between the lateral earth pressure and the wall displacement. Initially, solutions for SSI problems were based on analytical approaches that aimed at producing closed-form solutions to the problem at hand. Since the 1980s, the advancement in computational power shifted the focus of current methodologies for tackling soil structure interaction problems towards finite element methods (FEM) (Randolph, 1981), boundary element methods (BEM) (Sanchez, 1982), and p-y curve methods (Boulanger et al. 1999, Allotey 2007). It is the latter method that is of concern to the research proposed in this study.

Soil-structure interaction methods that are based on the P-y curve method aim at replacing the homogeneous soil continuum by a series of springs that mimic the soil behavior adjacent to the substructure. This is shown in Figure 1.1a. For a general 3-D model, the soil response can be expressed by six uncoupled springs per node, 3 lateral and 3 rotational as shown in Figure 1.1b. However, many applications such as laterally loaded piles, rigid retaining walls, and tie back walls, can be modelled as 1-D problems with only lateral soil resistance expressed as $p_y = k_y(x).v$ .

The success and failure of this method relies heavily on the congruity between the spring stiffness and soil stiffness. Springs' stiffnesses are usually modeled using p-y curves which plots the spring force/stress (p) against the spring displacement (y). P-y curves are usually empirically derived by calibrating mathematical expressions using data from field or laboratory experiments.



(a)                                    (b)
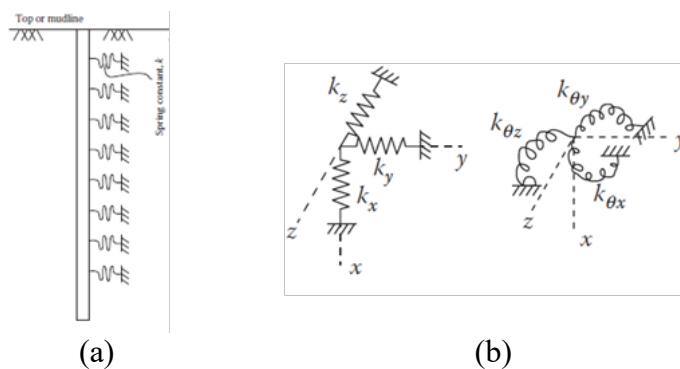
Figure 1.1 (a) Soil modeled as a series of springs (b) Six uncoupled springs defining the soil resistance for six degrees of freedom

The derived p-y model is then incorporated in a computer program for the analysis of the particular substructure. The complexity of the model is chosen based on the simplicity of the application and the tolerated error.

P-y curves have been widely used in the analysis of piles under lateral loads. However, the use of p-y curves for the analysis of rigid walls is still in its early stages. There is a need for realistic and simplified models that could describe the p-y relationship for rigid walls to be used as input in robust soil-structure-interaction problems in the context of performance-based design. The proposed dissertation aims explicitly at satisfying this need.

**B. Research Motivation**

Based on the background and literature review that will be presented in the next chapter, four techniques have been investigated for the solution of SSI problems: (1) closed-form solutions, (2) pseudo-static solutions at limit state, (3) discretization of the soil continuum into plane-strain finite elements, and (4) modeling the surrounding soil as a series of springs.

Closed-form solutions for SSI problems subjected to dynamic loading can only be found for very specific cases involving soils behaving elastically (linear) and for simple excitations as in the case of free-vibration or simple harmonic motion. However, these conditions are rarely met in practical SSI problems involving rigid walls subject to seismic excitations. In such cases, soil displacement may reach intensities beyond the 'elastic' range, forcing the soil into nonlinear behavior. Moreover, ground motion induced by seismic activities involves complex wave functions creating a very complicated problem that is mathematically unresolvable. Such conditions require the

use of numerical techniques such as FE method or finite difference in order to solve the equation of ground motion.

Pseudo-static solutions such as Mononobe-Okabe method are conceptually simple and provide a good tool for understanding pressure induced by seismic activities on rigid walls. However, this method suffers certain limitations that need to be addressed. First, it assumes that rigid walls move sufficiently to cause yielding in the retained soil. This may not be the case for massive gravity walls or basement walls braced at top and bottom. Second, all restrictions that apply for Coulomb theory apply to this method as well. M-O analysis, for example, over predicts the actual total passive thrust, for an interface friction angle exceeding half the soil friction angle.

Discretization of soil continuum into finite elements (FE) is a versatile method capable of capturing complex SSI behavior. The method has been widely investigated, validated, and vindicated. Many powerful and user-friendly finite-element packages with built-in complex soil models capable of simulating soil behavior more accurately are readily available to engineers. However, the use of FE method in SSI problems has certain drawbacks which keeps it at bay for many practicing engineers. First, the solution using FE method tends to be computationally expensive even with powerful computers and advanced simulation techniques. It is common for certain models to require a simulation time between few days to a week. Under such conditions, it becomes impractical if not impossible for practicing engineers to run a parametric study to reach an optimized solution. Second, finite element softwares with built-in complex soil models require extensive understanding of soil characterizations and behaviors. Many structural engineers are not disciplined enough in the geotechnical field to make

necessary assumptions regarding soil characterizations. This has kept the pipeline between structural department and geotechnical department in engineering firms on high demand and definitely at a heavy cost.

On the other hand, modeling soil as a series of springs presents a happy medium between the specific closed-form solutions, the overly simplified pseudo-static limit-state solutions, and the more complex time consuming FE model solutions. First, the use of non-linear springs can capture retained soil behavior under a wide range of soil deformation. Rigid retaining structures may experience small deformations as in the case of static loading or large deformation as in the case of strong ground motion. Non-linear springs can predict stresses behind the rigid retaining structure for either cases. This cannot be done in pseudo-static methods which assume an elastic or yielding soil responses. Second, contrary to FE models, adding springs to the surrounding substructure has an infinitesimal effect on simulation time. Finally, springs and spring properties are concepts that belong to the realm of structural engineering. Using springs in lieu of soil continuum releases structural engineers from the burden of meddling with geotechnical issues.

When modeling a soil continuum as a series of springs, special care should be taken in defining the spring stiffness. As stated earlier, soil is a non-linear material and its resistance varies with displacement, confinement, and relative density. It follows that a non-linear spring stiffness would be a most fitting representation of the soil behavior. In the analysis of basement walls, P-y curves noted in the literature are assumed at best bilinear. This is an over simplified assumption and a better representation of soil resistance behind rigid wall systems is warranted.

As a result, there is a need for realistic and simplified models that could describe the p-y relationship for rigid walls to be used as input in robust soil-structure-interaction problems in the context of performance-based design. Such p-y relationships could be incorporated in commercial structural analysis software in the form of non-linear springs that describe the lateral pressure versus lateral displacement relationship. This is consistent with the p-y curves concept commonly used to model the reaction of the soil for laterally loaded piles.

### C. Research Objectives

The main goal of the proposed research study is to investigate the p-y response of granular soils that are supported by rigid retaining walls over the full range of wall displacements (active to passive). This primary goal is to be reached by achieving two main objectives:

1. Investigate and determine the non-linear p-y response for granular soils supported by full-scale rigid walls using the finite element method. An expression for the backbone model is proposed that takes into account the effect of the wall height, soil properties (relative density, soil friction angle, and the modulus of elasticity), wall friction, and confinement pressure.

2. Design and construct a laboratory-scale rigid wall prototype that could be used to measure the p-y response for granular soils under static and cyclic loading conditions. The wall, having a width of 0.5m and a height of 1.2m, will be hinged at its bottom and forced into rotation using a hydraulic piston applied at its top. Pressure sensors as well as LVDT's will be installed at necessary locations to record soil stresses and wall

displacements at several depths. P-y curves for active, passive and cyclic motion will be determined, analyzed and compared to p-y curves found in literature.

## D. Research Methodology

### 1. *Numerical Modeling*

A finite element model of the rigid wall is built on PLAXIS 2D software. The FE model is comprised of an infinitely rigid wall, a half space soil continuum, an interface layer at soil/wall boundary to allow for reduced soil properties at the interface and for possible slippage, and a subgrade material. The wall is subjected to an incremental prescribed displacement. A parametric study on the following variables is conducted:

- Soil Models: Mohr Coulomb Model, Hardening Soil Model

- Mesh Sensitivity: Fine, Medium, Course and V. Course

- Height of Wall: 5, 10, and 15 meters

- Soil Properties: Loose, Medium, and Dense

- Soil-Wall Reduction Factor: 0.0, 0.6, 0.8, 1.0

- Ratio of Bottom/Top of Wall Displacement: 0%, 10% and 20%

The parametric study is repeated twice: once for the case of active wall displacement and another for the case of passive wall displacement. Lateral earth pressures at different depths of the wall, for both active and passive wall displacements, are extracted from the FE model and p-y curves are constructed. Once the p-y curves at different wall depths are extracted, a correlation between the different variables is

7

explored and normalized expressions for the prediction of active and passive p-y curves are proposed. Different shapes for the backbone curves are considered and assessed depending on their complexity and degree of precision.

## 2. *Laboratory Test*

The second part of the dissertation involves deriving the p-y curves experimentally within a lab setting. This entails characterizing the backfill material as well as building a prototype for conducting the experiment. To characterize the backfill material, the following tests are conducted:

- Sieve analysis according to ASTM C136M

- Minimum and maximum density according to ASTM D2049-69

- Specific gravity according to ASTM D792

- Soil friction angle using direct shear test ASTM D3080 - 04

- Soil friction angle at low confining pressures using consolidated drained triaxial test

- Interface friction angle between acrylic plate and sand using direct shear test

The soil-retaining-system is built from hollow steel members. One side of the retaining system is designed as a rigid wall that pivots about its bottom axis but is free to displace laterally at its top. Sensors and LVDTs are located on the system to record the pressures and displacement needed to construct the p-y response. In addition to the above the following challenges are addressed:

- Optimizing the dimensions of the retaining system whereby creating an oversized retaining system leads to difficulty in managing the experiments (storing excess amount of soil, filling and emptying the system etc.) while creating an undersized system results in unwanted backpressures in the soil.

- Designing a replicable and a reliable filling mechanism that produces a soil bed of uniform density.

- Reducing the sidewall frictional forces to minimize unjustified pressures at the rigid wall resulting from boundary constraints.

- Quantifying the residual friction forces at sidewalls,

- Creating a mechanism that facilitates the removal of the backfill material in an easy manner.

The experiments are conducted on three relative densities for the backfill material (loose, medium-dense and dense dry sand) as the rigid wall is subjected to two types of loading: static and cyclic. P-y curves are constructed experimentally and compared to the proposed models.

### E. Thesis Outline

The following paragraph describes the order of this dissertation. Chapter I is an introduction on p-y curves, research motivation and objectives, and the methodology adopted for the current research. Chapter II presents an overview of research studies reported in the technical literature. This overview includes a summary of the available p-y curve models used in the analysis of laterally loaded piles, p-y curves used in dynamic analysis, and finally p-y curves used in the analysis of rigid walls. Chapter III and Chapter IV presents a detailed study on active and passive p-y curves derived

numerically using a commercial soil-structure-interaction software. Both chapters

include a description of the FE model built on PLAXIS2D, a thorough parametric

analysis conducted through a series of numerical simulations, and finally, a proposed

expression for the predictions p-y response in term of the different parameters affecting

the response of p-y curves. Chapter V of the dissertation presents the characterization of

the backfill material used in the experimental program and a description of the soil-

retaining-system specifically fabricated for the purpose of this study. Chapter VI and

Chapter VII present the analysis and results of the conducted experiments. Chapter VI

discusses the experimentally derived p-y response for the cases of loose, medium-dense,

and dense sand when subjected to static loading, while Chapter VII discusses the results

of the experimentally derived p-y curves for medium-dense sand when subjected to

slow cyclic loading.

# CHAPTER 2

# RESEARCH BACKGROUND AND RELATED WORKS

**A. P-Y Curves in SSI Problems**

The earliest form of spring models was proposed by Winkler (Winkler, 1967). Winkler showed that a beam on soil foundation can be modeled as a beam supported by a series of independent linearly-elastic springs (Figure 2.1a & b). "The main limitation of the method is that it fails to capture the inherent non-linearity in soils due to plastic and creep strains, volume change, anisotropy, loading types, microstructural adjustments leading to degradation or softening, and healing or strengthening."

Non-linearity in the soil resistance - soil displacement relationship could be modeled using p-y curves. P-y curves can be linear lines represented by a constant stiffness '$k$' or non-linear with a varying stiffness represented by $k(x, v)$ as shown in Figure 2.2b. P-y curves are usually back-calculated from experimental or numerical data. For the case of laterally-loaded piles, fitted p-y curve models are commonly referred to as backbone curves. Different models of p-y curves with varying complexities are presented in literature. These include bilinear, polynomial, hyperbolic, and stitched models of different curves/lines (Matlock & Ripperger, 1956) (Brown, Morrison, & Reese, 1988) (Dunnavant & O'Neill, 1989) (Reese, Cox, & Koop, 1974) (Matlock & Ripperger, 1956).
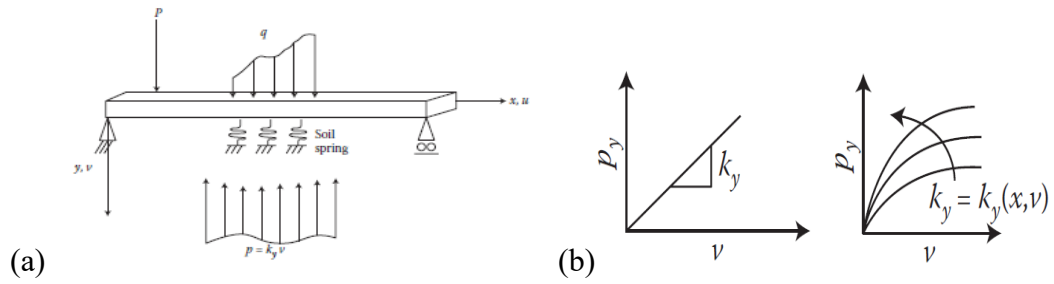
Figure 2.1 (a) Winkler's foundation model (b) generic p-y curves
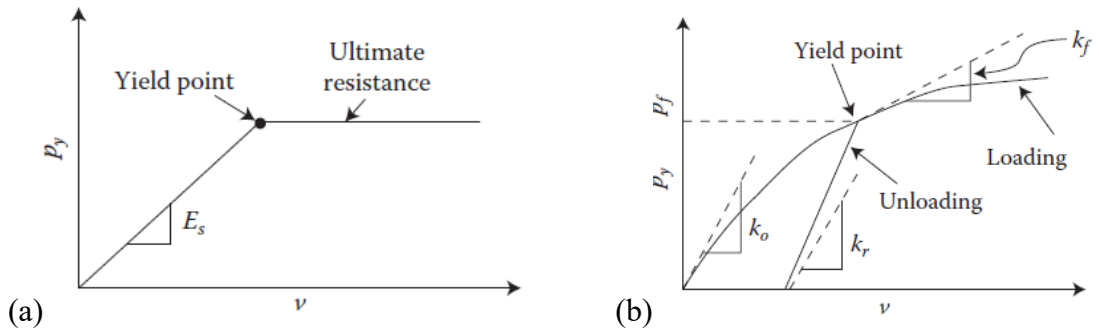


Figure 2.2 (a) typical bilinear elastic – perfectly plastic backbone curve (b) backbone curve based on nonlinear stitched models

Figure 2.2a shows an example of an elastic perfectly-plastic backbone model while Figure 2.2b shows an example of a stitched non-linear model with different loading and unloading paths.

### B. Monotonic and Slow-cyclic P-Y Curves for Piles

The analysis of piles under lateral loading is one field in geotechnical engineering that has exhausted the concept of p-y curves. In the 1970's oil companies sponsored research programs at the University of Texas to develop the analysis of piles under lateral loading. Since then, the understanding of pile behavior under lateral loads have significantly evolved and different methods have been proposed in the literature contributing to this end.

Matlock (1970) published a paper that aimed at constructing p-y curves for laterally loaded piles embedded in clayey soil. Through a series of experiments conducted on the miniature piles shown in Figure 2.3a, Matlock (1970) deduced two important soil behaviors surrounding laterally loaded piles. First, when a pile cycles between two opposite pre-selected displacements of equal magnitude, the soil resistance decreases from one cycle to another until stability is reached. The stabilized resistance constitutes an identified lower limit for soil resistance for a given displacement. Figure 2.3b shows the variation of soil resistance in a miniature pile under cyclic motion between four pre-set displacements. The dashed line in the figure represents the identified lower limit. Second, a cavity in-line with the motion of the pile known as slack zone forms within the clay forming tangential side-forces along the sides of the pile as the pile travels from one end to another. The two mentioned soil behaviors led Matlock to identify three p-y curves depending on the type of loading sustained by the pile: static, cyclic, and loading after cyclic. This is shown in Figure 2.3c.
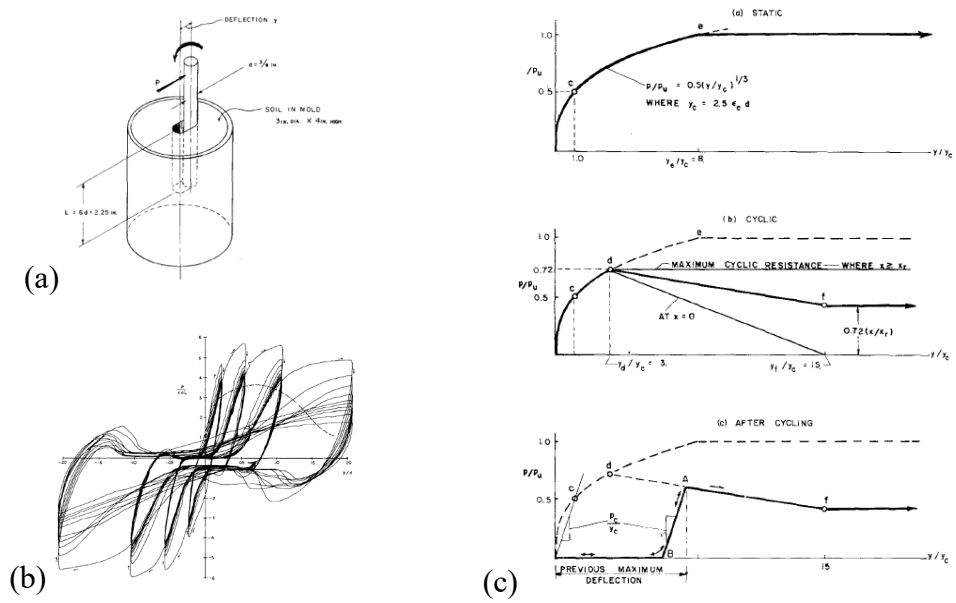
Figure 2.1 (a) miniature pile fabricated by Matlock (1970) (b) clay resistance due to slow cyclic loading (c) proposed p-y curves for piles in clay
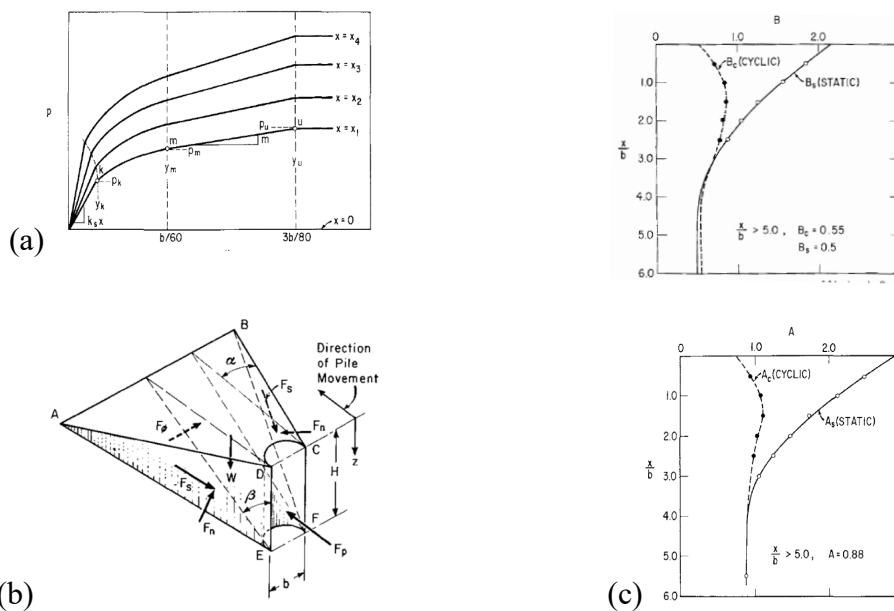


Figure 2.2 (a) p-y curves constructed by Reese et al. (1974) for the case of piles in sand (b) 3D failure wedge (c) factors proposed by Reese et al (1974) for cyclic loading

Reese et al. (1974) investigated pile behavior in cohesionless soil. After a series of experiments conducted on piles embedded in cohesionless soil, Reese et al. proposed a nonlinear stitched model consisting of a linear segment, a parabolic transitional segment, a softer elastic region, and an ultimate segment. The p-y curve model is shown in Figure 2.4a. The linear elastic segment is characterized by a back-calculated slope. It is worth noting that the back-calculated slope compared poorly with the values found in the literature as given by Terzaghi. The end of the elastic region is marked by the beginning of a yielding region. The yield region, parabolic in shape, constitutes a transitional phase were the soil gradually loses stiffness until it reaches a stable value at point 'm'. Between points m and u, the soil maintains an elastic behavior until it reaches its ultimate resistance at point 'm'. At point 'u' the elastic region is discontinued and the model is forced into a perfectly plastic behavior at ultimate resistance. The ultimate soil resistance was calculated using a theoretical 3-D failure wedge as shown in Figure 2.4b. The dimensions of the 3-D wedge were tailored to match the ultimate resistant force recorded from experimental data.

The three phases noted above by Reese et al. represent the backbone curve for monotonic loading. To introduce the effect of cyclic loading on soil resistance, Reese et al. suggested that the soil resistance at points 'm' and 'u' be multiplied by the modified correction factors B-cyclic and A-cyclic instead of B-static and A-static, respectively. The values of $B_c$ and $A_c$, as shown in the Figure 2.4c, are notably smaller than their static counterparts, resulting in a degradation of soil resistance after cyclic loading.

## C. Dynamic Analysis of Piles Utilizing P-Y Curves

Concerns about the effect of kinematic and inertial forces on piles are raised in the literature (Finn et al. 2005, ECN, 2003). Finn et al. (2005) argued that pseudo-static seismic analysis done as a result of monotonic and slow cyclic loadings will give incorrect results. This was demonstrated by Wilson et al. (1998). Wilson et al. conducted a series of centrifuge tests on piles while exciting the system with a seismic event. A mass 'm' was attached to the top of the pile to produce inertial forces. Figure 2.5 compares the centrifuge test results with other experiments that do not account for kinematic and inertial forces. It can be seen from Figure 2.5 that kinematic forces had much lesser effect on piles than inertial forces.
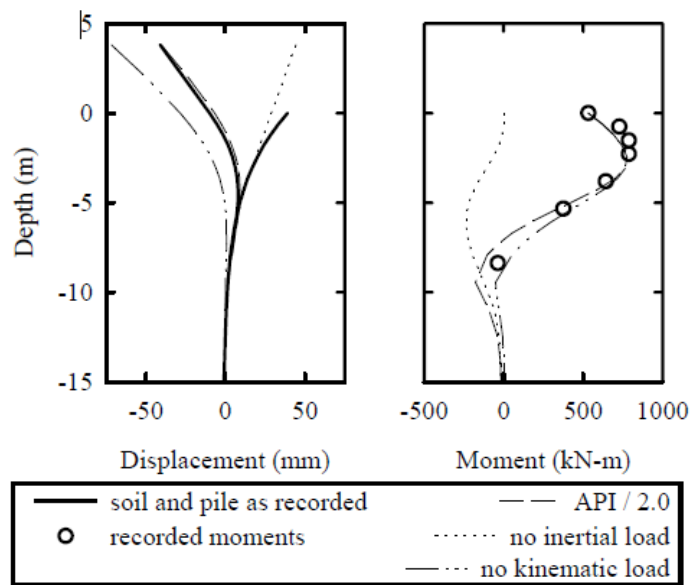
Figure 2.3 Graphs constructed by Wilson et al. showing the effect of inertial and kinematic loads on the behavior piles

Other methods for solving the problem of piles under dynamic loading are proposed in literature. These methods include finite element method (FEM) (Randolph, 1981), boundary element method (BEM) (Sanchez, 1982), and Beam on Non-linear Winkler Foundation (BNWF) (Boulanger et al. 1999, Allotey 2007).

Initially, BNWF models applied the ground motion time history at the end of each spring as displacement inputs (Matlock & Foo, 1978). Dashpots were then added in parallel to the springs to model the damping radiation of the structure (Kagawa, 1980). Recently, the method was enhanced by Wang et al. (1998) by linking the structure to the soil-column by near-field springs and a far-field spring paralleled by a dashpot (Figure 2.6).
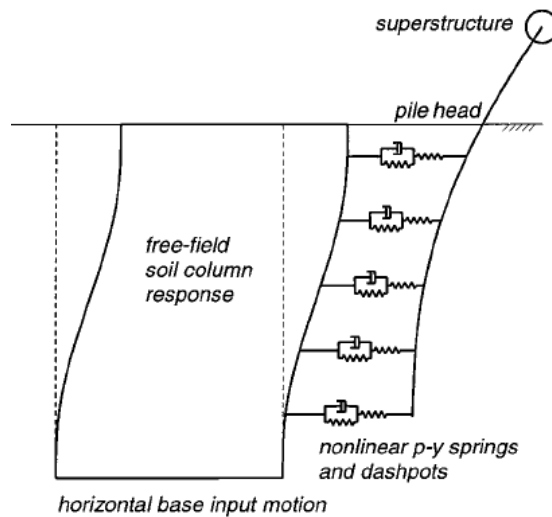


Figure 2.6 Model proposed by Wang et al. (1998) for the dynamic analysis of piles

The clay is conceptualized as three components working in series: elastic component ($p\text{-}y^e$), plastic component ($p\text{-}y^p$), and gap component ($p\text{-}y^g$). Figure 2.8a shows a sketch of the three components of clay behavior working in series. Radiation damping is accounted for using a dash-pot placed in parallel to the elastic p-y component in an arrangement termed as "series hysteretic/viscous damping" as proposed by Wang et al. (1998). On the other hand, the sand was modeled using the p-y back-bone curve recommended by API 1993 as shown in Figure 2.7. Recorded free-field motions at different soil depths were used as input for the dynamic p-y analysis. The results of the p-y dynamic analysis proved satisfactory.

### D. P-Y Curves and Finite Element for the Analysis of Basement Walls

One of the earliest pseudo-static studies aimed at developing a methodology for the design of yielding-retaining walls subjected to seismic events was done by Okabe and Mononobe-Matsuo in 1926 and 1929, respectively. The method resulting from these studies, known as the Mononobe-Okabe (M-O), gained popularity due to its simplistic approach and ease of application. Relying on Coulomb theory, M-O derives their expression by subjecting a failure wedge to pseudo-static acceleration resulting from dynamic loading. Though easy to use, M-O method suffers certain limitations and should be used with care (Kramer, 1996).
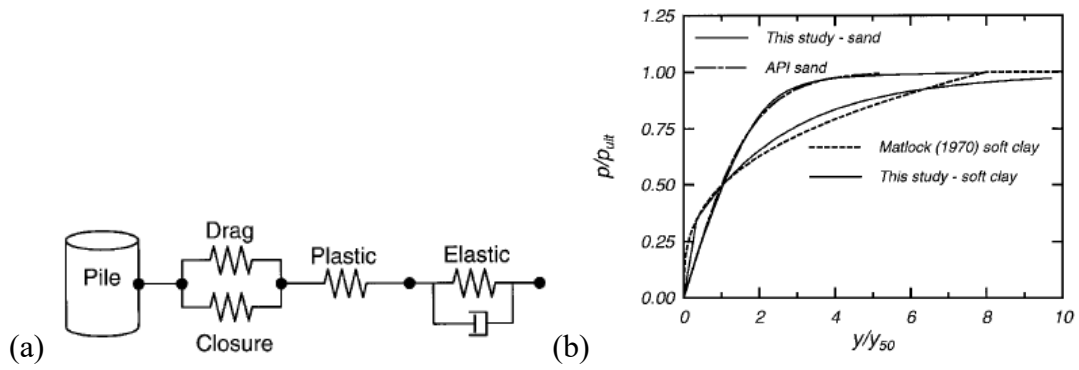
Figure 2.4 (a) Components of Non-linear p-y elements (b) Normalized p-y curves for soft clay and sand

The M-O method assumes that the wall displacement during a seismic event is sufficient for the limit state to be reached in the soil. Wood (1973) argued that a limit state may not be reachable in all practical soil retaining systems i.e. basement walls, rigid retaining walls or small amplitude seismic events. For such cases, the soil will behave elastically and the assumption of a failure wedge formation behind the wall would be inaccurate. To solve this problem, Wood (1973) developed a finite element model to plot the lateral stress distribution on the wall. The soil was modeled as an elastic continuum and pushed horizontally with a static 1g force. Figure 2.8 shows the finite element model proposed by Wood (1973). As shown in the figure, different mesh sizes were compared and a course mesh was chosen as sufficiently accurate.

Nadim and Whiteman (1983) enhanced the 2-D plain-strain finite-element model proposed by Wood (1973) by introducing two preset slip planes: one at the wall interface with the soil and the second inclined within the soil elements propagating from the bottom corner to the surface (Figure 2.9).
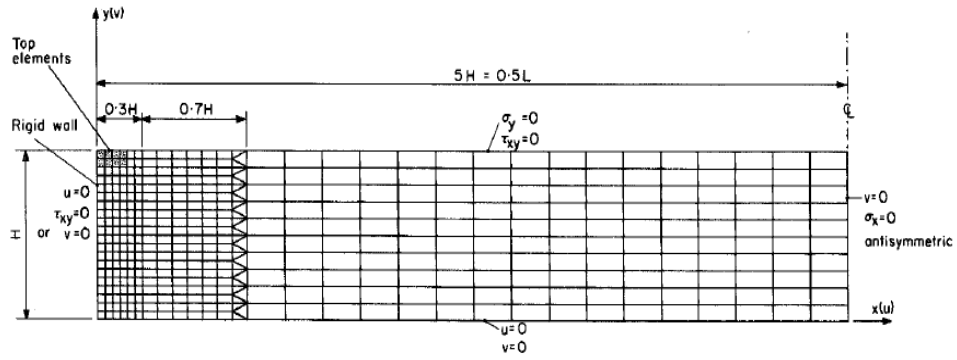
Figure 2.5 Finite element model proposed by Wood (1973)
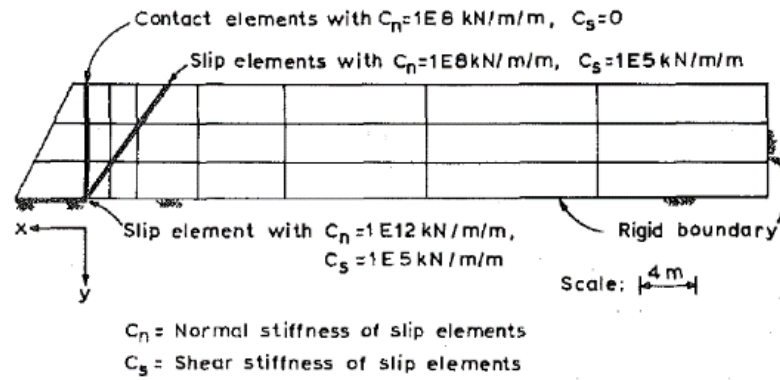


Figure 2.6 Finite element model proposed by Nadim and Whiteman (1983)
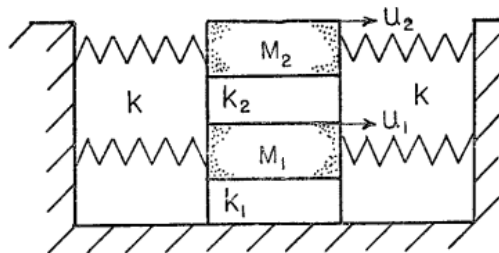


Figure 2.7 Lump mass shear-beam Winkler model by Scott (1973)

An alternative method to finite element was proposed by Scott (1973). Scott modeled the soil as a shear beam connected from one side to a fixed boundary and the other to a rigid wall using elastic springs (Figure 2.10). Forces on the wall were computed and were comparably higher than those predicted by M-O method.

The simplified shear-beam model proposed by Scott (1973) was enhanced by Richard et al. (1999) to include a free-field and a near-field soil behavior as shown in Figure 2.11. The free-field represent the portion of the soil that is not influenced by the structure, whereas the near-field soil represents the soil behavior adjacent to the wall. The near-field soil is modeled by a series of springs having a bilinear p-y curve consisting of an elastic portion bounded by an upper and a lower limits defined by active and passive state. The elastic stiffness varies with the square root of depth 'z' and as given by the equation $k_s = \frac{1.35 G_{fl}}{H} \sqrt{\frac{z}{H}}$ , where $G_{fl}$ is the elastic shear modulus at depth H. Finally, an expression for the stress distribution behind the wall is proposed based on incremental plasticity theory and Mohr-Coulomb failure criterion.

Maleki and Mahjoubi (2010) studied the effect of wall flexibility on the soil resistance subjected to dynamic loading. As shown in Figure 2.12, they proposed a model that utilizes springs for near-field soil and a discretized semi-infinite continuum for free-field soil. The free-field soil consisted of plain strain elements fixed at the bottom and vertically restrained at the left end. The near-field soil was modeled as a series of springs having a p-y curve similar to that proposed by Richard et al. (1999). The wall and the soil continuum were simultaneously excited by 6 earthquake events and the pressure distribution behind the wall was plotted.
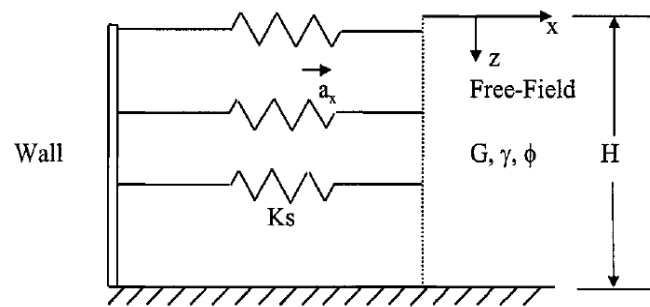
Figure 2.8 Dynamic model proposed by Richard et al. (1999)
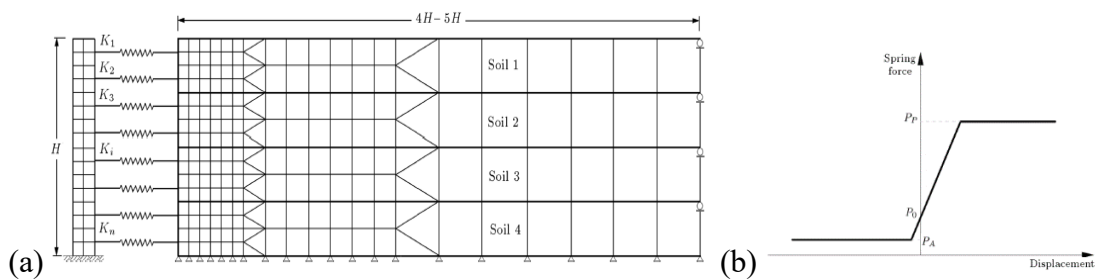


Figure 2.9 (a) FEM model proposed by Maleki et al. (2010) (b) p-y curve model for springs at near-field

Beam-column models attached to series of springs were also investigated for the case of tie-back walls under static loading resulting from sequential construction (Briaud, 1998). Three major components were identified in tieback walls, namely the wall retaining the natural soil, soldier piles below excavation level, and the anchors (Figure 2.13). Since each component responds differently when loaded, three different p-y curves were considered. The p-y curve for the retained sand was taken as a bilinear elastic perfectly-plastic model with a special twist. Based on back-calculated data extracted from a full scale test conducted by Kim (1994), the elastic limits for active and passive displacements were considered invariable at 1.3mm and 3mm, respectively.

Variation in the elastic stiffness is thus ensured with changes in values of $P_{active}$ and

$P_{passive}$ at different depths. This is slightly different from the approach adopted by

Richard el al. (1999) and Maleki & Mahjoubi (2010).
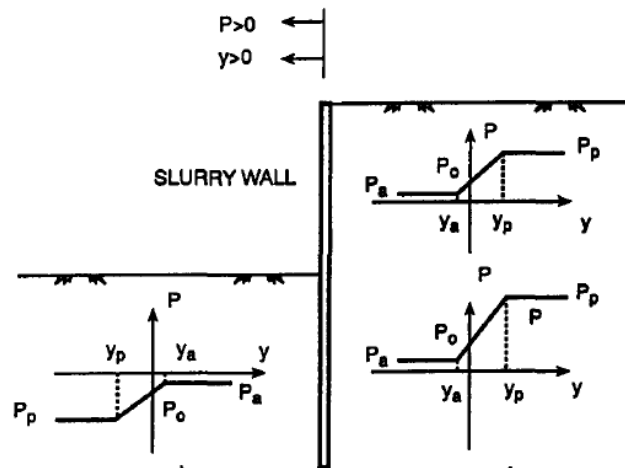


Figure 2.10 Different p-y curves used for tieback walls for different components as proposed by Briuad and Kim (1998)

# CHAPTER 3

# ACTIVE P-Y RESPONSE FOR RIGID WALLS

# RETAINING GRANULAR SOILS

### A. Introduction

The mobilization of active lateral pressure on retaining walls has been studied extensively. Traditional lateral earth pressure methods replace the soil by an earth pressure distribution evaluated as the product of the vertical effective stress and the active earth pressure coefficient $k_a$. The earliest solutions for $k_a$ are reflected in the theories proposed by Rankine and Coulomb (Das 2015). More recently, upper bound and lower bound solutions (Chen 1975, Soubra and Macuh 2002, Lancellotta 2002, and Paik and Salgado 2003) that are based on limit analysis and soil arching principles have also been developed. Loukidis and Salgado (2012) report that the differences between the upper bound values for $k_a$ as obtained using Coulomb's solution, Chen (1975), Soubra and Macuh (2002) and the lower-bound solution presented in Lancellotta (2002) are minimal and do not exceed 7%. However, they state that solutions that are produced by limit state analyses may be valid for cases where the wall displacements are large enough to mobilize fully active conditions. In the context of performance-based design where the stresses that are associated with a given level of wall displacement govern the design, there is a need to assess the evolution of the earth pressure parameter $k$ as a function of the wall displacement. Loukidis and Salgado (2012) conducted rigorous finite element analyses to quantify the relationship between $k$ and wall displacement. There analysis was however restricted to the case of gravity walls.

For structures with underground basement walls, the soil-structure-interaction between the side soil and the walls affects the response of the system, particularly under cyclic loading conditions. In the context of performance-based design, there has been interest in quantifying the relationship between the lateral earth pressure and the wall displacement using the concept of p-y curves by replacing the homogeneous soil continuum by a series of springs that mimic the soil behavior adjacent to the substructure. The p-y method has been advocated and applied by geotechnical and structural engineers in the design of laterally loaded piles (Matlock 1970 and Reese et al. 1974). The problem for piles has been extensively studied using full scale field tests, centrifuge tests, and 3D finite element analyses.

On the other hand, very limited studies have been conducted on the mobilization of lateral earth pressure behind rigid walls in the context of p-y curves. Briaud and Kim (1998) were the first to recommend p-y relationships for the analysis and design of tieback walls. These p-y relationships were calibrated/back calculated using data collected from full scale tests on walls in sand. Briaud and Kim (1998) state that the lateral earth pressure that is exerted by the soil on the wall is bounded by the active and passive earth pressure conditions. Based on the data collected, they recommend that the active earth pressure could be assumed to be mobilized at wall movements of 1.3mm (away from the retained soil). El Ganainy and El Naggar (2009) and Saad et al. (2016) adopted this p-y relationship as the backbone curve for the lateral pressure-lateral deflection relationship used for modeling the side soil in their analysis of the response of buildings with underground stories.

In reality, the relationship between lateral earth pressure and wall displacement is expected to be complex and is affected by the height of the wall, the relative density of the backfill material, the interface friction between the wall and the soils, the non-linearity of the soil response, and the type of wall movement (translation and/or rotation). Elchiti et al. (2017) conducted a preliminary investigation of the p-y response of rigid basement walls in the active state of loading and concluded that the above mentioned complexities in the relationship between lateral earth pressure and wall displacement could be captured using numerical analyses. The analyses conducted in Elchiti et al. (2017) were however restricted to rigid basement walls that are simplistically assumed to be fixed at their base (supported on rock).

There is a need for realistic and simplified models that could describe the p-y relationship for rigid retaining walls to be used as input in robust soil-structure-interaction problems in the context of performance-based design. Such p-y relationships could be incorporated in commercial structural analysis software in the form of non-linear springs that describe the lateral pressure versus lateral displacement relationship. This is consistent with the p-y curves concept commonly used to model the reaction of the soil for laterally loaded piles.

The goal of this paper is to shed light on the mechanics of the soil-structure interaction between rigid basement walls and granular backfill soil in the active state of loading. This is achieved by (1) building a PLAXIS 2D model that incorporates the wall, backfill and foundation soil, (2) investigating the effect of the height of wall, soil properties, and interface friction angle on the lateral p-y response, and (3) utilizing the

26

results to establish a simple empirical model that is capable of predicting the p-y response behind rigid basement walls in the active state of loading.

### B. Finite Element Study

The finite element model of the rigid retaining wall and the backfill material was built in PLAXIS 2D and presented in Figure 3.1. The model consists of a rigid retaining wall subjected to a varying horizontal prescribed displacement, a semi-infinite half space backfill soil medium, a semi-infinite half space subsoil medium, and two interface soil layers acting on the boundaries of the backfill with the rigid wall and the subsoil layer. The rigid wall is modeled as a rigid rectangular plate and moved incrementally in the active direction using a non-uniform horizontal prescribed displacement. The prescribed displacement is applied on the wall with a linearly varying intensity such that the bottom magnitude equals to 20% that of the top. The prescribed displacement restrains the wall vertically, allows no bending in the wall to occur, and ensures a rigid rotation of the wall with a bottom movement of 20% that of the top.

The applied wall displacement field was selected based on the results presented in Saad et al. (2016) for basement wall displacements under real earthquake excitation. The results showed that walls in buildings that included multiple basements showed more-or-less rigid wall rotations with maximum lateral wall displacements recorded at the top of the wall (ground level) and minimum lateral wall displacements recorded at the level of the foundations. The magnitude of the wall displacement at the foundation level was evaluated to be between 10% and 20 % of the top wall displacement.  In their numerical study, Elchiti et al. (2017) investigated the effect of bottom wall
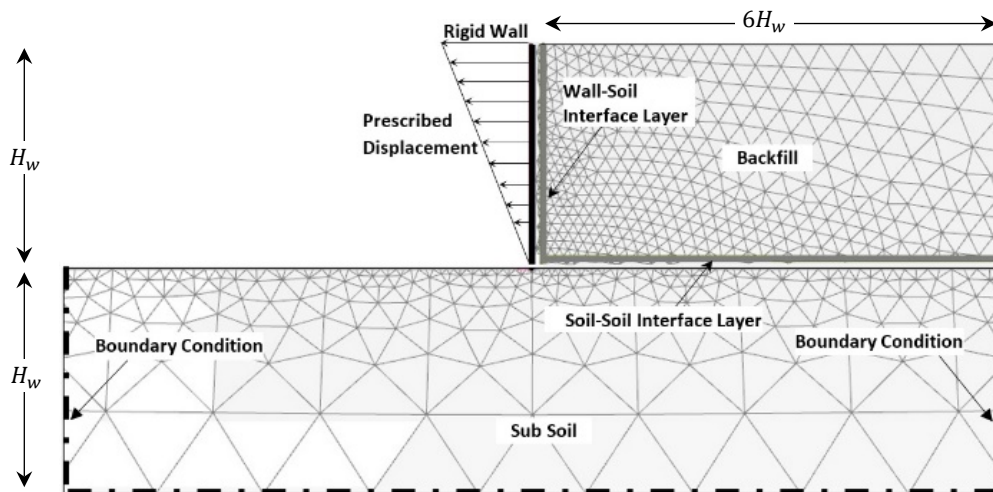
Figure 3.1 Finite element model in PLAXIS 2D (not to scale)

displacement $(y_b)$ on the resulting p-y relationship by adopting a displacement at the

base of the wall that is equal to a certain percentage of the top wall displacement $(y_t)$.

The analysis included pure wall rotation about the wall base $(y_b = 0\%)$, in addition to a

combination of translation and rotation conditions$(y_b = 0.1 \, y_t \, and \, 0.2 \, y_t)$. They

observed that the resulting p-y relationships at different depths are slightly sensitive to

the assumed base wall movement condition. As a result, the displacement at the base of

the wall in this study was taken as 20% of the top wall displacement.

The subsoil and backfill continua are meshed using 15-noded plane-strain

triangular elements of varied sizes ranging from very fine elements at locations of stress

concentration to course elements at the boundaries. The length of the backfill soil

together with the height and length of the subsoil continuum are critically chosen to

ensure a semi-infinite behavior of the soil continuum with no limitation imposed by the

boundary conditions on the rigid wall behavior. An interface layer is modeled at the

soil-wall boundary. The interface layer allows for reduced soil strength and stiffness at

the interface and a differential displacement (slip) between the wall and the backfill. The left and right boundary conditions restrict movement in the horizontal direction while allowing free vertical movement of the soil. The bottom edge of the subsoil continuum is modeled as fixed.

### C. Constitutive Soil Model

Elchiti et al. (2017) compared the response of granular backfill in active wall displacement for soil modeled using the traditional Mohr-Coulomb model and the more advanced Hardening Soil model that is built-in in PLAXIS. They concluded that the results of the Mohr-Coulomb model exhibit signs of numerical instability at relatively small wall displacements. These numerical instabilities were attributed to the elastic-perfectly plastic nature of the Mohr-Coulomb model, whereby soil elements in the active failure wedge will yield early on in the deformation process causing loss of stability at larger deformations. On the other hand, the Hardening Soil model yielded a more stable response that was capable of predicting the p-y behavior of the retained granular soil up to large wall displacements. Accordingly, the Hardening Soil model was adopted in this study to model the constitutive response of the backfill and subsoil in the FE analysis.

The Hardening Soil model in PLAXIS is an advanced non-linear model that assumes a hyperbolic relationship between stress and strain. The Hardening model adopts isotropic hardening and includes two yield surfaces to differentiate between shear and isotropic loading (Schanz 1999). The final bounding surface is based on the Mohr-Coulomb failure envelope with a non-associated flow rule using the dilatancy angle as the non-normality parameter. With respect to its stiffness behavior, the model considers stress

and strain level dependency of the moduli. A hyperbolic stress - strain relation is considered between the deviatoric stress and the major principal strain to account for strain dependency, while a power law is adopted to consider stress dependency, and the user specifies the moduli at a certain reference pressure. In this study, the parameters utilized in the Hardening soil model (Table 3.1) were adopted from Skeini (2015) and are consistent with the behavior of loose, medium dense and dense Ottawa sand. It should be noted that all interface soil layers in PLAXIS 2D are modeled using the Mohr-Coulomb model. When more advanced soil models are chosen, PLAXIS 2D extracts the parameters relevant to the Mohr-Coulomb model and applies the reduction factor to them to deduce the shear strength parameters of the interface response between the soil and the wall.

**Table 3.1** Soil properties for the hardening model in PLAXIS 2D

| | Parametric Study Cases with different Densities | | | Validation Example |
|---|---|---|---|---|
| | Loose | M. Dense | Dense | M. Dense |
| Soil Unit Weight, $\gamma$ $(kN/m^3)$ | 16.5 | 18.0 | 19.5 | 17.0 |
| Initial Void Ratio, $e_{int}$ | 0.685 | 0.615 | 0.560 | 0.615 |
| Sec. Stiffness, $E_{50}^{ref}$ $(MPa)$ | 15-25 | 30-50 | 60-80 | 45 |
| Tang. Stiffness, $E_{oed}^{ref}$ $(MPa)$ | 15-25 | 30-50 | 60-80 | 45 |
| Unload/ reload Stiffness, $E_{ur}^{ref}$ $(MPa)$ | 200000 | 200000 | 200000 | 200 |
| Power of stress dependency of E, m | 0.4 | 0.4 | 0.4 | 0.4 |
| Cohesion, $C_{ref}'$ $kN/m$ | 1.0 | 1.0 | 1.0 | 1.0 |
| Friction Angle, $\emptyset'$ (°) | 33 | 36 | 39 | 34 |
| Dilation Angle, $\psi$ (°) | 4 | 7 | 11 | 7 |
| Poisson' Ratio, $v'$ | 0.3 | 0.3 | 0.3 | 0.3 |
| Reference Stress, $p_{ref}$ $(kPa)$ | 100 | 100 | 100 | 100 |
| Failure Ration, $R_f$ | 0.95 | 0.95 | 0.95 | 0.95 |

## D. Parametric Study

A parametric analysis was implemented to characterize the components that affect the variation of lateral earth pressure with respect to active wall displacement. The parameters that were varied are the: (1) height of wall, (2) relative density of soil, and (3) soil-wall interface friction angle. P-y curves for loose, medium dense, and dense sands retained by 5m, 10m, and 15m high walls were determined and analyzed. For each case analyzed, two types of interface roughnesses were considered: a rough surface that is typical of a concrete basement wall and an idealized non-frictional surface that is assumed to be perfectly smooth. Although the latter case may not be applicable in practice, its importance lies in understanding the effect of the interface properties on the p-y response. The importance of characterizing the p-y response of a non-frictional wall will be discussed in the remainder of this paper. To model both types of surfaces, reduction factors, $R$, of 0.8 and 0.1 are used to simulate the rough and smooth wall, respectively. The reduction factor in PLAXIS resembles the ratio of the interface soil property (friction coefficient and stiffness) to the backfill soil property. An interface reduction factor of 0.1 (rather than zero) was used to model the non-frictional wall. This is attributed to numerical instabilities that were observed in the case of $R = 0.0$. A graphical representation of the above parametric study is shown in Figure 3.2. It is clear from Figure 3.2 that the study includes an analysis of the effect of the modulus of elasticity of the soil on the p-y response for every given relative density.

Height of Wall:
5m, 10m, 15m

Interface Reduction Factor (R):
0.1, 0.8

Loose
($\phi = 33^o$)

Medium-Dense
($\phi = 36^o$)

Dense
($\phi = 39^o$)

$E_{50}^{ref}$=15 MPa   E=2   E=2   E=30   E=40   E=50   E=60   E=70   E=80
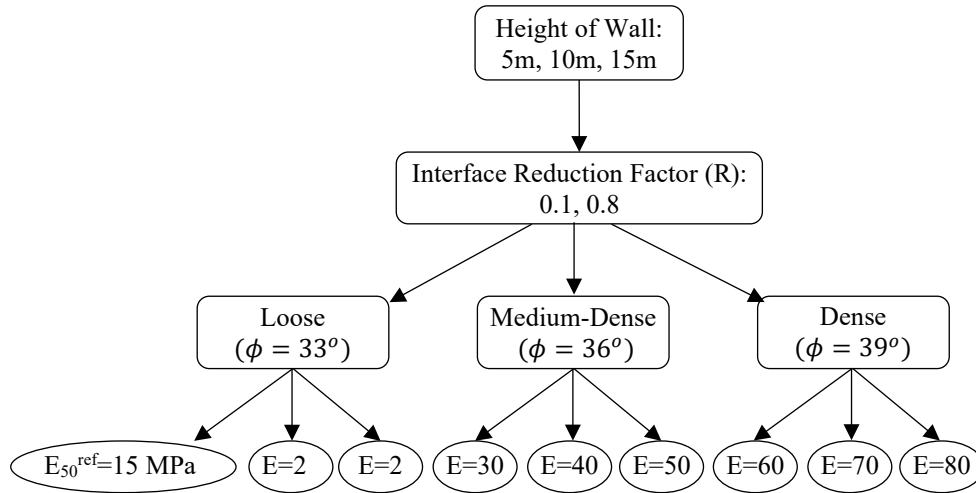
Figure 3.2 Wall and soil parameters used in the numerical parametric study

## E. Results

### 1. *P-Y Curves for the Case of a Frictional Wall*

To plot the p-y curves, stress points at 1m depth intervals along the height of the wall are chosen. At any given increment of top wall displacement, the lateral earth pressure is plotted against the horizontal displacement of the wall at each stress point. P-y curves for a 10m high wall with an interface reduction factor of 0.8 are plotted for the case of loose and medium dense soil in Figure 3.3. The p-y curves are presented for depths ranging from 1.0m to 8.0m. Also shown on the figures is the theoretical "active" earth pressure computed at the limit state using Coulomb's method. The curves on Figure 3.3 represent p-y curves in the sense that they portray the relationship between the lateral earth pressure at a depth 'z' versus the wall displacement at that particular depth 'z'. At zero wall displacement, the lateral earth pressures correspond to the at-rest condition. As the wall is displaced laterally, the lateral earth pressures are reduced with displacement and the rate of reduction in lateral stress with displacement is observed to decrease systematically until fully active conditions are mobilized.

More importantly, the p-y relationships presented in Figure 3.3 for frictional rigid walls indicate that the adoption of a depth-independent fixed lateral displacement of 1.3mm as a criterion for full mobilization of active earth pressure in published p-y curves (Briaud and Kim 1998, El Ganainy and El Naggar 2009, and Saad et al. 2016) may not be completely representative of the true response. The 1.3mm displacement criterion is presented graphically on Figure 3.3. While this criterion may be more-or-less applicable in predicting the displacement required to approach active conditions at
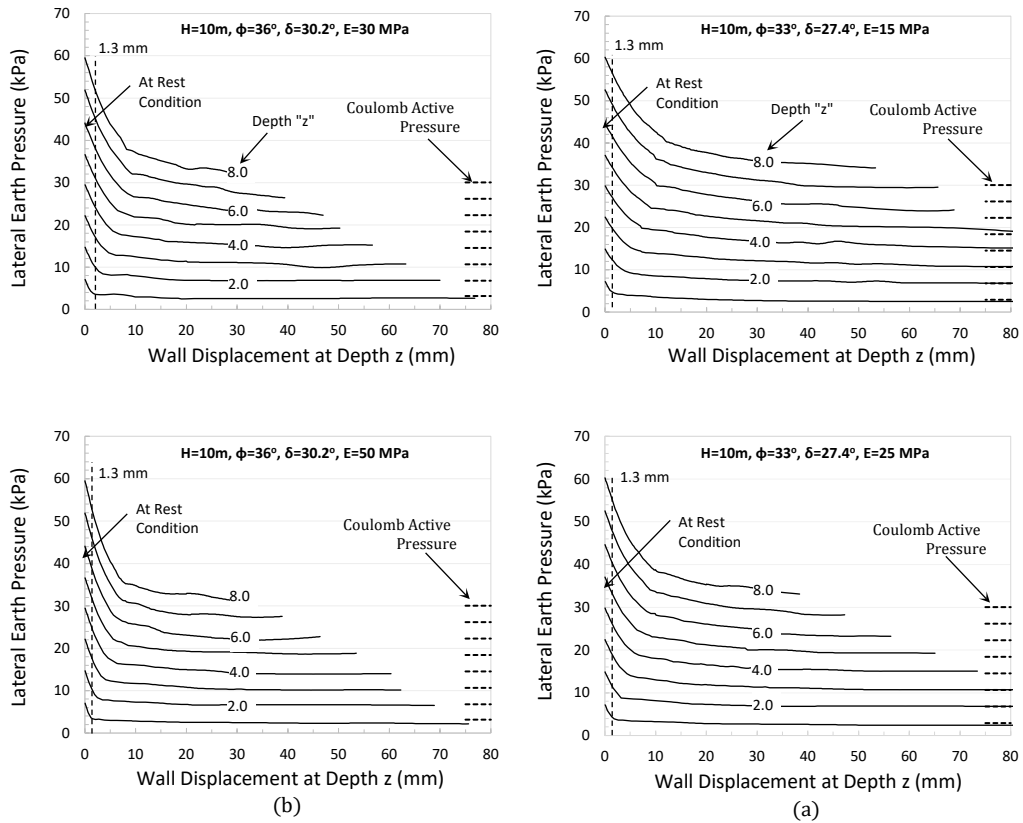


Figure 3.3. P-y Curves for frictional wall, R=0.8, retaining (a) loose granular soil and (b) medium dense granular soil

very shallow depths (z = 1m), the p-y curves at larger depths indicate that displacements as high as 10mm are required for depths as high as 8m for cases of loose sand.

The effect of soil density on the p-y relationship for identical wall cases is clearly illustrated when comparing the results between Figures 3.3a (loose sand) and 3b (medium dense sand). The p-y curves for medium dense sands are observed to be initially steeper (faster reduction in lateral stress with displacement) than those of loose sands. In addition, the displacement required to approach active stresses in medium dense sands are smaller (1.5 to 8mm) than loose sands (2 to 15mm). It is interesting to note that at any given density, the p-y curves are shown to be also sensitive to the assumed modulus of elasticity as reflected in Figures 3.3a ($E_{50}{}^{ref}$ of 15 and 25 MPa) and Figures 3.3b ($E_{50}{}^{ref}$ of 30 and 50 MPa). As the modulus of elasticity increases, the steepness of the initial portion of the p-y curve increases and the displacement required to approach active conditions decreases.

### 2. *P-Y Curves for the Case of a Non-Frictional Wall*

The finite element analyses were repeated for the case of "non-frictional walls". The resulting p-y relationships at depths ranging from 1.0m to 8.0m in a 10m high wall are presented in Figures 3.4a (loose) and 3.4b (medium dense), respectively. Also plotted are the theoretical "active" earth pressures that correspond to the Coulomb method for computing Ka for non-frictional walls.

The p-y curves on Figures 3.4 exhibit a response that is clearly different than that observed for the cases involving soil/wall friction. The p-y curves in the non-frictional cases are smoother, with an initial response that is less steep and a reduction in stiffness that is more gradual starting from the at-rest condition all the way to the

34

fully active condition. The displacements required to approach fully active conditions are clearly larger than the displacements observed in the case of frictional wall.

### F. Analysis of Numerical Results

A comparison between the p-y curves of identical frictional and non-frictional walls underlines the significance of the properties of the interface friction on the p-y response. Any attempt to model p-y curves numerically or analytically will require an investigation of the development of shear stresses at the soil-wall interface. It is evident, that rigid wall displacements are accompanied by the slippage of soil on the soil-wall
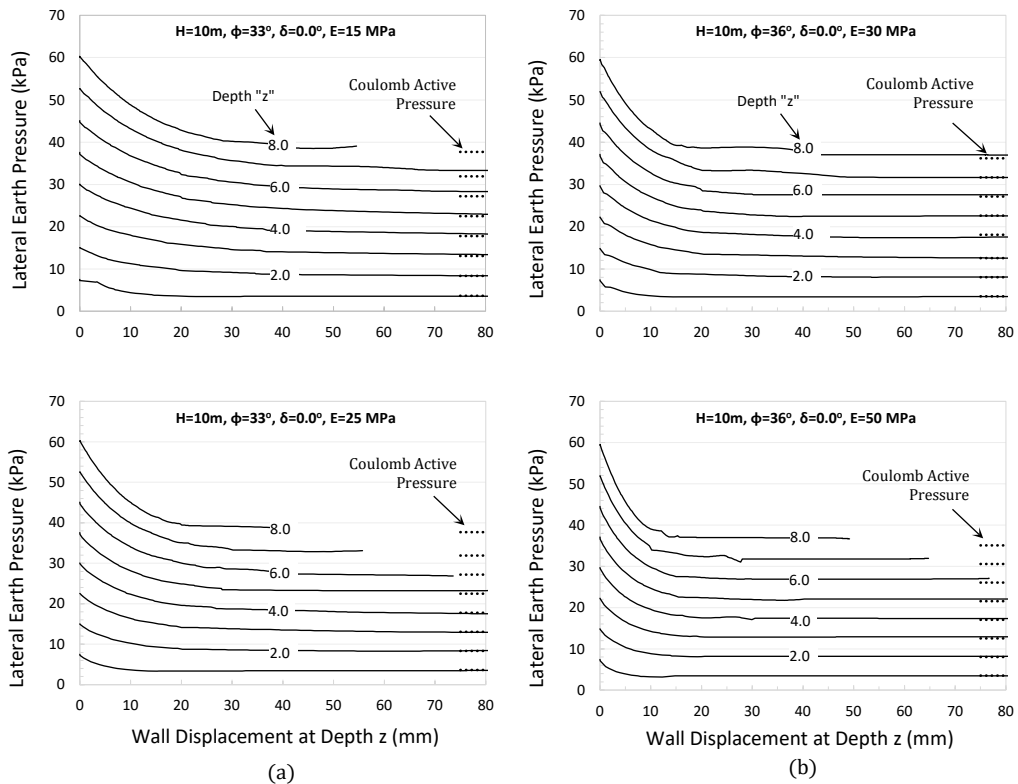


Figure 3.4 P-y Curves for non-frictional wall ($\delta = 0^o$) retaining (a) loose granular soil and (b) medium dense granular soil

interface. In the case of frictional walls undergoing active displacement, soil slippage leads to the development of upward vertical stresses. At any given depth, it is expected that such shear stresses will reduce the vertical stress at the soil-wall interface in comparison to the free field stresses ($\gamma.z$).

Figure 3.5 shows the vertical stress contours for medium dense soil retained by a 10m frictional wall displaced in the active direction. The reduction in vertical stress noted above can be seen in the soil at proximity to the wall. Such reduction in the vertical stresses at the soil-wall interface will result in variations in the horizontal lateral stresses which would be reflected in the observed p-y response. In this study, it is hypothesized that the p-y response of a frictional wall could be derived from the p-y response of an identical "non-frictional" wall provided that the reduction in the vertical stresses due to wall friction at the soil-wall interface is taken into consideration and properly modeled. If the drop in vertical stress $\Delta\sigma_{v,i}^{f}$ at a given wall displacement increment (i) can be quantified, the horizontal lateral stress of the frictional wall $\sigma_{h,i}^{f}$ can be simply deduced from the lateral stress of an identical non-frictional wall $\sigma_{h,i}^{nf}$ such that:

$$\sigma_{h,i}^{f} = \sigma_{h,i}^{nf} - k_i.\Delta\sigma_{v,i}^{f} \tag{1}$$

where the superscript $f$ denotes the case of frictional wall, the subscript $nf$ denotes the case of non-frictional wall, and $i$ denotes an increment of wall displacement.

The parameter $k_i.\Delta\sigma_{v,i}^{f}$ in Equation (1) reflects the reduction in the lateral earth pressure in the frictional wall cases as a result of the drop in vertical stresses at the
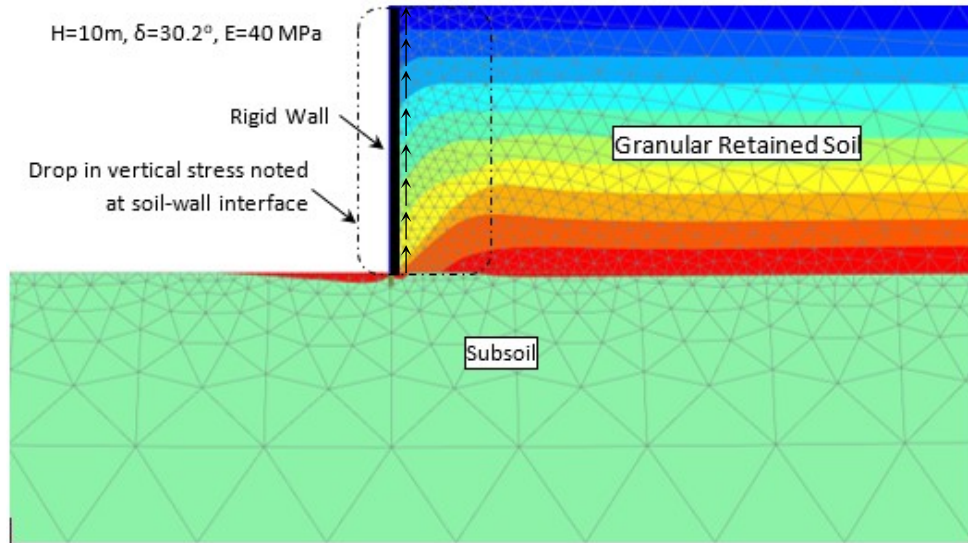
Figure 3.5 Drop in vertical stress at soil-wall interface due to frictional wall displacement.

interface between the wall and the soil due to the mobilization of frictional shear stresses at the interface. In the next section, an effort will be made to present a theoretical basis for the hypothesis presented in Equation (1) and to mathematically determine the relationship between the drop in the vertical stress at the soil-wall interface as a function of the mobilized soil-wall frictional stresses. Given this relationship, Equation (1) can be used to predict the p-y curve of a frictional wall as a function of that of an identical non-frictional wall.

To test the hypothesis reflected in Equation (1), the p-y relationships for identical frictional and non-frictional walls are plotted on Figure 3.6a and 3.6b for loose and medium dense sands, respectively. Also plotted on the figure are the variations observed in the vertical stresses and the frictional shear stresses at the interface between the soil and the wall at the same depths. For illustration, results are only presented for cases involving depths of 3.0m and 6.0m. A comparison between the p-y curves for the

frictional and non-frictional wall cases confirms the observations made in previous sections regarding the clear differences in the p-y responses. An investigation of the variations in the vertical and frictional stresses with displacement show that the frictional stresses increase with displacement resulting in a corresponding decrease in the vertical stresses. At a particular wall displacement that is unique to any given density and depth, the frictional stresses reach their maximum values and the vertical stresses reach their minimum values, simultaneously. Not surprisingly, this unique displacement corresponds clearly with the discontinuity that is observed in the slope of the p-y curve in the frictional wall cases. This indicates that the difference between the p-y relationships in the frictional and non-frictional wall cases is directly related to the variation of the frictional stresses with displacement.

The difference between the p-y curve for frictional and non-frictional walls at any given depth z is related to the drop in the vertical stresses caused by the formation of vertical shear stress at the soil-wall interface. This section is dedicated to finding the analytical relationship that relates these components. A free body diagram of the failure wedge behind a rigid non-frictional wall at active conditions for granular soil is presented in Figure 3.7a. In the figure, $\theta_{cr}$ denotes the failure angle at limit state measured from the horizontal plane, $P_a$ denotes the active force applied on the wall at active state, $F$ denotes the friction force developing at the soil-soil failure plane, and $\phi$ denotes the soil friction angle. Since the failure wedge at the limit state is in static equilibrium, the forces acting on the wedge constitute a closed force triangle as shown in Figure 3.7a (Coulomb theory). As stated earlier, the $'nf'$ superscript is used after symbols that are designated for the analysis of non-frictional walls.

From the law of sines:

$$P_a^{nf} = W^{nf} \frac{\sin (\theta_{cr}^{nf} - \emptyset)}{\sin(90 - (\theta_{cr}^{nf} - \emptyset))} \tag{2}$$

For the cases involving frictional walls ($\delta > 0$), the corresponding failure wedge and force diagram are presented in Figures 3.7b. In this case, Equation (2) becomes:

$$P_a^{f} = W^{f} \frac{\sin (\theta_{cr}^{f} - \emptyset)}{\sin(90 - (\theta_{cr}^{f} - \emptyset) + \delta)} \tag{3}$$
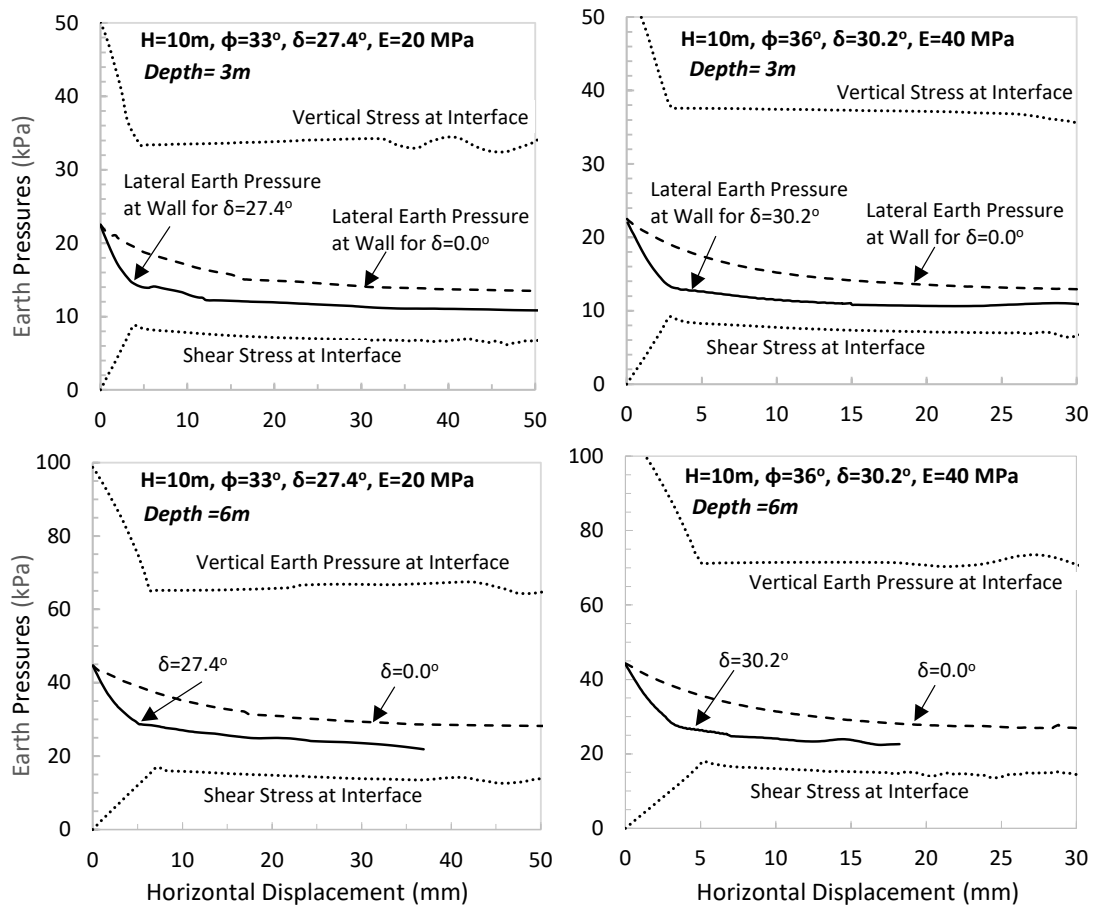


Figure 3.6. Interdependency between P-Y curves for frictional and non-frictional wall (a) loose sand and (b) dense sand
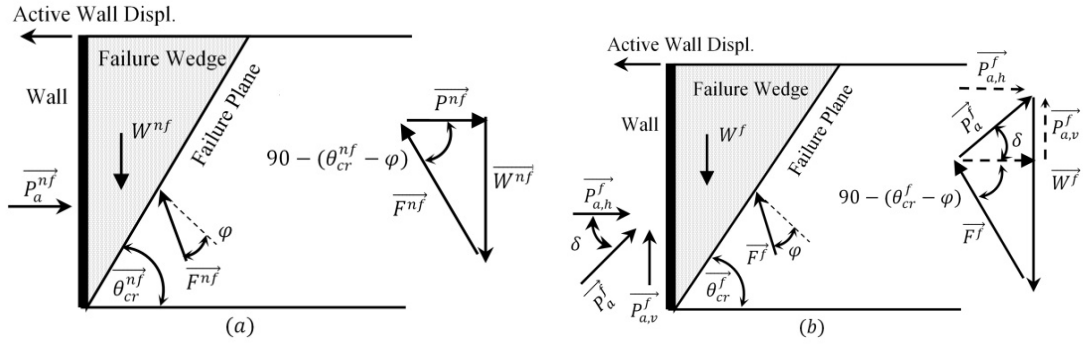
Figure 3.7 Active failure wedge for (a) non-frictional wall and b) frictional wall.

where the superscript $'f'$ denotes a frictional wall. Using the geometry of the wedge and some trigonometric relationships, the ratio $\dfrac{P_a^f}{P_a^{nf}}$ can be written as:

$$\frac{P_a^f}{P_a^{nf}} = g \cdot \left[ \frac{1}{\cos(\delta) \cdot \left( 1 + \dfrac{\tan(\delta)}{\tan\left(90 - \theta_{cr}^f - \emptyset\right)} \right)} \right] \tag{4}$$

where g is given by:

$$g = \frac{\tan\left(\theta_{cr}^{nf}\right)}{\tan\left(\theta_{cr}^f\right)} \cdot \frac{\sin\left(\theta_{cr}^f\right)}{\sin\left(\theta_{cr}^{nf}\right)} \cdot \frac{\sin\left(90 - \left(\theta_{cr}^{nf} - \emptyset\right)\right)}{\sin\left(90 - \left(\theta_{cr}^f - \emptyset\right)\right)} \tag{5}$$

For friction angles ranging from 30 to 40 degrees, which is the expected range of fiction angles for sand, the variable 'g' in Equation (5) can be approximated as 1.0. Therefore, Equation (4) can now be approximated as:

$$\frac{P_a^f}{P_a^{nf}} = \left[ \frac{1}{\cos(\delta) \cdot \left( 1 + \dfrac{\tan(\delta)}{\tan\left(90 - \theta_{cr}^f - \emptyset\right)} \right)} \right] \tag{6}$$

The physical meaning of the mathematical terms presented in Equation (6) is reflected in the force triangles presented in Figure 3.7. $\tan(\delta)$ and $\tan(90 - (\theta_{cr}^f -$

$\emptyset$)) refer to $\dfrac{Pa_v^f}{Pa_h^f}$ and $\dfrac{W - Pa_v^f}{Pa_h^f}$ respectively, where the subscripts "$v$" and "$h$" denote the

vertical and horizontal components of the forces. Replacing both parameters in Equation

(6), the above equation can be rewritten as:

$$Pa^f \times \cos(\delta) = Pa_h^f = Pa^{nf} - Pa^{nf} \times \frac{Pa_v^f}{W^f} \tag{7}$$

The force terms at limit state in Equation (7) can be expressed for a wedge with

a height "$h$" as:

$$Pa_h^f = K_a^f \left(\frac{\gamma.h^2}{2}\right) \tag{8}$$

$$Pa^{nf} = K_a^{nf} \left(\frac{\gamma.h^2}{2}\right) \tag{9}$$

$$Pa_v^f = \tau_a^f \left(\frac{h}{2}\right) \tag{10}$$

$$W^f = \frac{\gamma h^2}{2} \times \frac{1}{\tan(\theta_{cr}^f)} \tag{11}$$

Substituting Equations (8), (9), (10) and (11) in Equation (7), one gets the

following relationship:

$$k_a^f (\gamma h) = k_a^{nf}.(\gamma h) - k_a^{nf}.(\tau_a^f \tan\theta_{cr}^f) \tag{12}$$

or

$$k_a^f (\gamma h) = k_a^{nf} (\gamma h - \tau_a^f \tan\theta_{cr}^f) \tag{13}$$

or

$$\sigma_{a,h}^f = \sigma_{a,h}^{nf} - k_a^{nf} \tau_a^f \tan\theta_{cr}^f \tag{14}$$

where: $k_a^f$= active coefficient of earth pressure for frictional wall i.e $\delta \neq 0$.

$k_a^{nf}$= active coefficient of earth pressure for non-frictional wall i.e. $\delta = 0$.

$\tau_a^f$= interface shear at active condition at depth $h$.

$\theta_{cr}^f$ = failure plane angle made with the horizontal axis for a frictional wall.

It can be inferred from Equation (14) that the active lateral earth pressure behind a frictional wall $\sigma_{a,h}^f$ can be computed from the lateral earth pressure behind an identical non-frictional wall ($\sigma_{a,h}^{nf}$) less a component of stress ($k_a^{nf}\tau_a^f tan\theta_{cr}^f$) that is related to the reduction in the vertical stress at the soil wall interface due to friction.

The relationship in Equation (14) was derived for the active limit state condition for the wall. To show the validity of the relationship, the lateral earth pressure computed using Equation (14) was compared with the Coulomb lateral earth pressure at the active limit state for a 10m wall retaining granular soil having a friction angle $\emptyset = 36°$, a soil density of $\gamma = 18.0\ kN/m^3$, and an interface friction angle $\delta = 30.2°$ (equivalent to a reduction factor $R$=0.8). The lateral earth pressure computed at a depth of 4m using Coulomb theory yields a pressure of $14.73\ kPa$ while that computed using Equation (14) for the same depth yields a pressure of $15.02\ kPa$. Note that the angle of the failure wedge was determined from the finite element results to be equal to 58.5 degrees.

Though Equation (14) was originally derived assuming fully active limit state conditions, the equation will be used to predict the lateral earth pressure behind a frictional wall over the whole range of active wall displacements and at any depth $'z'$. To include incremental stepping in the wall displacement, $i$, Equation (14) is expressed in follow form:

$$\sigma_{hi}^f = \sigma_{hi}^{nf} - k^{nf}\tau_i^f tan\ \theta_{cr}^f \tag{15}$$

The variations of $\sigma^{nf}$ and $\tau_i^f$ with displacement are needed as input in Equation (15) to determine $\sigma_{hi}^f$. These variations will be initially obtained from the FE analysis to validate Equation (15). In the next section, empirical models will be proposed for predicting the variations of $\sigma^{nf}$ and $\tau_i^f$ with displacement to eliminate the need for finite element results while applying Equation (15). The empirical models will be calibrated using finite element results for a practical range of wall heights and sand densities.

The calculation of $\sigma_{hi}^f$ in Equation (15) requires knowledge about the lateral earth pressure coefficient $k^{nf}$ which ranges between the at rest earth pressure coefficient $k_o$ and the fully active coefficient $k_a$. As a first estimate, $k^{nf}$ is assumed to be equal to the lateral earth pressure coefficient for the non-frictional wall at the current wall displacement increment, i. Once the first estimate of $\sigma_{hi}^f$ is obtained from Equation (15), the value of $k^{nf}$ in the second iteration is updated so that it corresponds to the appropriate lateral stress level $\sigma_{hi}^f$. The updated estimate of $k^{nf}$ is then used to determine a better estimate of $\sigma_{hi}^f$. Following a small number of iterations, the problem converges and the final estimate of $\sigma_{hi}^f$ is determined and used to plot the variation of $\sigma_{hi}^f$ with wall displacement.

The routine described above was coded in MATLAB language (MIRtoolbox R2018) and tested for the cases of loose and medium dense soils retained by a frictional 10-m wall having an interface reduction factor of $R = 0.8$. The variation of the interface shear stress $\tau_i$ with wall displacement at different depths was extracted from the output files of the PLAXIS 2D results as presented in Figure 3.8. The variation of the lateral

earth pressure $\sigma_{h,i}^{nf}$ with displacement for the case of an identical non-frictional wall was also extracted from the FE model results which were previously presented in Figure 3.4.

Equation (15) was then used to predict the variation of $\sigma_{hi}^{f}$ with wall displacement. The resulting predicted p-y curves for the frictional wall were then plotted using dotted lines and compared to the FE-determined p-y curves (solid lines) in Figures 3.9a and 3.9b for loose and medium dense sand cases, respectively.

A comparison between the predicted (Equation 15) and numerical (PLAXIS) p-y curves for the frictional wall indicates an excellent match between the curves at all levels of wall displacement and for almost all depths considered. The only exception is the p-y relationships predicted for depth of 7.0m and 8.0m where some discrepancy is observed, particularly at larger wall displacements. For all practical purposes, this discrepancy is considered to be relatively small and insignificant. It could be concluded with certainty that the relationship that is presented mathematically in Equation (15) is capable of producing realistic and representative model predictions for the p-y relationships of frictional rigid walls supporting cohesionless backfill.

### G. Proposed Empirical P-Y Model

In the previous section, the applicability of Equation 15 in predicting the p-y curves for frictional walls was validated. In the validation, the variations of the lateral earth pressures $\sigma_{h,i}^{nf}$ and the interface shear stresses $\tau_i$, with wall displacement were extracted from the FE results. A major objective of this study is to develop a methodology or a framework for formulating and calibrating a simplified empirical model for predicting the "at-rest to active" p-y response for rigid walls. The simplified
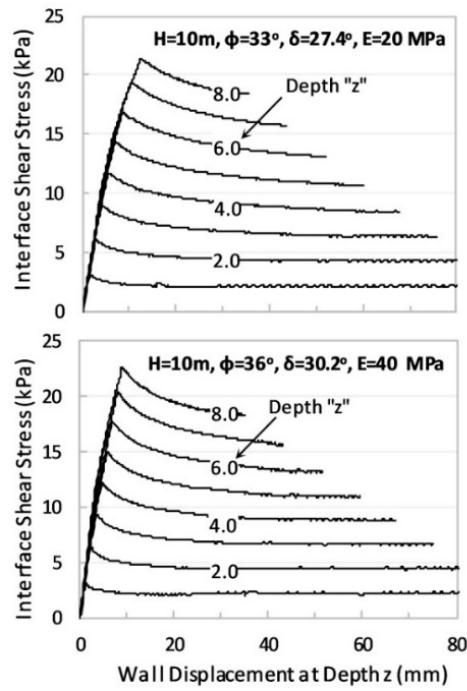
Figure. 3.8 Shear stress at wall interface for frictional wall for the cases of loose and medium dense sand.
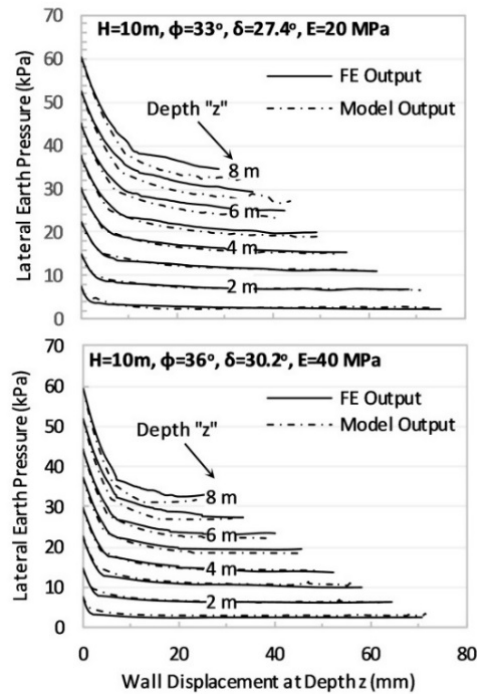


Figure 3.9 Comparison between predicted (Eq 15) and numerical p-y relationship for a 10m wall in (a) loose sands and (b) medium dense sands

model will utilize Equation 15 with the exception that the variations of $\sigma_{h,i}^{nf}$ and $\tau_i$ with displacement will be modeled using empirical equations. These empirical models are presented in the following sections.

### H. Modeling P-Y Curves for Non-Frictional Walls

The objective of this section is to develop an empirical model that is capable of predicting the p-y response for non-frictional walls with different heights and different sand densities. For that purpose, the finite element analysis was expanded to include 5m and 15m wall heights. The effect of wall height on the p-y response for the case of loose sand for depths ranging from 1m to 4m is presented in Figure 3.10a. Results show that the p-y relationship at any given depth is significantly affected by the height of the wall. The amount of wall displacement needed for active limit states to be mobilized are the smallest for the 5m-high wall followed by the 10m and 15m high walls, respectively. These observations are also relevant to the medium dense and dense sand backfill cases (not shown for brevity).

The results in Figure 3.10a indicate that any proposed p-y relationship for non-frictional walls has to include the height of the wall in its formulation. A representative parameter that could be used to normalize the p-y response while including the wall height in addition to the wall displacement "y" is the wall "distortion" $\theta_w$, which is defined as $\frac{y}{H_{wall}-z}$ for a wall that is subjected to pure rotation. For a wall that is subjected to both rotation and translation (as is the case in this study), the wall "distortion" $\theta_w$, could be defined as $\frac{y}{H_{eff}-z}$ where $y$ is the horizontal wall displacement at depth $z$, $H_{eff}$ is the effective wall height measured from the top of the wall to its

fictitious point of rotation at the bottom (see Figure 3.11), and $z$ is the depth at which the p-y curve is to be determined. If the bottom wall displacement is assumed to be a fraction $U_b$ of the top wall displacement, the effective length of the wall can be calculated as:

$$H_{eff} = H_{wall} \cdot \left( \frac{1}{1-U_b} \right) \tag{16}$$
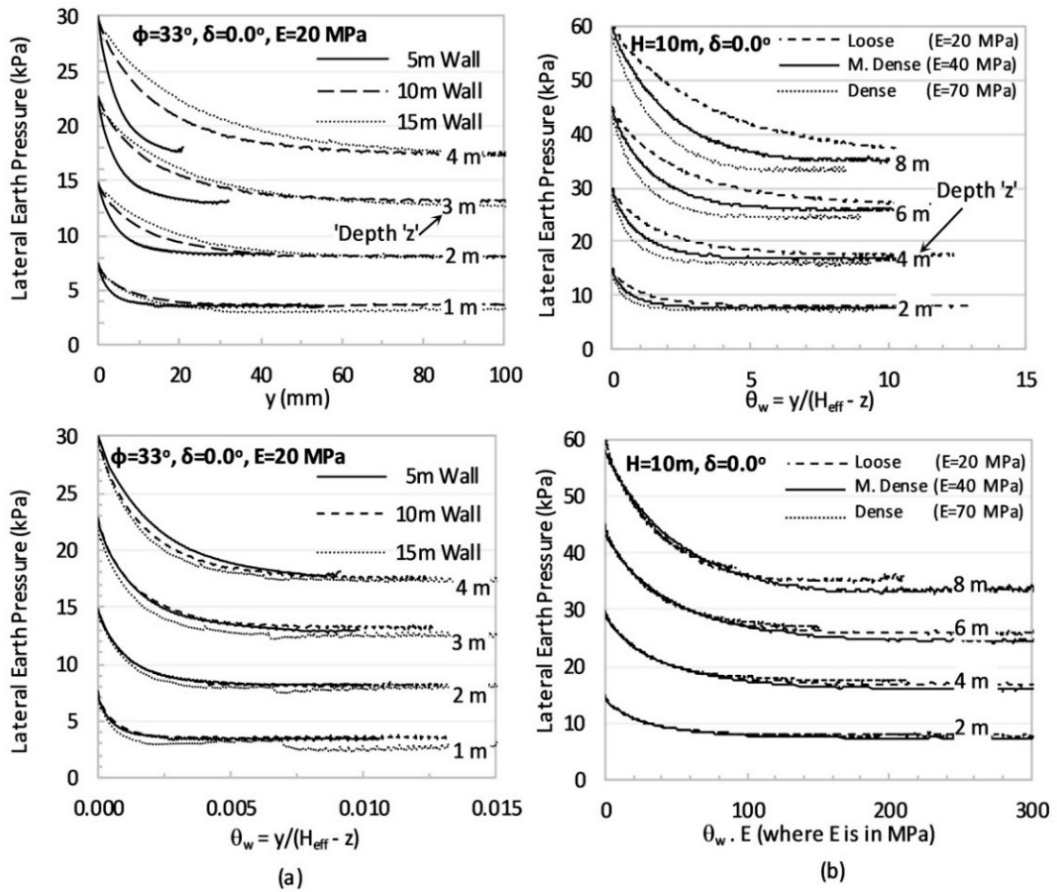


Figure 3.10 (a) Effect of wall height on p-y response (b) Effect of soil modulus on $p - \theta_w$
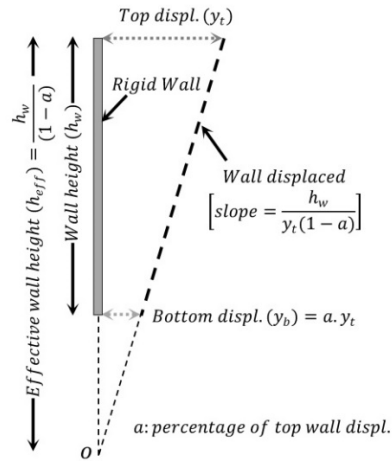
Figure 3.11 Definition of effective wall height $H_{eff}$

P-y curves that are presented in normalized format ($p - \theta_\omega$ instead of p-y) are plotted in Figure 3.10a for the case of loose sand. Results in Figure 3.10a indicate that presenting p-y curves in the form of $p - \theta_w$ curves leads to a normalized response that could be modeled to be independent of the wall height. Results for cases involving medium dense and dense sand backfills indicated that this observation was valid irrespective of the sand density. Eliminating the effect of the wall height in predicting the p-y response at different depths is key for generalizing the p-y relationship and constitutes the first step in developing simplified empirical normalized p-y curves for non-frictional walls

The other main parameter that was shown to affect the p-y curves for non-frictional walls is the soil density as reflected in the moduli of elasticity and the friction angle. To study the effect of soil density on the p-y response, three cases involving 10m high walls retaining loose ($E20$), medium dense ($E40$), and dense sand ($E70$) were investigated. FE analyses for each case were conducted using the corresponding soil properties indicated in Table 1. Normalized $P - \theta_w$ curves for depths of 2m, 4m, 6m,

and 8m for each case of soil stiffness are plotted on Figure 3.10b. As expected, results on Figure 3.10b indicate that denser sands portray $P - \theta_w$ responses that show faster mobilization of active conditions compared to sands with lower density and stiffness.

In an attempt to normalize the $P - \theta_w$ response to incorporate the effect of soil stiffness, the lateral earth pressure curves in Figure 3.10b where plotted versus wall distortion $\theta_w$ multiplied by the soil modulus $E$ on Figure 3.10b. The lateral stress variations with $\theta_w E$ at different depths show an acceptable degree of normalization between the loose, medium dense, and dense sand cases. It could thus be concluded that the $P - \theta_w E$ relationship could be used as a basis for developing a simplified empirical model for the p-y response of non-frictional walls. Note that $E$ is represented by the secant stiffness $E_{50}^{ref}$ in the balance of this paper.

Different expressions have been proposed in the literature for modeling the p-y backbone curve in soil-structure interaction problems. These expressions vary from simple bi-linear models to more complex non-linear stitched models and hyperbolic models. In this study, the backbone model adopted for the prediction of the $p - \theta_w E$ relationship of non-frictional walls entails a hyperbolic model that simulates the $p - \theta_w E$ response starting from at-rest conditions and ending at the onset of active limit state pressures computed theoretically using Coulomb theory. Once the active lateral stresses are mobilized, they remain constant until the final position of wall displacement is reached. The proposed non-linear hyperbolic model $p - \theta_w E$ is presented in Figure 3.12 and has the following mathematical form:

$$p(\theta_w E) = - \frac{\theta_w E}{\left(\frac{1}{C_o} + \frac{\theta_w E}{\Delta p}\right)} + p_o \tag{17}$$

where $\Delta p$ is the drop in the lateral stress from the at-rest condition to the active condition modified by a reduction factor $R_f$ to enhance the fit to the FE-derived curves ($\Delta p = p_o - p_a/R_f$), $p_o$ is the initial at-rest pressure computed as $k_o.\gamma.z$, $E$ is the soil's modulus expressed in kPa, and $C_o$ is the initial slope of the hyperbolic curve.

To find the values of $R_f$ and $C_o$, a non-linear regression analysis was conducted on the normalized $p - \theta_w E$ curves taking into consideration all the cases analyzed in this study (different wall heights and different sand densities and stiffnesses). The regression analysis indicated that a constant reduction factor $R_f$ of 0.7 was sufficient to accurately model the hyperbolic portion of the $p - \theta_w E$ response. On the other hand, the regressed values of $C_o$ indicated that $C_o$ is a function of the friction angle of the sand $\phi$ and the wall height $H_{wall}$. The dependency of $C_o$ on $\phi$ and $H_{wall}$ could be simply modeled using the linear relationships presented in Figure 3.13 to cover the range of typical wall heights and friction angles considered in practice.
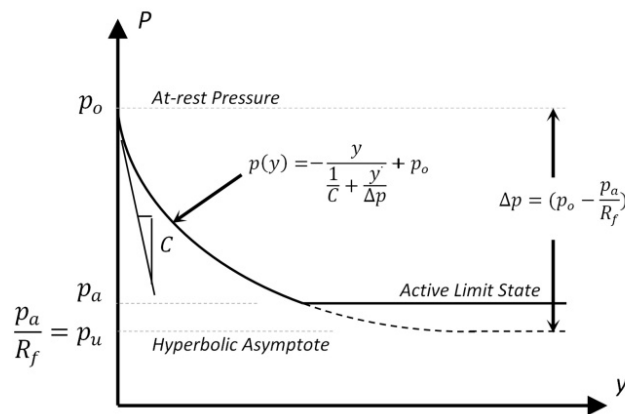


Figure 3.12 Sketch of the proposed hyperbolic model.
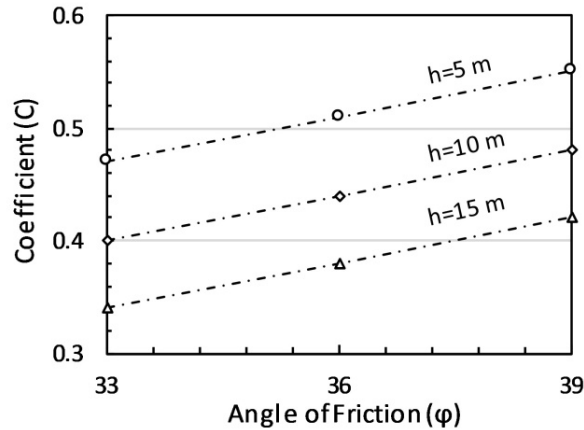
Figure 3.13 Values of C used in hyperbolic function.

The accuracy of the simplified normalized hyperbolic model in fitting the FE-derived $p - \theta_w E$ curves for non-frictional walls is tested in Figure 3.14 for both loose and dense sand cases retained by walls with heights ranging from 5m to 15m. The simplified model (Equation 17) that is bounded by the theoretical Coulomb active pressure provides an excellent fit to the FE-derived data. Some slight deviations are observed at active conditions for cases of low depths. These slight deviations are expected and attributed to charging the soil with a minimum cohesive intercept of 1 kPa in order to stabilize the FE model.

At any given depth z, the empirically derived $p - \theta_w E$ curves on Figure 3.14 can be predicted using information about the height of the wall, unit weight, modulus of elasticity and friction angle of the soil, and the depth z at which the curves are to be evaluated. These empirically derived curves provide an alternative for running expensive finite element analyses to determine the p-y curves for non-frictional walls supporting sand backfill.

# I. Modeling Interface Frictional Stresses Versus Displacement

The interface frictional stresses at the wall-soil boundary for different depths were extracted from PLAXIS 2D and plotted over the range of wall displacements ($\tau_z - y$ curves) in Figure 3.15. Cases of different wall heights and soil relative densities were considered. When the wall is in the at-rest condition, no shear stresses develop at the soil-wall boundary. As the wall displaces in the active direction, differential movement at the soil-wall interface occurs initiating upward shear stresses at the wall boundary. If lateral soil pressure is held constant with wall movement, $\tau_z - y$ curves should register a linear increase in the $\tau_z$ with wall movement. However, Figure 3.15 indicates a slight deviation from the linear behavior as noticed in the first segment of the $\tau_z - y$ curve. This deviation is attributed to the decrease in the horizontal normal stresses with wall displacement as the lateral stresses decrease towards active stresses. This becomes more pronounced in the second part of the $\tau_z - y$ curve which marks the region of plastic behavior in the material. This part of the curve shows a decrease in shear stress that is directly proportional to the decrease in lateral stresses over the same range of wall displacements. Once active pressure is reached, shear stresses stabilize approaching a theoretical value which is equal to the vertical component of the Coulomb active stress. This value can be computed using Equation 18 such that:

$$\tau_a = k_a . \gamma . z \times \sin{(\delta)} \tag{18}$$
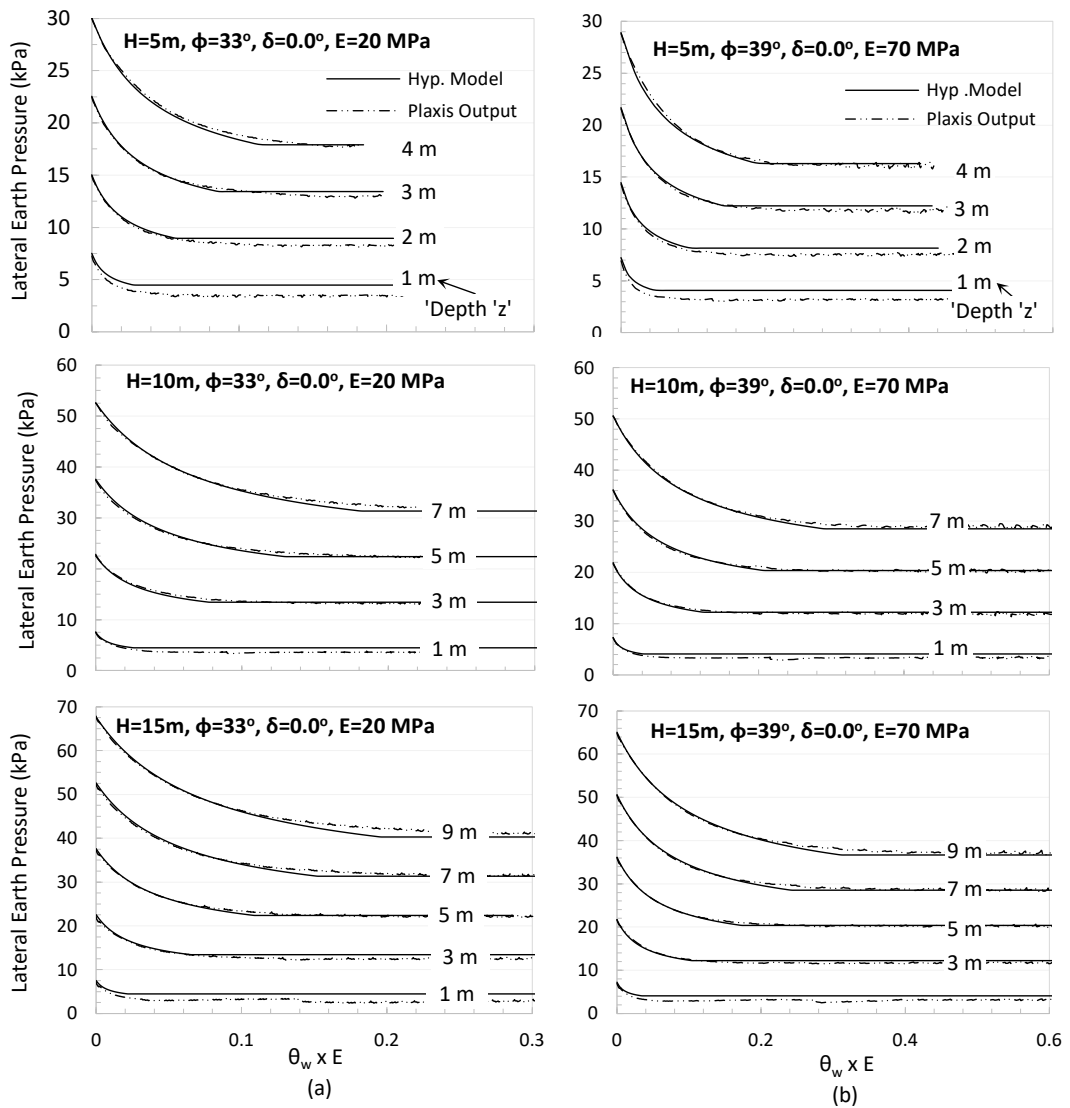
Figure 3.14 Verification of hyperbolic model on 5m, 10m, and 15 non-frictional wall retaining loose and dense sand.

Modeling the non-linear features exhibited in the FE-derived $\tau_z - y$ relationship as reflected in Figure 3.15 requires a complex mathematical model. To simplify the model, a decision was made to capture the relationship with an elastic-perfectly plastic model whereby the initial slope is modeled with a linear segment that ends at a wall displacement corresponding to the theoretical active shear stress calculated from Equation (18).
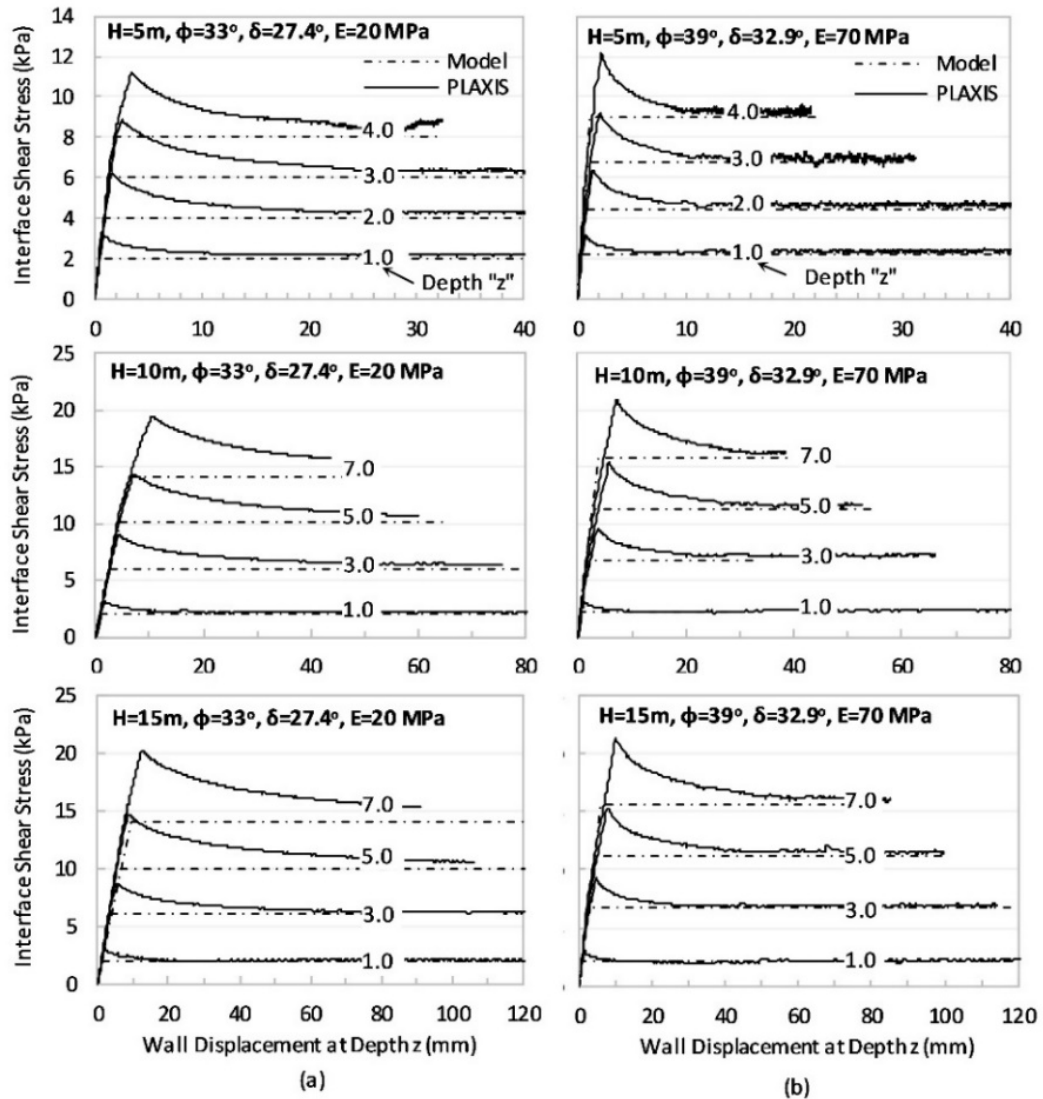
Figure 3.15 Interface stress mobilization for 5, 10, and 15m walls retaining loose and dense sand.

The only unknown parameter in this proposed bilinear $\tau_z - y$ relationship is the slope of the linear portion, $s$. A non-linear regression analysis was conducted on the FE-derived slopes of the $\tau_z - y$ relationship to calibrate a simple empirical relationship that allows for predicting the slope, s. The proposed slope of the $\tau_z - y$ relationship can be expressed as follows:

$$S_z = \left(\frac{\gamma.z}{P_a}\right)^n \times \frac{G}{H_{eff}} \times \frac{1}{\tan(\delta)^m} \qquad (19)$$

Equation (19) accounts for the backfill soil stiffness through the shear modulus $G$, the height of the wall through the effective wall height $H_{eff}$, the interface characteristics through the interface friction angle $\delta$, and the embedment depth through the fraction given by $\left(\frac{\gamma.z}{P_a}\right)^n$. It is found that a value of 0.1 given for $n$ best represents the data. $P_a$ is the atmospheric pressure in kPa. The shear modulus $G$ can be derived from the Young's modulus $E$ and Poisson's ratio $\nu$. The main empirical parameter that needed to be calibrated in Equation 19 is $m$. A comprehensive sensitivity analysis indicated that $m$ is a function of the interface friction coefficient $\tan(\delta)$ and the interface reduction factor $R$, defined as the ratio $\left[\frac{\tan(\delta)}{\tan(\phi)}\right]$. Since all the finite element runs that were conducted in this study for frictional walls involved an R of 0.8, additional cases where analyzed with interface reduction factors of 0.6 and 1.0 to establish a general empirical relationship that would allow for estimating the parameter $m$ for cases involving interface reduction factors that are generally used in practice. The numerical results for the new cases (R = 0.6 and 1.0) were combined with the cases of R = 0.8 and a non-linear regression analysis was utilized to find the expression of $m$ as reflected in Equation 20 such that:

$$m = 8.4 \times R^{0.6} \times e^{2.0 \tan(\delta)^2} \qquad (20)$$

Combining Equations (18), (19) and (20), the interface shear stress($\tau$) at a given depth (z) and wall displacement ($y_i$) can be expressed as:

$$\tau_{i,z} = \begin{cases} S_z.y_i, & \text{if } y_i < \frac{\tau_a}{S_z} \\ \tau_a, & \text{otherwise} \end{cases} \qquad (21)$$

The empirically derived $\tau$ (Equation (21)) is plotted against the interface shear stress extracted from the FE analysis for three wall heights and two relative densities (loose and dense) in Figure 3.15. It can be seen that the model can predict the elastic and the active limit state of the $\tau_z - y$ curve accurately. The discrepancy recorded between the two models over a significant part of the displacement range could be considered to be substantial. However, as will be shown in the next section, its effect is rather insignificant on the final result. A simple bi-linear $\tau_z - y$ model is considered to be advantageous provided that the resulting accuracy in predicting the final p-y response of the frictional wall is not compromised.

## J. Verification of the Empirical P-Y Model

In previous sections, it was shown that the p-y relationship of a frictional wall as reflected in the variation of $\sigma_{hi}^{f}$ with wall displacement can be predicted using Equation (15) provided that the variations of the interface shear stress $\tau_i$ and the lateral earth pressure of an equivalent non-frictional wall $\sigma_{h,i}^{nf}$ with displacement are available as input. In this section, the empirical models that were derived for the variations of $\sigma_{h,i}^{nf}$ and $\tau_i$ with displacement will be used (instead of the FE-predicted relationships) to predict the p-y relationship of the equivalent frictional wall.

The comparison between the FE-derived p-y curves and the curves obtained using the empirical models for $\sigma_{h,i}^{nf}$ and $\tau_i$ is presented in Figure 3.16. The comparison is shown for 5m, 10m, and 15m walls that are supporting loose and dense sand. Results indicate that the empirically derived p-y curves provide a reasonable representation of the FE-derived p-y relationships. These results are very encouraging given the

simplified nature of the hyperbolic and bi-linear models adopted for $\sigma_{h,i}^{nf}$ and $\tau_i$, respectively. These models require as input typical soil properties and information about the wall height and associated wall movement. The mathematical formulation of the models is relatively simple and amenable to coding within structural engineering software packages that aim at modeling the soil around the wall as a series of springs.

### K. Example Problem

To illustrate the effectiveness of the empirical p-y model in predicting the response of general cases with wall heights and soil properties that are different than those used in the calibration of the model, an arbitrary example problem that involves a 12m rigid wall with an interface reduction factor of 0.6 is assumed to retain granular soil with properties shown in Table 3.2. Integrating the $\sigma_{hi}^{nf}$-model as expressed in Equation (17) and the $\tau_i$ −model as expressed in Equation (21) into Equation (15) and running a step by accuracy showing the versatility of the above methodology, even for cases with soils step analysis over the range of wall displacements, p-y curves for the 12m rigid wall are constructed and presented in Figure 3.17. The empirically derived p-y curves are compared to the numerically derived (PLAXIS 2D) curves on the same figure. Results indicate that the proposed model is capable of capturing the FE behavior with sufficient having friction angles and stiffness characteristics that are different than those used to calibrate the model.

**Table 3.2**. Soil properties for the validation example used in PLAXIS 2D

|  | M. Dense |
|---|---|
| Soil Unit Weight, $\gamma (kN/m^3)$ | 17.0 |
| Initial Void Ratio, $e_{int}$ | 0.615 |
| Sec. Stiffness, $E_{50}^{ref} (MPa)$ | 45 |
| Tang. Stiffness, $E_{oed}^{ref} (MPa)$ | 45 |
| Unload/ reload Stiffness, $E_{ur}^{ref} (MPa)$ | 200 |
| Power of stress dependency of E, m | 0.4 |
| Cohesion, $C_{ref}' kN/m$ | 1.0 |
| Friction Angle, $\varnothing'(°)$ | 34 |
| Dilation Angle, $\psi(°)$ | 7 |
| Poisson' Ratio, $v'$ | 0.3 |
| Reference Stress, $p_{ref} (kPa)$ | 100 |
| Failure Ration, $R_f$ | 0.95 |
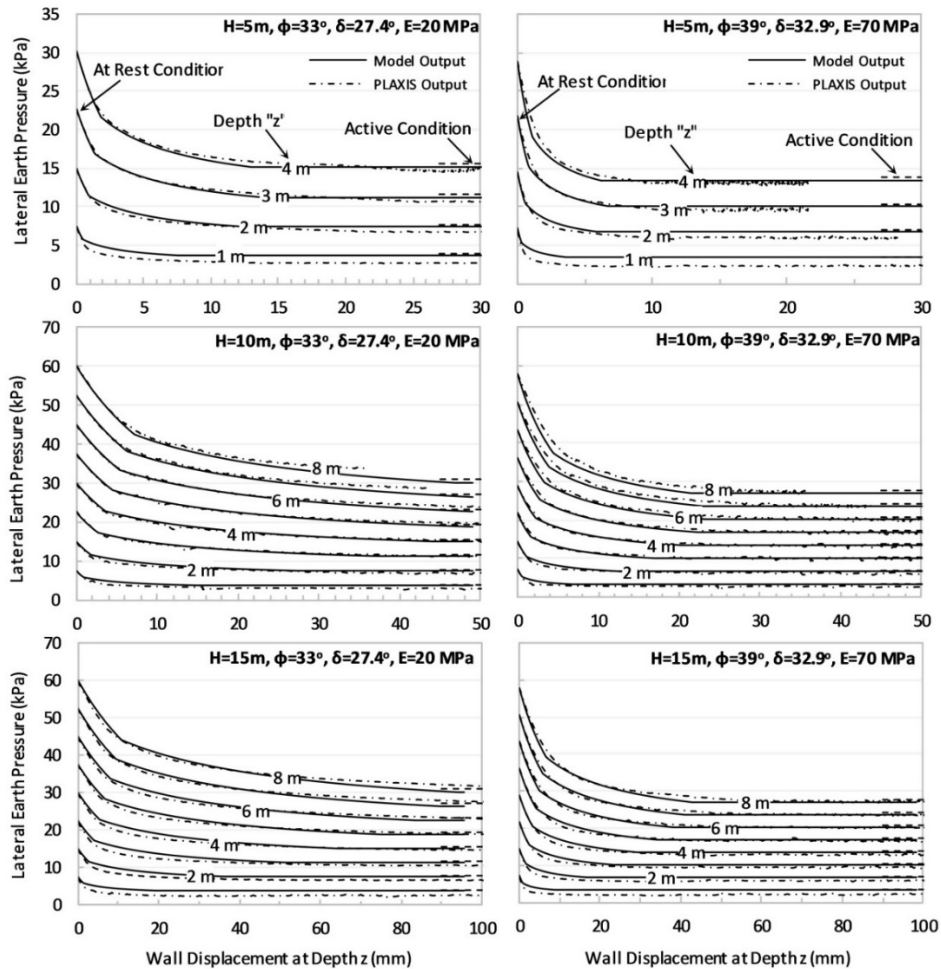


Figure 3.16 Comparison between FE-derived p-y curves for 10m frictional wall and those predicted using Equation (15) and empirical models for $\sigma_{h,i}^{nf}$ and $\tau_i$ as input
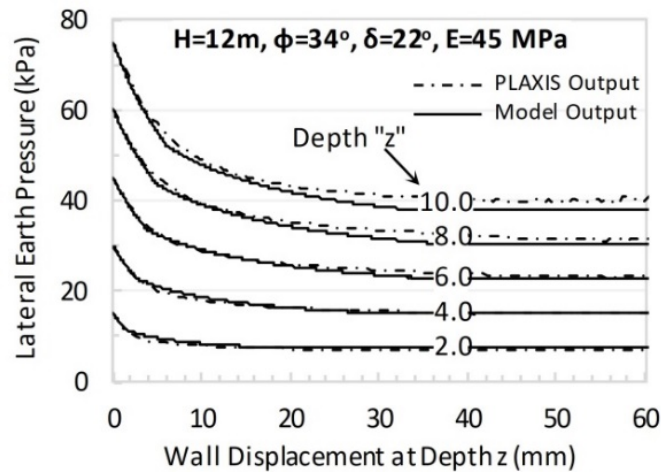
Figure 3.17 Comparison between FE-derived p-y curves for 12m frictional wall and those predicted using Equation (15) and empirical models for $\sigma^{nf}$ and $\tau$ as input.

## L. Conclusions

In this study, finite element analyses were conducted to model the mobilization of active earth pressure behind rigid basement walls. The intent is to investigate the possibility of generating p-y relationships that could be used in modeling soil response analogous to those used in pile analysis and design. Based on the results, the following conclusions can be made:

1.    The use of the Hardening soil model in the FE analysis resulted in p-y relationships that are reasonable. The resulting p-y relationships at different depths were found to be sensitive to the relative density of the soil and the height of the wall, which had a direct effect on the magnitude of the local displacements required for active conditions to be mobilized. Results showed that the 1.3mm displacement criterion that is typically referenced in the literature for the mobilization of active conditions in p-y curves is not realistic for full scale rigid walls.

59

2.      The p-y curves of rigid frictional walls were found to be steeper than

identical p-y curves for non-frictional walls. The p-y curves in the non-

frictional cases are smoother, with an initial response that is less steep and a

reduction in stiffness that is gradual.  These differences in response could be

attributed to the mobilization of frictional shear stresses at the soil wall

interface in the case of the frictional wall cases.

3.      The p-y relationship for a frictional wall could be derived from the p-y

relationship of an identical non-frictional wall provided that the variation of the

frictional shear stresses along the wall soil interface with displacement could

be identified. To validate this finding, the variations of the lateral earth

pressures $\sigma_{h,i}^{nf}$ and the interface shear stresses $\tau_i$, with wall displacement were

extracted from the PLAXIS results and used in Equation 15 to predict the

variation of $\sigma_{h,i}^{nf}$ with displacement. Results of the predicted p-y curves were

satisfactory when compared to the FE-predicted p-y curves of the frictional

wall.

4.      A simplified empirical model was developed to model p-y curves for

non-frictional walls. The model is hyperbolic in nature and relates the lateral

earth pressure mobilized behind a rigid non frictional wall to the wall distortion

multiplied by the modulus of elasticity of the soil$(p - \theta_w E)$. The use of $\theta_w E$

in the simplified model as the main independent variable (instead of y) was

needed to obtain a generalized normalized response that caters for cases with

different wall heights and different soil stiffness. The parameters of the

hyperbolic model were calibrated using regression. The simplified model was

shown to provide acceptable representation of the p-y response of non-frictional walls with different heights and sand densities.

5.      A simplified empirical bilinear model was also developed to represent the mobilization of the frictional shear stresses at the soil-wall interface $\tau_i$ with displacement. Validation experiments indicated that the utilization of this simple model with the hyperbolic $(p - \theta_w E)$ model for non-frictional walls could provide realistic estimates of the p-y response of frictional walls without the need for expensive finite element analyses.

It is worth noting that the intent of this study is to provide a methodology for modeling p-y curves for cohesionless soils that are used as backfill behind rigid basement walls. In the finite element analyses that were conducted, the soil properties that were used pertain to those of Ottawa sand. As a result, the numerical results and the associated simplified model parameters are expected to be affected by the choice of the soil type used. Moreover, while the choice of the hardening soil model is adequate for loose and medium dense sands that do not exhibit significant post-peak softening in the stress-strain relationship, its use is questionable for dense sands that exhibit significant dilation and softening at large strains. The use of the hardening soil model for dense sands is a limitation that needs to be investigated further in future studies.

# CHAPTER 4

# Passive P-y Curves for Rigid Basement Walls Supporting Granular Soils

## A. Introduction

For structures with underground basement walls, the soil-structure-interaction (SSI) between the side soil and the walls affects the response of the system, particularly under cyclic loading conditions. In the context of performance-based design, there has been interest in quantifying the relationship between the lateral earth pressure and the wall displacement using the concept of p-y curves by replacing the homogeneous soil continuum by a series of springs that mimic the soil behavior adjacent to the substructure. The p-y method has been advocated and applied by geotechnical and structural engineers in the design of laterally loaded piles (Matlock 1970, Reese et al. 1974, API 1993). The problem for piles has been extensively studied using full scale field tests, centrifuge tests, and 3D finite element analyses (Boulanger et al. 1999).

On the other hand, very limited studies have been conducted on the mobilization of lateral earth pressure behind rigid walls in the context of p-y curves. Briaud and Kim (1998) were the first to recommend p-y relationships for the analysis and design of tieback walls. These p-y relationships were calibrated/back calculated using data collected from full scale tests on walls in sand. Briaud and Kim (1998) state that the lateral earth pressure that is exerted by the soil on the wall is bounded by the active and passive earth pressure conditions. Based on the data collected, they recommend that the active earth pressure could be assumed to be mobilized at wall

movements of 1.3mm (away from the retained soil) and the passive earth pressure at wall movements of 13mm (into the retained soil). El Ganainy and El Naggar (2009) and Saad et al. (2016) adopted this p-y relationship as the backbone curve for the lateral pressure-lateral deflection relationship used for modeling the side soil in their analysis of the response of buildings with underground stories.

P-y curves were also incorporated in the analysis of lateral SSI for walls under dynamic loading. In the dynamic analysis, the near-field soil (in contact with the wall) is customary modeled by a series of link elements (springs) with an axial stiffness that is characterized by a given p-y curve. Richard et al. (1999) modeled the near-field soil by a series of springs having a bilinear p-y curve consisting of an elastic portion bounded by upper and lower limits defined by active and passive limit states, respectively. The elastic stiffness of the near-field soil was modeled by $k_s = 1.35 G_z/H \sqrt{z/H}$, $G_z$ being the shear modulus of the soil at a depth $z$, $H$ the height of the wall, and $z$ the depth at which the p-y response is being modeled. Maleki and Mahjoubi (2010) used the same p-y model for defining the stiffness of the spring elements in the study of the effect of wall flexibility on the soil resistance during dynamic loading.

In reality, the relationship between lateral earth pressure and wall displacement is expected to be complex and is affected by the height of the wall, the relative density of the backfill material, the interface friction between the wall and the soils, the non-linearity of the soil response, and the type of wall movement (translation and/or rotation). Elchiti et al. (2017) conducted a preliminary investigation of the p-y response of rigid basement walls in the active state of loading and concluded that the above-mentioned complexities in the relationship between lateral earth pressure and wall

displacement could be captured using numerical analyses. The analyses conducted in Elchiti et al. (2017) were however restricted to rigid basement walls that are simplistically assumed to be fixed at their base (supported on rock) and subjected to active loading.

Numerical results from soil structure interaction analyses conducted in Saad et al. (2016) on five, ten and fifteen storey buildings with underground stories ranging from zero to five basement floors indicated that the maximum base shear at the ground level was governed by the lateral earth pressures mobilized in the retained soil behind the wall during seismic excitation. In particular, the lateral soil stresses that were mobilized as the wall was pushed towards the soil (passive loading direction) dictated the design base shear needed for the design of the shear walls. These results point to the need for realistic models that could describe the p-y relationship for rigid retaining walls to be used as input in robust soil-structure-interaction problems in the context of performance-based design. Such p-y relationships could be incorporated in commercial structural analysis software in the form of non-linear springs that describe the lateral pressure versus lateral displacement relationship. This is consistent with the p-y curves concept commonly used to model the reaction of the soil for laterally loaded piles.

The goal of this paper is to shed light on the mechanics of the soil-structure interaction between rigid basement walls and granular backfill soil in the passive state of loading. This is achieved by (1) building a PLAXIS 2D model that incorporates the wall, backfill soil and foundation soil (2) investigating the effect of the height of wall, soil properties, and interface friction angle on the lateral p-y response, and (3) utilizing

the numerical results to establish a simple empirical model that is capable of predicting the p-y response behind rigid basement walls in the passive state of loading.

## B. Finite Element Modeling

### 1. *PLAXIS 2D Model*

The finite element model (FEM) of the rigid retaining wall and the backfill material was built in PLAXIS 2D and presented in Figure 4.1. The model consisted of four elements: a rigid wall, a semi-infinite half-space backfill soil, a semi-infinite half space subsoil, and an interface soil layer acting as a soil-wall boundary.

The rigid wall was modeled as a rectangular plate element. The wall is moved incrementally in the passive direction using a trapezoidal prescribed displacement. Differential displacement between the top and bottom of the wall results in a combined rotational/translational wall movement. The horizontal prescribed displacement also ensures that no vertical movement or bending of the plate element can occur. A rotation/translation wall movement was chosen based on the results presented in Saad et al. (2016) for basement wall displacements under real earthquake excitations. The study revealed that walls in buildings that included multiple basements showed more-or-less rigid wall rotations with maximum lateral wall displacements recorded at the top of basement wall (ground level) and minimum lateral wall displacement recorded at the level of foundations. The magnitude of the horizontal wall displacement at the foundation level was evaluated to be between 5% and 20% of the top wall displacement.
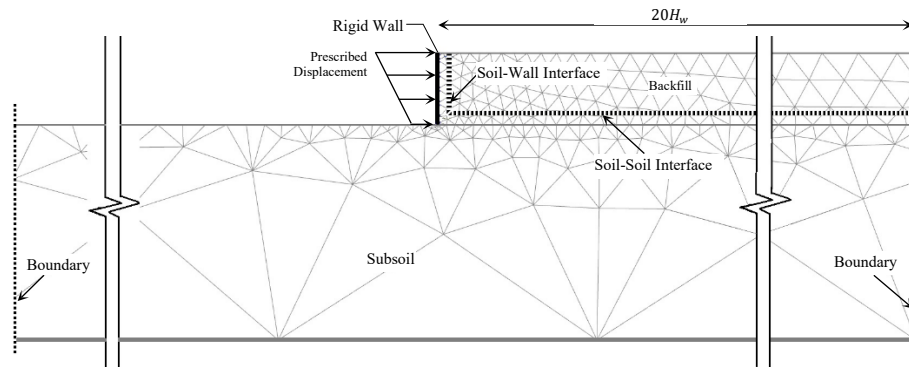
Figure 4.1 Finite element model

Six-node plane strain triangular elements were used to mesh the subsoil and backfill continua. The finite element mesh was adaptively refined to converge to an element distribution with varied sizes ranging from very fine triangular elements at locations of stress concentration at the wall-soil and soil-soil interfaces to course triangular elements at the boundaries. Moreover, an interface layer was constructed at the soil-wall boundary and at the backfill-subsoil boundary. Modeling an interface layer at the boundary of two materials is desirable for several reasons. It allows for the reduction in soil strength and soil stiffness at the interface as well as for the formation of differential displacement (slippage) between the adjoining elements thus minimizing stress build-up at points of stress concentration. Interface layers in PLAXIS are modeled as rectangular elements with zero thickness. The property of the interface layer in PLAXIS is given through a reduction factor $R_{int}$. At the soil-wall interface, $R_{int}$ was varied in accordance with the parametric study presented in the following section, while at the soil-subsoil interface, a value of 1.0 was selected.

The left and right boundary conditions of the finite element model are selected to limit horizontal movements due to applied wall displacement while simultaneously

allowing free vertical displacement at the boundaries. The bottom subsoil boundary is modeled as a full fixity. The length of the retained soil and the depth of the subsoil layer are selected following a comprehensive sensitivity analysis. Inadequate length of the retained soil will result in the formation of back pressure at the backfill boundary. Several lengths of soil ($6H_w, 10H_w, 15H_w, 20H_w$) were investigated in the sensitivity analysis. Significant magnitudes of back pressure were observed for the backfill length of $6H_w$. However, back pressure magnitudes dropped significantly with an increased backfill length of $10H_w$ and became negligible at a backfill length of $15H_w$ and non-existent for a backfill length of $20H_w$. As a result, a $20H_w$ backfill soil was used in the study. A similar analysis was done for determining the required depth of the subsoil layer. The sensitivity analysis revealed that a subsoil depth of $3H_w$ is sufficient to minimize boundary effects.

The effect of bottom wall translation on passive p-y response was investigated assuming bottom wall displacements that are $5\%, 10\%,$ and $20\%$ of the top wall displacement. This range of bottom wall displacements is consistent with numerical results presented in Saad et al. (2016) for full scale reinforced concrete buildings that are subjected to earthquake shaking. The effect of the assumed bottom wall displacement on the numerically derived p-y curves is presented in Figure 4.2 for a 10m wall retaining medium-dense sand. The p-y curves are presented for depths ranging from 1 to 7m. The results indicate that bottom wall displacements ($y_b$) with a magnitude ranging from 5% to 20% of the top wall displacement ($y_t$) have an insignificant effect on the p-y response. Based on these results, a decision was made to adopt a bottom wall displacement that is equal to 20% of the top wall displacement in the remainder of this study.
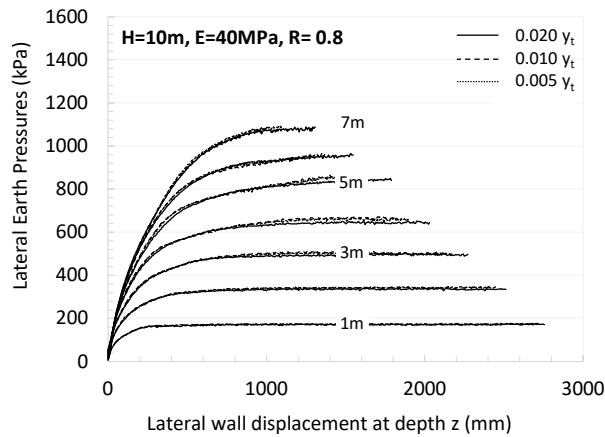
Figure 4.2 Effect of bottom wall translation on P-y response

## 2. *Constitutive Soil Model*

Elchiti et al (2017) compared the response of granular backfill in active wall displacement for soil modeled using the traditional Mohr-Coulomb model and the more advanced Hardening Soil model available in PLAXIS. They concluded that the results of the Mohr-Coulomb model exhibit signs of numerical instability at relatively small wall displacements. These numerical instabilities were attributed to the elastic-perfectly plastic nature of the Mohr-Coulomb model, whereby soil elements in the passive failure wedge will yield early on in the deformation process therefore causing loss of numerical stability at larger deformations. On the other hand, the Hardening Soil model yielded a more stable response that could predict the p-y behavior of the retained granular soil up to large wall displacements. Accordingly, the Hardening Soil model was adopted in this study to model the constitutive response of the backfill and subsoil in the FE analysis.

The Hardening Soil model in PLAXIS is an advanced non-linear model that assumes a hyperbolic relationship between stress and strain. The Hardening model adopts isotropic hardening and includes two yield surfaces to differentiate between shear and isotropic loading. The final bounding surface is based on the Mohr-Coulomb

failure envelope with a non-associated flow rule using the dilatancy angle as the non-normality parameter. With respect to its stiffness behavior, the model considers stress and strain level dependency of the moduli. A hyperbolic stress - strain relation is considered between the deviatoric stress and the major principal strain to account for strain dependency, while a power law is adopted to consider stress dependency, and the user specifies the moduli at a certain reference pressure. In this study, the parameters utilized in the Hardening soil model (Table 4.1) were adopted from Skeini (2015) and are consistent with the behavior of loose, medium dense and dense Ottawa sand.

It should be noted that all interface soil layers in PLAXIS 2D are modeled using the Mohr-Coulomb model. When more advanced soil models are chosen, PLAXIS 2D extracts the parameters relevant to the Mohr-Coulomb model and applies the reduction factor to them to deduce the shear strength parameters that govern the soil-wall and backfill-subsoil interface responses.

### 3. *Parametric Study*

The results in this study are based on a parametric analysis that was designed and implemented to characterize the components that affect the variation of lateral earth pressure with respect to passive wall displacement. The parametric study consisted of varying (1) the height of wall, (2) the relative density (RD) of the soil and (3) the soil-wall interface reduction factor, $R_{int}$. Three wall heights, 5m, 10m, and 15m, corresponding to 2, 4, and 6 basement floors, respectively, were considered. For each wall height, loose (RD = 45%), medium-dense (RD = 67%), and dense (RD = 84%) dry granular soils were considered as backfill material. The soil properties associated with each relative density are presented in Table 4.1. Three soil-wall interface reduction

Table 4.1 Soil properties for constitutive model used in parametric study

| Parameters | Hardening Model | | |
|---|---|---|---|
| | Loose | M. Dense | Dense |
| Soil Unit Weight, $\gamma(kN/m^3)$ | 16.5 | 18.0 | 19.5 |
| Soil Relative Density $R_d$ (%) | 45 | 67 | 84 |
| Initial Void Ratio, $e_{int}$ | 0.685 | 0.615 | 0.560 |
| Sec. Stiffness, $E_{50}^{ref}(MPa)$ | 15-25 | 30-50 | 60-80 |
| Tang. Stiffness, $E_{oed}^{ref}(MPa)$ | 15-25 | 30-50 | 60-80 |
| Unload/ reload Stiffness, $E_{ur}^{ref}(MPa)$ | 200000 | 200000 | 200000 |
| Power of stress dependency of E, m | 0.4 | 0.4 | 0.4 |
| Cohesion, $C_{ref}'(kN/m)$ | 1.0 | 1.0 | 1.0 |
| Friction Angle, $\emptyset'(°)$ | 33 | 36 | 39 |
| Dilation Angle, $\psi$ (°) | 4 | 7 | 11 |
| Poisson' Ratio, $v'$ | 0.3 | 0.3 | 0.3 |
| Reference Stress, $p_{ref}$ (kPa) | 100 | 100 | 100 |
| Failure Ration, $R_f$ | 0.95 | 0.95 | 0.95 |

factors (0.6, 0.8, and 1.0) were considered in the investigation. These values were chosen to be in line with the common values used in practice for the case of granular soil bearing on concrete walls. A graphical representation of the above parametric study is shown in Figure 4.3.
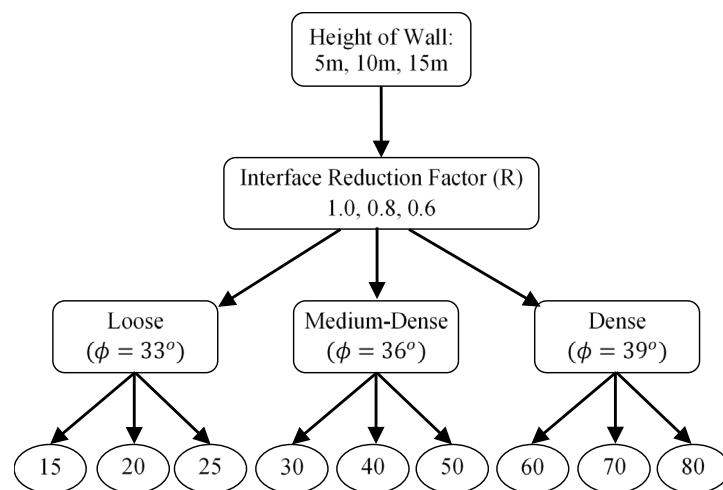


Figure 4.3 Parametric study chart

## C. Numerically derived passive p-y curves

To construct p-y curves using the FE results, lateral earth pressures at 1-m depth intervals were extracted from stress points selected at the soil-wall interface and plotted against the horizontal wall displacement at that depth. Typical p-y curves for the case of medium-dense sand retained by a 10m high wall having an interface reduction factor of 0.8 are shown in Figure 4.4. Several observations can be made based on the reported results. First, passive p-y curves exhibit a non-linear monotonic increase in lateral earth pressure ending in an asymptotic limit-state passive pressure. Second, there is a reduction in the rate of stress increase with increased wall displacement consistent with the reduction in the soil stiffness with increased strain for the hardening model used. Third, the rate at which passive pressure mobilizes behind the wall is sensitive to the embedment depth, z. P-y curves at shallower depths mobilize at faster rates than those at lower depths. This is observed by comparing the amount of wall displacement needed for the limit-state passive pressure to be reached at different depths below the ground. A comparison of the wall displacements required to mobilize the passive
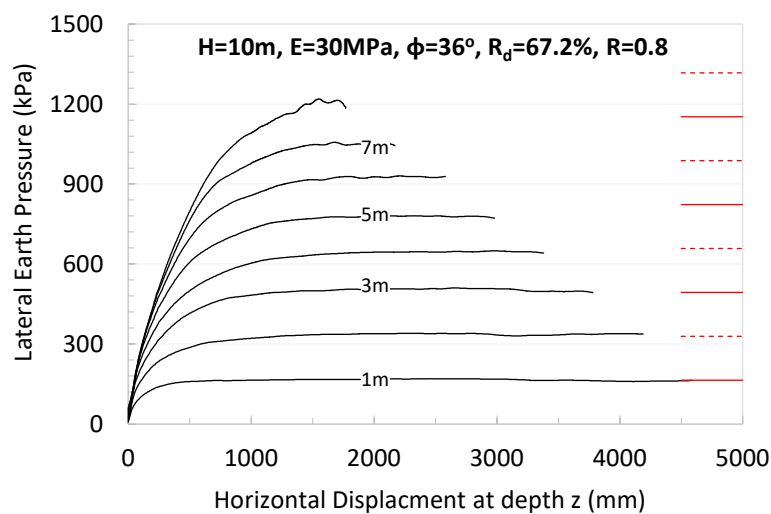


Figure 4.4 Typical passive P-y curves

pressure shows that the passive pressure is mobilized at y=600mm and y=2000mm for depths of 1m and 5m, respectively.

The large wall displacements needed for full passive pressures to be mobilized may not be reached in practical applications involving basement walls under real seismic shaking. Most building codes limit story-drift ($y_t/H_w$) to less than 2.0%, $y_t$ being the top wall displacement and $H_w$ the height of the wall. Consequently, for SSI problems, there is more value in characterizing the p-y response at relatively smaller lateral displacements that may be attained in practice. Figure 4.5 presents the early stages of the p-y response for the same wall shown in Figure 4.4. Wall displacements corresponding to 2% story drift at each depth z are marked by circles on the p-y curves. An investigation of the p-y curves in the lower displacement range indicates that non-linearity in the lateral stress-displacement response is clearly visible and is observed at early stages of wall displacement. This is essential for proposing future models for the prediction of p-y curves for performance-based design applications whereby story drift (lateral wall displacement) could be the governing design criteria. Results on Figure 4.5 indicate that the elastic-perfectly plastic p-y models that are currently being advocated in the literature (Briuad and Kim 1998, Richard et al. 1999, and Maleki and Mahjoubi 2010) would be incapable of predicting the non-linear passive p-y curves without suffering from over-prediction of the mobilized lateral pressures at different levels of wall displacement. The adoption of a depth-independent fixed lateral displacement of 13mm as a criterion for full mobilization of passive earth pressure in published p-y curve models may not be completely representative of the true response. The 13mm

displacement criterion, shown graphically in Figure 4.5, is clearly a very early estimate

for the development of full passive pressure.
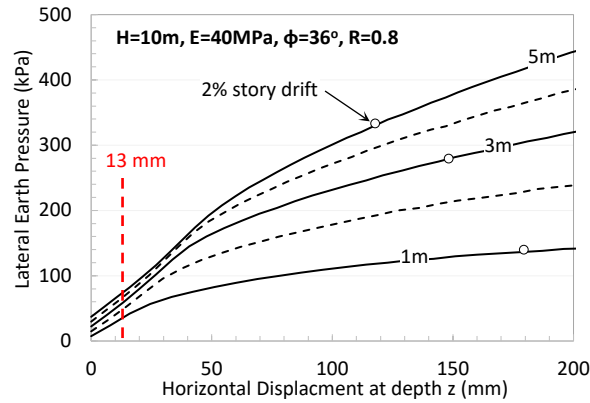


Figure 4.5 P-y curves in the practical range of wall displacements

The p-y curves in Figures 4.4 and 4.5 correspond to the case of a 10-m high

wall that is supporting medium dense sand with a modulus of elasticity of 40 MPa. The

effects of varying the stiffness of the backfill and the height of the wall on the resulting

p-y curves are presented in Figures 4.6a and 4.6b, respectively. Results on Figure 4.6a

pertain to cases where the soil modulus ($E$) was varied between 30 and 50MPa. As

expected, the p-y curves indicate that sands with a lower stiffness lead to an initially

"softer" p-y response, with lower mobilized lateral stresses at any given wall

displacement. The effect of "E" is however restricted to the initial portion of the p-y

curve with no impact on the maximum passive pressures at limit state. For any given

depth, the curves converge at a common limit state pressure at large wall displacement.

This observation is logical given that the maximum passive pressure is governed by the

friction angle of the sand and the interface friction coefficient between the sand and the

wall, and is independent of the initial stiffness, E.

73
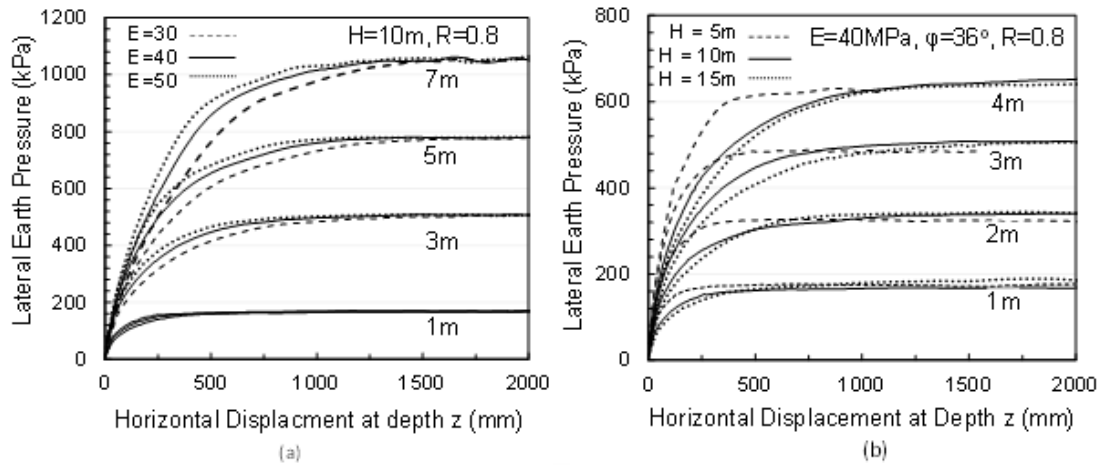
Figure 4.6 (a) Effect of soil modulus on P-y response (b) Effect of wall height of P-y response

The effect of wall height on the passive p-y response is shown in Figure 4.6b. P-y curves for wall heights of 5m, 10m, and 15m retaining medium-dense sand for depths ranging from 1m to 4m are presented in the figure. Results indicate that cases with shorter walls exhibit a stiffer (steeper) initial p-y response. The stiffer response observed in the 5-m high wall cases at any fixed wall displacement could be attributed to the larger distortion/shear strain that is expected in the soil retained by to the shorter wall. To support this statement, a sketch is presented in Figure 4.7 to show the displacement/distortion conditions in 5m and 10m high walls that are displaced such that the local wall displacements (y) at a given depth $z$ are equal in both walls. Define $\psi_1$ and $\psi_2$ as the angular distortions of the 5m and 10m walls, respectively (see Figure 4.7). As indicated in the figure, for both walls to displace the same amount $y$ at a given depth $z$, the 5m-wall will have to undergo higher angular distortions compared to the 10m-high wall. This will eventually result in the development of higher shear stresses and higher passive pressures in the shorter walls as portrayed in Figure 4.6.
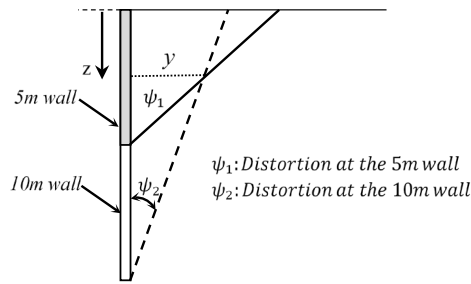
Figure 4.7 Wall distortion for 5m and 10m walls for a given displacement y at depth z

The parametric study was extended to study the effect of the interface reduction factor R on the observed p-y response. The interface reduction factor for granular soil bearing on poured concrete is commonly taken to be between 0.6 and 1.0. To study the effect of R, a 10m rigid wall retaining medium-dense soil was analyzed for R values of 0.6, 0.8, and 1.0. P-y curves for depths ranging between 1m and 7m are plotted on Figure 4.8a. At any given depth z, results indicate that the three p-y curves corresponding to the three values of R initiate from the same at-rest pressure and end at three different values of limit-state passive pressures at large wall displacements. A negligible effect of the interface friction coefficient is noted with regards to the initial part of the p-y curves which represents relatively smaller wall movements. The p-y curves for different R values diverge at wall displacements ranging from 10cm (for shallow depths) to around 40cm (at larger depths). This divergence at relatively large displacements is expected since the limit-state passive pressure is correlated with the assumed interface reduction factor, R.

The results presented in Figures 4.4, 4.5, 4.6, and 4.8a pertain to cases with medium dense sand. The effect of relative density of the retained soil on the p-y response is investigated in Figure 4.8b for cases involving a 10-m high wall and an

interface reduction factor of 0.8. Parameters representing each relative density are presented in Table 4.1 with soil moduli of 20MPa, 40MPa, and 70MPa in the case of loose, medium-dense, and dense soil, respectively. The p-y curves in Figure 4.8b point clearly to the significant effect of relative density on the p-y response. As expected, the cases with loose and medium dense sands show lower magnitudes of the limit-state passive pressure compared to the dense sand case. The effect of relative density is equally visible in the lower displacement range with stiffer responses observed in the case of dense sands.

Based on the parametric study, it could be concluded that the passive p-y response is affected by the depth below the ground surface $z$, the soil modulus $E$, the relative density, and the height of the wall $H_w$. On the other hand, the effect of the interface reduction factor R is confined to the p-y response at larger wall displacements.
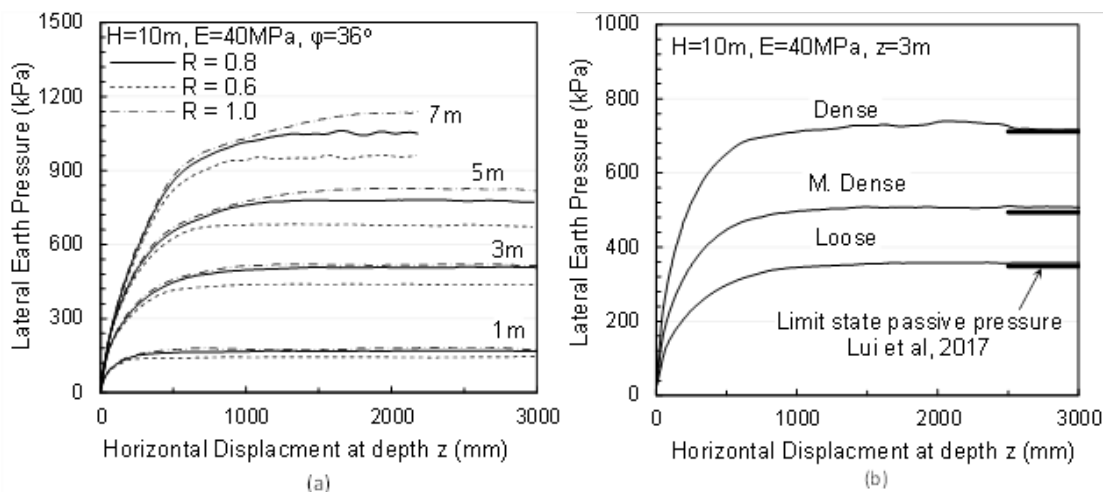
Figure 4.8 P-y response for different a) interface reduction factors b) soil relative density

### D. Empirical P-Y Model

#### 1. *Model Formulation*

Several models have been proposed in the literature for the prediction of p-y curves. These models vary in complexity and accuracy from simple elastic-perfectly plastic models (Briaud and Kim 1998) to more advanced non-linear models including power functions (Matlock 1970), nonlinear functions (Ramberg-Osgood, Reese et al., Duncan et al. 2001, API 1993) and piecewise linear models (Allotey and Naggar 2007). P-y models that are based on the Ramberg-Osgood model have been successfully employed in modeling p-y curves for piles under lateral loading. In a general context, the Ramberg-Osgood model can be expressed as:

$$p = \frac{(C_o - C_f)y}{\left[1 + \left\{\frac{(C_o - C_f)y}{p_f}\right\}^m\right]^{1/m}} + C_f y \tag{1}$$

where $C_o$ and $C_f$ are the initial tangent spring stiffness and the spring tangent stiffness at failure, respectively, $P_f$ is the spring force at the yield point, and '$m'$' is the order of the p-y curve. For the case of predicting passive pressure behind rigid walls, the expected stiffness, $C_f$, at limit-state can be considered to be equal to 0. If $m$ is taken as 1 and the lateral pressure at $y = 0$ is equal to the at-rest value ($p_o$), the Ramberg-Osgood model in Equation (1) can be simplified to:

$$p = \frac{y}{\frac{1}{C_o} + \frac{y}{\Delta p}} + p_o \tag{2}$$

where $\varDelta_p$ is the change between the initial pressure $p_o$ and the asymptotic pressure at failure $p_f/R_f$, and $R_f$ is commonly introduced to minimize fitting errors. Duncan and

Chang (1970) proposed a range for $R_f$ between 0.75 and 0.95. A sketch representing the p-y model of Equation (2) is shown in Figure 4.10. When the expression for $\Delta_p$ is replaced in Equation (2), the final form becomes:

$$p = \frac{y}{\frac{1}{C_o} + \frac{y}{\frac{p_f}{R_f} - p_o}} + p_o \tag{3}$$

The expression in Equation (3) is one form of a hyperbola. The use of this form of hyperbolic function for the prediction of p-y response is desirable for two reasons. First, it can replicate the shape of typical p-y curves that exhibit monotonic increasing pressures that tend to a defined horizontal asymptote (limit) at a decreasing rate. Second, they are easy to construct, requiring the determination of two parameters, namely the initial slope $C_o$ and the value of the passive pressure at limit-state, $p_f$.
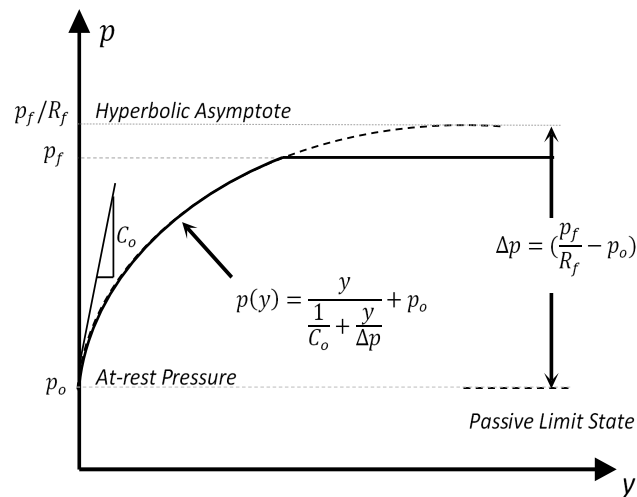


Figure 4.9 Hyperbolic model

78

### 2. *Passive Pressure ($p_f$)*

Different approaches were proposed in the literature for the prediction of passive lateral stresses behind retaining systems. These include limit equilibrium methods (Rankine 1857, Coulomb 1776, Terzaghi 1943), upper and lower bound analyses (Chen 1975; Soubra and Regenass 2000), and finite element methods (Tejchman et al., 2007; Hanna et al., 2011; Hanna and Diab, 2017).

Limit equilibrium methods are simple to implement. One of the earliest approaches for calculating $p_f$ using limit equilibrium were proposed by Rankine (1857) and Coulomb (1776). Rankine's theory predicts passive pressure accurately for smooth wall interfaces ($\delta$=0) retaining horizontal backfill, while Coulomb's theory presents a more general solution allowing for the presence of a sloped backfill and a rough wall interface ($\delta$>0). It has been shown that Coulomb's theory over predicts passive pressures for walls with $\delta > \phi/2$ (Kramer, 1996). As a result, Terzaghi (1943) proposed the use of a curved failure plane (logarithmic spiral) to enhance the prediction of passive pressure. His method was fine-tuned by several researchers to include a composite failure plane consisting of a curved segment and a straight segment (Kumar, 2001; Rao and Choudhury, 2005). Liu et al. (2017) proposed a modification to Terzaghi's method. His method led to satisfactory results for the case of granular soil and inconclusive results for the case cohesive soils.

The method by Liu et al. (2017) was utilized to predict passive pressures for cases involving a 10-m wall with soils of different densities. The predictions are shown in Figure 4.10 together with the numerically derived p-y curves for the cases under consideration. The passive pressures proposed by Liu et al. (2017) are shown as bold

lines on the right side of each figure. Results indicate that the passive pressures that are predicted using the Liu et al. (2017) model compare well with the asymptotic pressures resulting from the FE analysis. At larger depths, there is a tendency for the model to slightly overestimate the numerically derived passive pressures at large deformations. This is more visible in the cases of loose and medium-dense soil. This discrepancy in the limit-state passive pressure could be attributed to the wall movement that was adopted in our numerical model. The results published by Liu et al. (2017) were based on pure uniform lateral translation of a gravity wall in contrast to the translation/rotation movement adopted in this study for the rigid reinforced concrete wall. It should be noted that this inconsistency should not impose a challenge when proposing an empirical p-y model that is based on Equation (3). As stated previously, most design codes limit story drift to less than 2.0% making it unlikely for limit state passive pressures to fully develop behind the wall at practical depths. It could thus be concluded that the logarithmic spiral method proposed by Liu et al. (2017) is considered satisfactory for the current work and will be adopted for the prediction of passive pressures at the limit state.
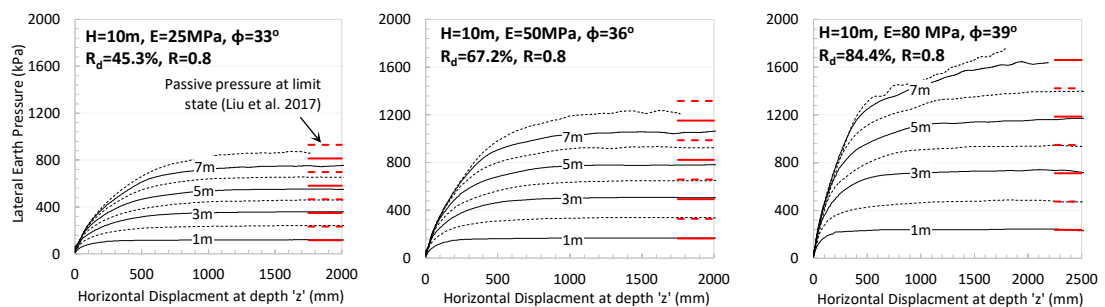


Figure 4.10 Comparison between FE analysis and limit-state passive pressure proposed by Liu et al. 2017

### 3. *Determining Initial Stiffness* ($C_o$)

The second parameter required for modeling p-y curves using the hyperbolic equation presented in Equation (3) is the initial stiffness ($C_o$). Unlike the limit-state passive pressure $p_f$, there is very limited literature on $C_o$. The determination of $C_o$ encompasses 1) extracting the values of $C_o$ from the FE results, 2) quantifying the dependence between $C_o$ and the main parameters ($z, E, H_w, \phi, \gamma$) which were found to have an impact on the numerically derived p-y response as identified in Section 4, and 3) proposing a simplified model for the prediction of $C_o$.

#### a. Extracting $C_o$ from the FE Results

Clough and Duncan (1971) presented a methodology for determining the initial stiffness of a set of data points to be fitted by a hyperbolic function. In its general form, the hyperbolic function expressed in Equation (3) can be written as:

$$p = \frac{y}{b+ay} + p_o \qquad (4)$$

By rearranging the variables, Equation (4) can be transformed into a straight line through the following expression:

$$f(y) = \frac{y}{p-p_o} = ay + b \qquad (5)$$

Where a = $1/\Delta_p$ and b = $1/C_o$. The expression in Equation (5) is that of a straight line with a slope 'a' and an intercept 'b'. Plotting the hyperbola as a straight line (Equation (5)) will allow for determining the initial slope $C_o$ as the reciprocal of the y-intercept. Figure 4.11 shows p-y curves for a 10m wall retaining medium dense soil transformed into straight lines using Equation (5). The minor curvatures in the lines are

81
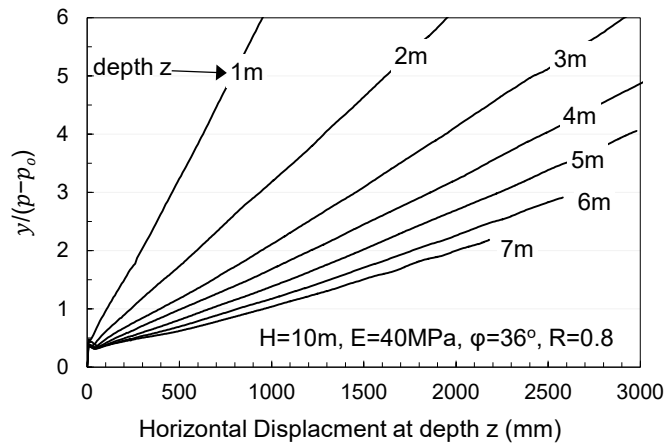
Figure 114.11 P-y curves for 10m wall retaining medium dense soil transformed into straight lines using Equation (5)

explained by the slight mismatch between the fitting model and the data extracted from FE analysis. To account for this mismatch, Clough and Duncan (1971) proposed that each line be replaced by a line passing through two points (70% and 90% of the maximum stress). This would standardize the fitting procedure and reduce any subjectivity.

b. <u>Sensitivity of $C_o$ to z, E, and $H_w$</u>

Figure 4.12 shows the variation of $C_o$ with the depth of embedment z for loose, medium dense, and dense soil. The values of $C_o$ at an incremental depth of 1m were back calculated using the method described in Section 5.3.1. Results on Figure 4.12 indicate that $C_o$ increases with embedment depth at a decreasing rate, reaching a peak value at approximately mid height of the retaining wall. After that depth, $C_o$ is observed to stabilize with very minor reductions at depths approaching the bottom of the wall. The initial increase in the values of $C_o$ with depth z is expected given the increase in the soil modulus with depth. In the hardening model, the soil modulus for granular soils

$(E_{50})$ is expressed in terms of the vertical confinement pressure $(\sigma_3)$ through the following equation:

$$E_{50} = E_{50}^{ref} \cdot \left(\frac{\sigma_3}{p^{ref}}\right)^m \tag{6}$$

Where $E_{50}^{ref}$ is the modulus of elasticity specified at a $p^{ref}$ of 101 kPa, $\sigma_3$ is the confining pressure, and the power factor 'm' defines the stress dependency on $E_{50}$. The peak that is observed in the relationship between $C_o$ and z at depths beyond $0.5H_w$ is possibly caused by the rotational movement of the wall. Alternatively, this peak could be due to a soil arching phenomenon that could lead to reduction in stresses next to the wall with depth. Further investigation on this issue is needed in future studies to better understand the reason behind this behavior.

Figure 4.13 presents the dependency of the initial stiffness $C_o$ on the wall height $H_w$ for medium dense soil retained by 5m, 10m, and 15m high walls. The effect of wall height on the initial soil stiffness is clear in the sense that soils retained by shorter walls exhibit higher initial stiffnesses than those retained by higher walls. More importantly, the peak that is observed in the value of $C_o$ around the mid-height of the wall is applicable, irrespective of the height of the wall. This observation is important since it indicates that any attempt to model the variation of $C_o$ with depth needs to incorporate the height of the wall and the increase in $C_o$ with embedment up to a peak $C_o$ value that is a function of the height of the wall.
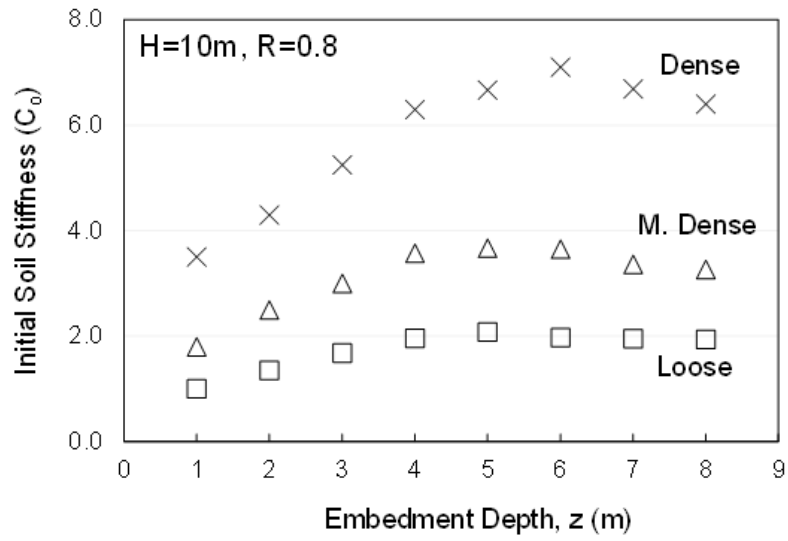
Figure 4.12 $C_o$ for a 10m wall retaining loose (E=20MPa), medium-dense (E=40MPa), and dense soil (E=70MPa)
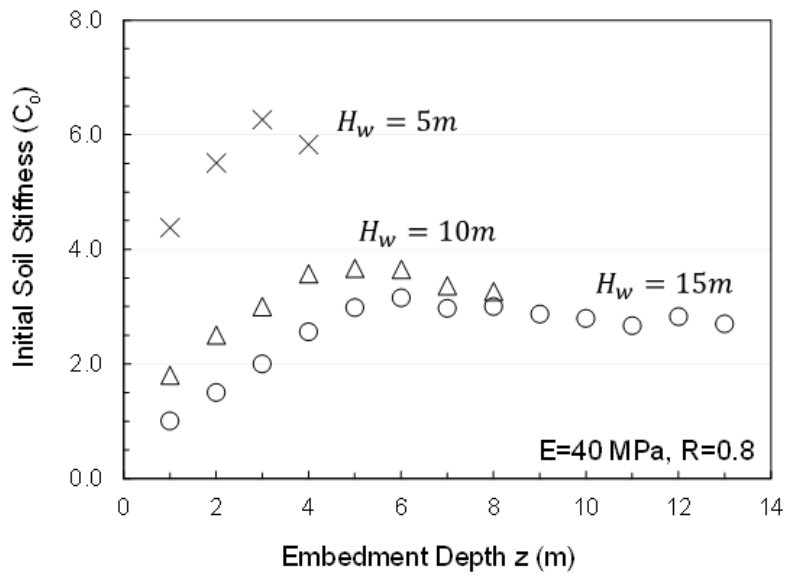


Figure 4.13 Sensitivity of $C_o$ to wall height $H_w$

c. Modeling the Initial Stiffness $C_o$

In this section, a simplified numerical expression for $C_o$ is proposed to model the variation of $C_o$ with depth for walls of different heights. The numerical expression is presented in Equation (7) and is based on a two-part model for $C_o$ as indicated in Figure 4.14. The first part consists of a non-linear curve (Equation (7)) that is applied over the upper half of the retained soil ($z$ between 0m and $0.5H_w$). The second part of the model assumes a constant value of $C_o$ determined by Equation (7) at depth $0.5H_w$.

$$C_o = E_{50}^{ref} \times \left(\frac{\gamma z}{p_{ref}}\right)^m \times \frac{1}{H_{eff}} \tag{7}$$

$H_{eff}$ is equivalent to the wall height multiplied by a correction fraction $\frac{1}{n}$, where n varies between 0.9 and 1.1 depending on the type of soil. For loose granular soil n=0.9; for medium-dense soil n=1.0, and for dense soil n=1.1. In line with the findings established in the previous section, the simplified model in Equation (7) expresses $C_o$ as a function of the modulus of elasticity, the embedment depth, and the height of the wall. The parameter $m$ is the same as that used in the soil hardening model (see Table 1).
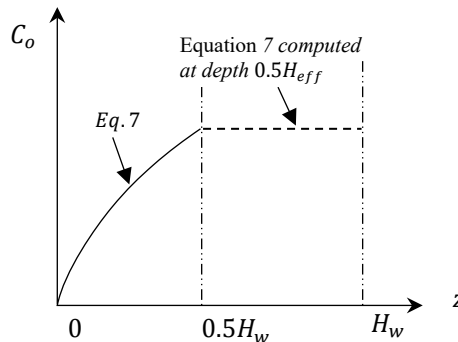


Figure 4.14 Proposed model for $C_o$
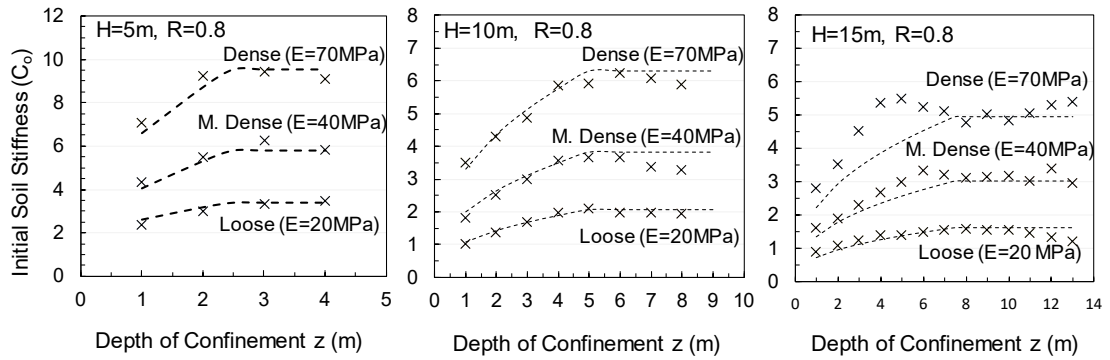
Figure 124.15 $C_o$ model (Equation (7)) versus $C_o$ extracted from FE analysis

To test the effectiveness of Equation (7) in predicting $C_o$, the FE-derived $C_o$ values and the predicted $C_o$ values (Equation (7)) were determined and plotted in Figure 4.15 for cases with different wall heights. Results on Figure 4.15 indicate that the simplified model (Equation (7)) is capable of predicting $C_o$ with an acceptable level of reliability. The only exception is the case involving a 15m high wall retaining dense soil, where the model is observed to slightly under predict $C_o$ for depths ranging from 3 to 6m. For all practical purposes, it could be concluded that the two-segment model presented in Figure 4.15 provides good predictions of the variation of $C_o$ with depth, relative density, and wall height.

### E. Validation

In this section, the effectiveness of the hyperbolic p-y model presented in Equation (3) is investigated for all representative cases analyzed in this study. In predicting the passive p-y response using Equation (3), the limit state passive pressure at any given depth is predicted using the Liu et al. (2017) model, the initial stiffness $C_o$ is modeled using the simplified model in Equation (7), and $R_f$ is assumed to be equal to 0.9.

The predicted (Equation (3)) versus numerical (PLAXIS) passive p-y curves for four representative cases involving walls with heights ranging from 5m to 15m and soils with different relative densities are presented in Figure 4.16. The analyzed cases include walls with different interface friction angles as reflected in R values ranging from 0.6 to 1.0.

It is clear from Figure 4.16 that the hyperbolic passive p-y expression that is depicted in Equation (3) is capable of modeling the p-y response of rigid basement walls that retain granular soils of different relative densities. The predictive performance portrayed in Figure 4.16 is indicative of all other cases analyzed in this study (not shown for brevity).
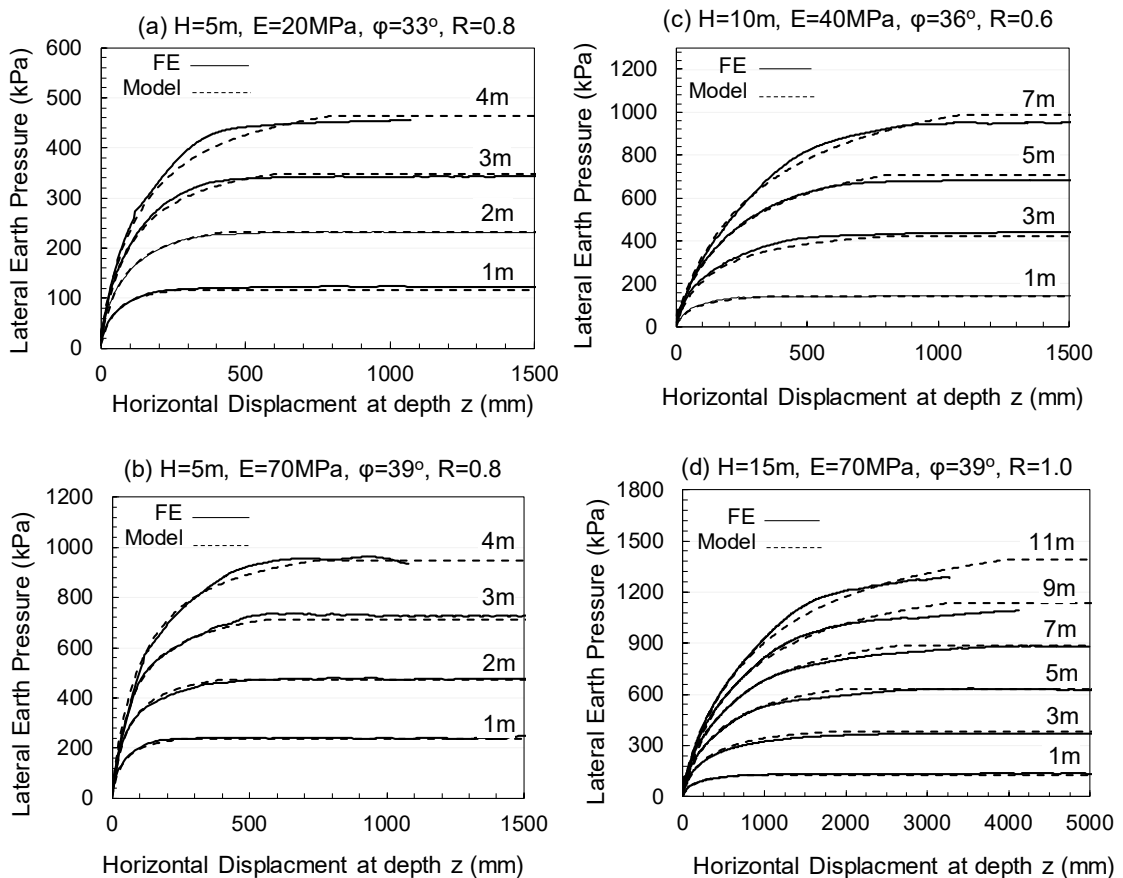


Figure 4.16 Comparison between FE analysis and proposed model

The parameters required to define the p-y relationship at different depths are limited to the limit state passive pressure as predicted by Liu et al. (2017) and the initial slope of the hyperbolic function as defined in Equation (7). The proposed simplified passive hyperbolic p-y model that is presented in Equation (3) (Ramberg-Osgood model) could be effectively employed to model the at-rest to passive segment of the p-y curves for rigid basement walls under lateral loading.

### F. Conclusions

In this study, finite element analyses were conducted to model the mobilization of passive earth pressures behind rigid basement walls. The intent is to investigate the possibility of generating p-y relationships that could be used in modeling soil response analogous to those used in pile analysis and design. Based on the results, the following conclusions can be made:

- The use of the Hardening soil model in the FE analysis resulted in p-y relationships that are realistic. The resulting p-y relationships at different depths were found to be sensitive to the relative density of the soil and the height of the wall, which had a direct effect on the magnitude of the local displacements required for passive conditions to be mobilized. Results showed that the 13mm displacement criterion that is typically referenced in the literature for the mobilization of passive conditions in p-y curves is not realistic for full scale rigid walls.
- The passive p-y response is affected by the depth below the ground surface $z$, the soil modulus $E$, the relative density, and the height of the wall $H_w$. On the

other hand, the effect of the interface reduction factor R is confined to the p-y response at larger wall displacements.

- The passive p-y response could be accurately predicted using a hyperbolic model that is based on the Ramberg-Osgood equation which requires two parameters (passive pressure at limit state and initial stiffness $C_o$) to model it mathematically. The method by Liu et al (2017) was found to be capable of predicting the numerically derived limit state passive pressures with an acceptable degree of accuracy. On the other hand, a simplified empirical model was derived to express the initial stiffness $C_o$ as a function of the depth below the surface, modified height of wall, and modulus of elasticity. The proposed hyperbolic model was shown to yield reliable predictions of the passive p-y response for all the cases analyzed in this study.

It is worth noting that the intent of this study is to provide a methodology for modeling passive p-y curves for cohesionless soils that are used as backfill behind rigid basement walls. In the finite element analyses that were conducted, the soil properties that were used pertain to those of Ottawa sand. As a result, the numerical results and the associated simplified model parameters are expected to be affected by the choice of the soil type used. Moreover, while the choice of the hardening soil model is adequate for loose and medium dense sands that do not exhibit significant post-peak softening in the stress-strain relationship, its use is questionable for dense sands that exhibit significant dilation and softening at large strains. The use of the hardening soil model for dense sands is a limitation that needs to be investigated further in future studies.

# CHAPTER 5

# EXPERIMENTAL SETUP AND SOIL

# CHARACTERIZATON

### A. Introduction

This chapter describes the experimental setup that was designed and constructed to allow for measuring the p-y response of a rigid wall supporting granular backfill. It also includes a detailed characterization of the soil material used.

A steel structure soil retaining system that can carry 2.5 tons of granular soil was designed and constructed in the lab for the purpose of measuring the p-y response of a rigid wall supporting sand of different relative densities. The retaining system was designed to be 0.5m wide, 1.2m high, and 2.6m long. As part of the system, a rigid side wall was designed to pivot about its bottom axis such that it can displace the soil in the active and passive direction in a rotational manner. Side wall friction stresses were reduced using grease and thin plastic sheets to minimize unwarranted side friction forces and to mimic as much as possible plane strain loading conditions. Pressure sensors, load cells, and LVDTs were attached to the system for collecting data that would allow for the construction of p-y curves. The method of pluviation was utilized for filling the system with backfill material. This technique is known for its ability to ensure a uniform density throughout the depth of the backfill. Three relative densities of dry sand were tested under static and slow cyclic lateral loading.

Dry clean sand was used as a backfill material. The dry sand was tested for grain size distribution, specific gravity, and minimum and maximum void ratio. Triaxial

tests were also conducted to determine the angle of friction and modulus of elasticity. Interface direct shear tests were also conducted to characterize the soil interface friction angle at the soil-wall boundary.

### B. Soil Retaining System

#### 1. *Wall System*

A steel structure soil retaining system was designed and fabricated in the laboratory. As shown in Figure 5.1, the retaining system consists of a rectangular enclosure, 0.5m wide and 1.25m high and 2.6m long, with an open top. The side walls are fabricated from $40 \times 80 \times 2.5\ mm$ rectangular hollow sections welded to a $4\ mm$ steel side plate. The side walls are braced to lateral bottom beams with side kickers at equal intervals. The bottom lateral beams are welded to the system's floor and thus constitute an integral part of the retaining wall system. The front wall is stiffened by H100x100 (I-beam) to undertake larger lateral pressures while minimizing wall deformations. It is built with a hinging mechanism at its bottom and kept unrestrained at its top. Two manual locks are installed at the top of the wall to stabilize the wall during the setup up phase. A similar design was adopted for the back wall, which was designed to flip open to facilitate access to the retaining system from the back side. The whole retaining system was designed as three separate blocks for ease of fabrication and possible relocation within the lab to be assembled with bolt systems at the side walls. The soil retaining system was modeled on SAP2000 and checked against both deflection and failure. A maximum movement of 2 mm at maximum pressure was considered as a deflection criterion.
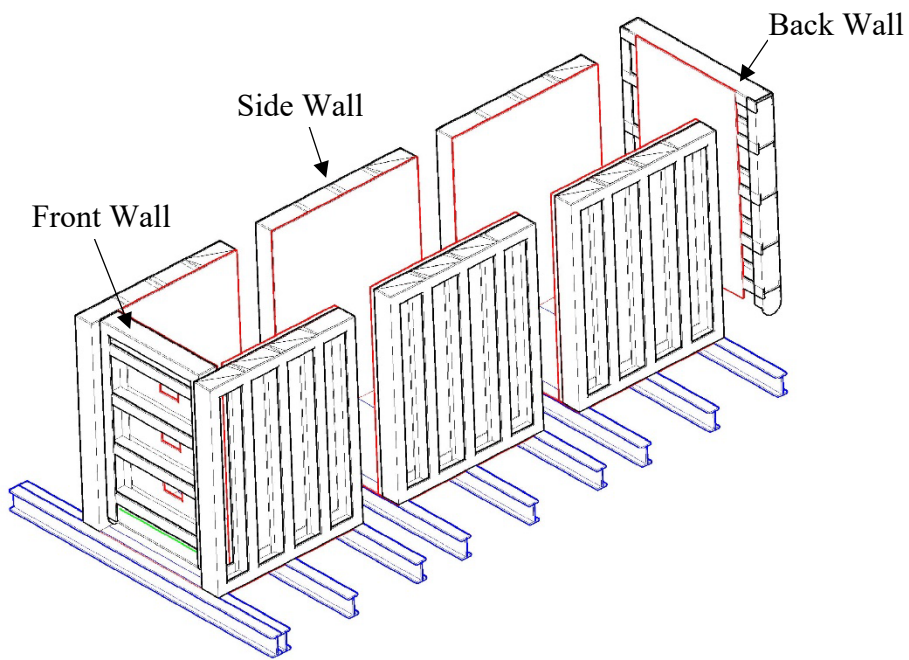
Figure 5.1 Soil Retaining System AutoCAD Drawing
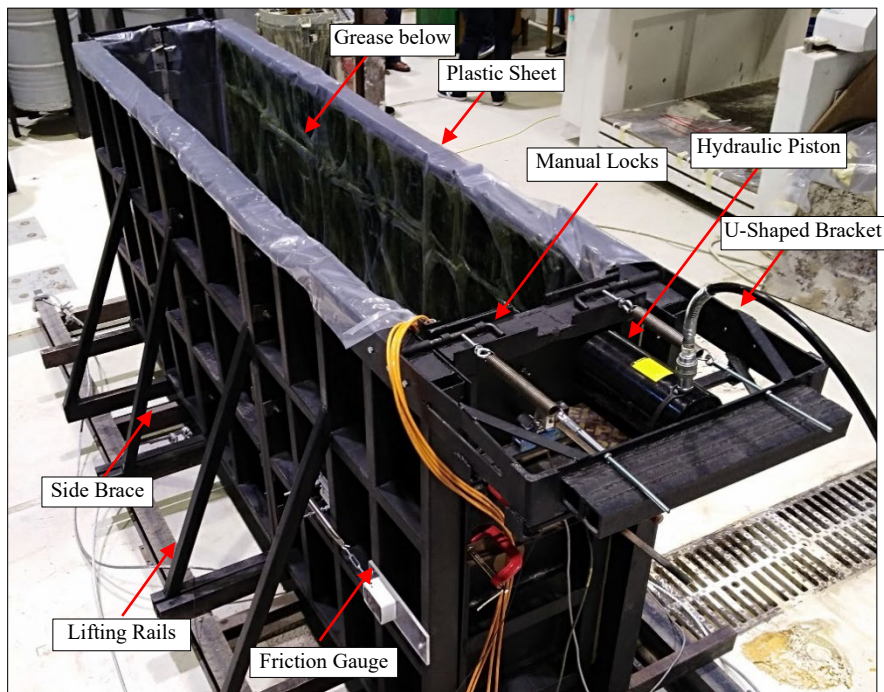


Figure 5.2 As-Built Soil Retaining System

## 2. *Front Wall Displacing Mechanism*

The soil retaining system is designed to be a stand-alone unit capable of conducting an experiment unaided by a structural unit (i.e. strong-wall) and in any location within the lab. For this to be accomplished, a U-shaped bracket attached to the side walls capable of seating a jacking system laterally (see Figure 5.2) was used. Three methods were investigated for displacing the top of the wall: (1) threaded rod method, (2) scissor jack method, and (3) hand driven hydraulic pump and piston method. In the first case, moving the wall was strenuous and required a lot of man-power and therefore was abandoned. In the case of a scissor jack, it was also strenuous and unprecise. In addition, the scissor jack buckled under the large passive pressure. As for the third case, it was relatively easy to use allowing an adequate level of displacement control. The displacing mechanism (hydraulic pump) was attached to the retaining system using a U-shaped bracket that utilized the sidewalls of the retaining system to create a self-standing system. The two springs shown in Figure 5.3 were installed to eliminate gap formation between the wall and the hydraulic piston during active wall displacement. However, after few trial experiments, it was found that the springs had to be extended significantly and were susceptible to permanent deformation. As a result, the spring system was replaced by weights extended around a pulley system and attached to the rigid wall (see Figure 5.4).

(a)　　　　　　　　　　　　　　(b)

(c)
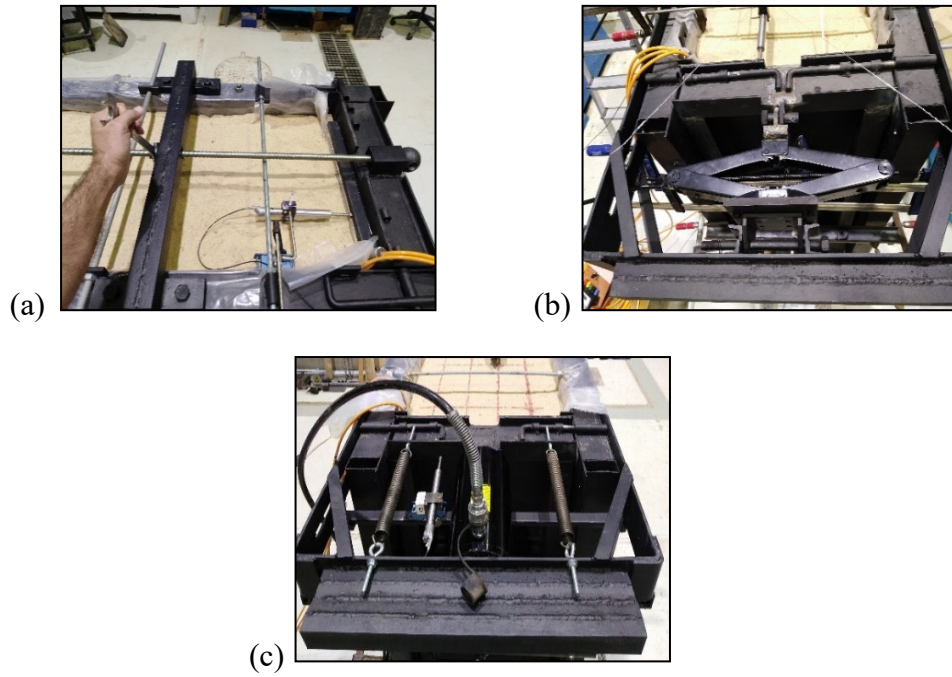
Figure 5.3 Methods for displacing top of wall using (a) threaded rod (b) scissor jack (c) hand-held hydraulic piston



Rod eye attached to rigid wall

Pulleys

Steel Wire

Weights
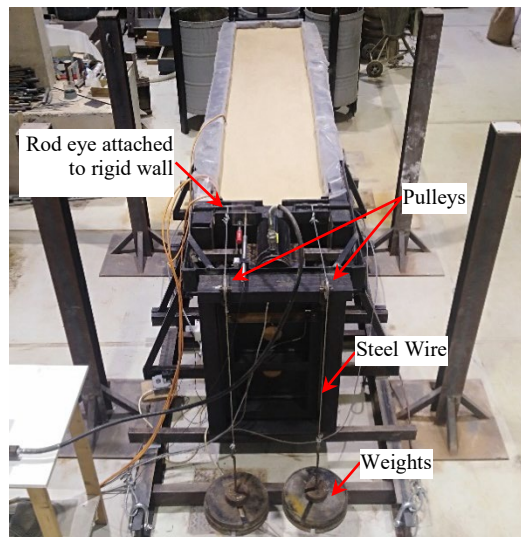
Figure 5.4 Pulley system

### 3. *Reduction of Side Wall Friction*

One of the challenges in conducting laboratory experiments on retaining wall prototypes is the development of unfavorable friction forces along the sidewalls. These friction forces can unjustifiably increase lateral earth pressures measured on the moving wall. The interface friction angle between the backfill and the side walls varies with the roughness of the interface, the particle size, and the morphology of the sand. Han (2018) reported that sand with an average particle size of $D_{50} = 2.68mm$, when sheared against a smooth steel interface, results in a $\delta/\phi$ of 0.53, where $\delta$ is the interface friction angle and $\phi$ is the internal friction angle of the sand.

Several methods that aim at minimizing the interface frictional stresses are available in the literature (Tatsuoka, 1985; Fang, 2004). The method that was adopted for its ease of application and efficacy entails creating a multi-layered interface comprising of a thin plastic sheet, grease, on thin PLEXI glass. Accordingly, a 4 mm PLEXI-glass plate was attached to the sidewalls (Figure 5.5a). A thin layer of grease was smeared over the PLEXI-glass using a paint spatula and a thin plastic sheet was overlain over the grease (Figure 5.5b & c). Though this technique was proven to greatly decrease the interface friction angle, residual frictional forces will remain. To measure these forces, a special device was custom-fabricated and attached to one of the sidewalls (Figure 5.6a). The device consisted of a low range force gauge connected in parallel with a sliding block. The block was loosely fitted in a rectangular cut made in the wall and placed flush with the interior surface (Figure 5.6b). The force gauge is mounted to the outside wall to record the frictional forces. On the opposite wall and at the same elevation, another force gauge was connected perpendicular to a fixed block in the same manner (Figure 5.6c) to measure the lateral earth pressure on the side of the wall. The

frictional shear stresses measured by the friction sensor were then divided by the normal stresses measured by the pressure sensor to calculate the friction coefficient and interface friction angle for the side wall.



(a)　　　　　　　　　　　　(b)　　　　　　　　　　　　(c)
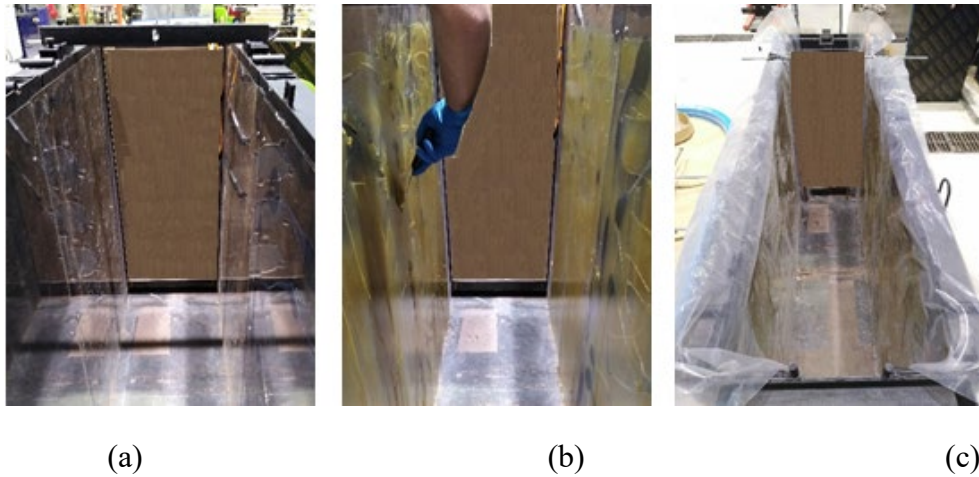
Figure 5.5 Reducing side walls friction. (a) PLEXI-glass on side walls (b) grease application over PLEXI-glass (c) thin plastic sheet above grease



(a)　　　　　　　　　　　　　　　　　(b)

(c)　　　　　　　　　　　　　　　　　(d)
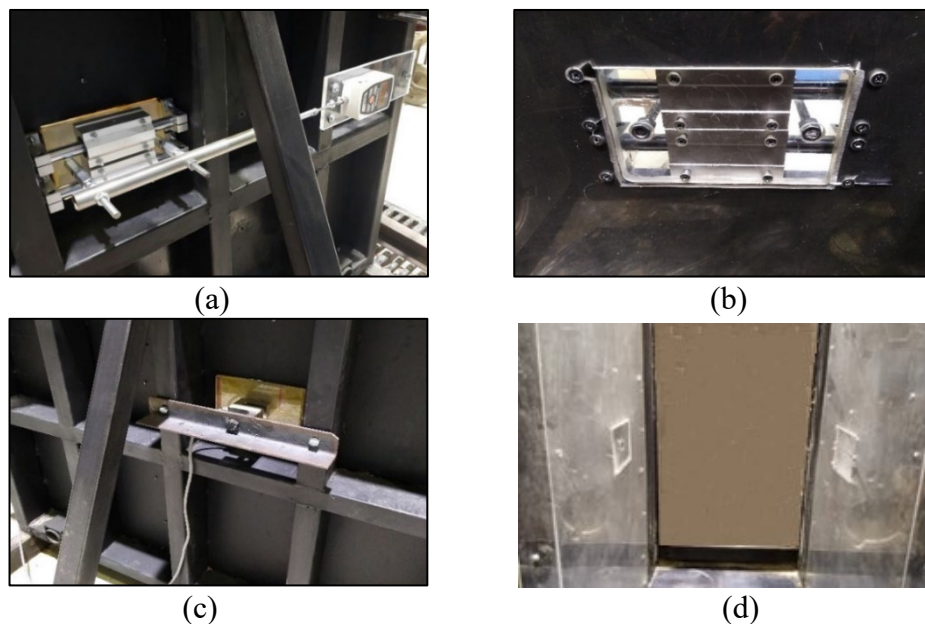
Figure 5.6 Interface friction angle device (a) parallel force gauge and sliding block (b) interior surface of sliding block flush with wall (c) perpendicular force gauge and fixed block (d) interior sidewalls showing both gauges opposite to each other.

### 4. *Pressure Sensors and LVDT's*

Three vibrating wire pressure sensors, model #4800VW by GOEKON (Figure 5.7), and two S-type load cells were used for measuring the lateral pressure induced by the retained soil under passive and active wall displacement. A schematic showing the location of the sensors on the front wall is shown on Figure 5.8. The vibration wire sensors (#2, #3, #4) have a diameter of 230 mm while the S-type load cells (#1, #5) were attached to round plates having diameters of 160 mm and 60 mm, respectively. It is recommended by the manufacturer to install the sensors flush with the inside surface of the wall. To this end, the shapes of the pressure sensors were carved out of a 40mm dense wooden board to fit the sensors flush with the wooden board (Figure 5.9a). The wooden board is then attached to the front wall (Figure 5.9b). To reduce the friction between the soil and the wooden board, a PLEXI-glass plate was added onto the surface of the board. In addition, an extra pressure sensor was placed at the floor of the retaining system to measure changes in vertical pressure while filling the tank and during the experiments (Figure 5.9b). In addition to the pressure sensors, two LVDT's, shown in Figure 5.8c, were placed on the front wall to measure the displacement at the top and mid height of the wall. The rigidity of the wall can be confirmed by looking at the ratio of one LVDT to the other.
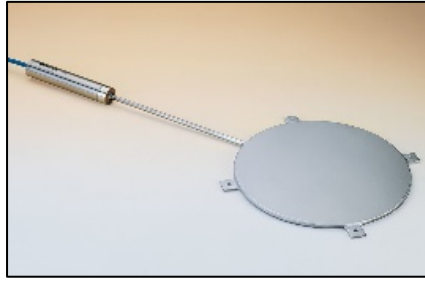
Figure 5.7 VW pressure sensor by GEOKON
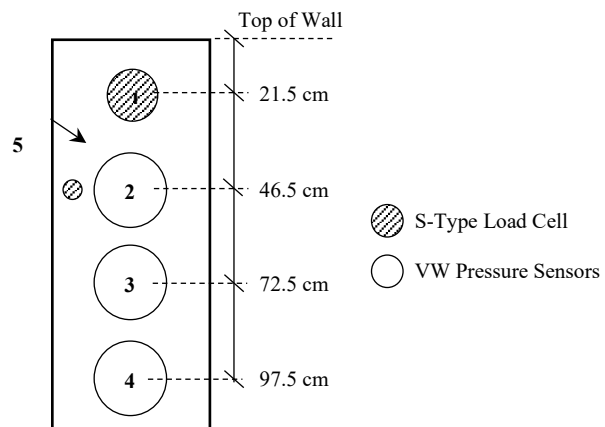


Figure 5.8 Sensor's location from top of wall
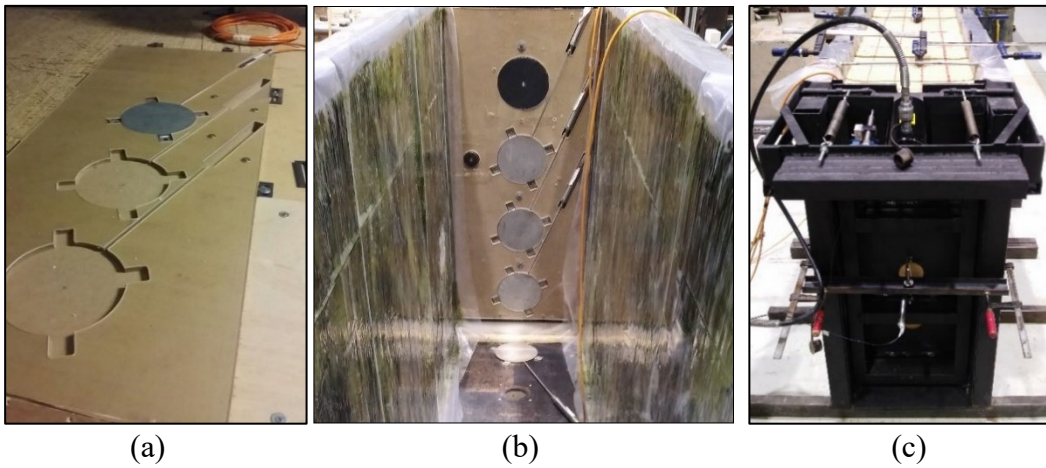


Figure 5.9 (a) Wooden board carved to fit sensors (b) pressure sensors on front wall
(c) LVDTs at top and middle of front wall

### 5. *Filling and Emptying Tank*

Since density is a key variable in the development of lateral earth pressure, sand should be placed in successive layers at a constant density. A well-documented method known as pluviation aims at providing a constant density for large scale laboratory experiments (Dave, 2012; Gade, 2016; Tabaroei, 2017). The pluviation technique utilizes the raining down of sand from a height (HF) at a constant discharge rate, deposition intensity (DI), to reach a pre-set density. Several pluviators of different complexities have been proposed in the literature. Figure 5.10a shows a portable pluviator designed by Dave et al. Common components of pluviators are: a sand storage compartment, a transporting flexible tube, an orifice that discharges sand at a specific rate, a rigid tube of different height to control the height of fall, and finally a sieve diffuser (Figure 5.10b) at the end of the rigid tube whose purpose is to rain sand in a uniform manner over a certain area.



(a)                                                    (b)
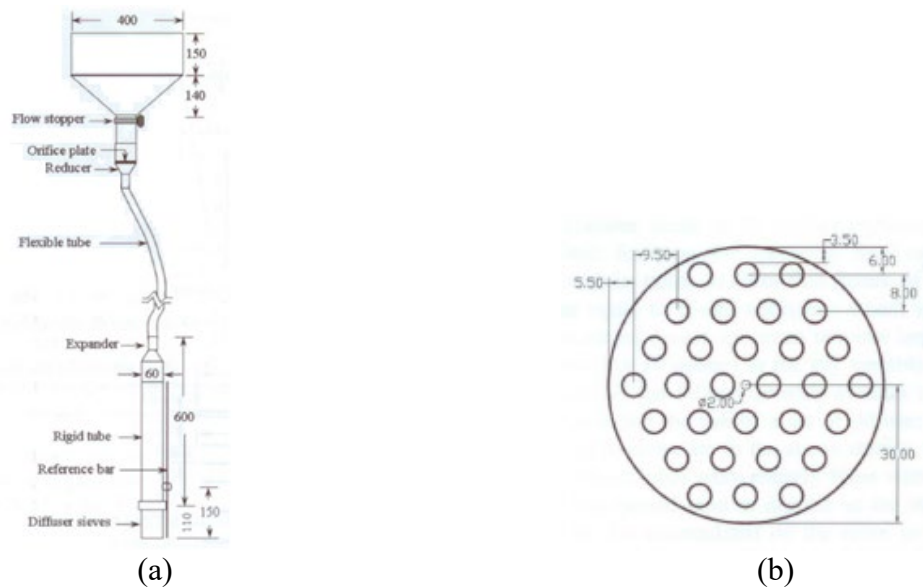
Figure 5.10 Portable traveling pluviator as designed by Dave et al. (a) pluviator device (b) sieve diffusor

A similar pluviator was crafted for the present study (Figure 5.11a). The hand-held portable pluviator is designed to be carried and moved by the laboratory crane and adjusted by hand. A steel barrel was used as a sand storage unit. A hole at the bottom of the barrel was cut out for sand to escape. At the hole location, a butterfly shutter is connected to open and close the hole. The butterfly shutter is attached to a flexible tube to transfer the sand from the sand storage unit to the rigid tube were the sand is discharged. An orifice is placed at the top end of the tube (Figure 5.11b) to control the rate of sand discharge. Since the pluviator is designed to be hand-held and manually operated, the flexible tube is customarily tugged in different directions during the filling process creating an inclination in the rigid tube. This inclination will pull the sand to one edge of the rigid tube and change the rate of discharge of sand and the resulting density. To ensure a vertical position of the rigid tube, a leveling mechanism was fabricated and placed between the flexible and the rigid tube (Figure 5.11c). The leveling mechanism consists of four PVC reducers with each two consecutive reducers joined by a 6mm rod. The rod serves as a pivoting axis allowing one reducer to twist (in the direction of the rod) while the second maintains its vertical position (Figure 5.12). If only two reducers and one axis of rotation are present, then shifting the flexible tube along a line that is perpendicular to the axis of rotation will keep the rigid tube vertical. Movement in any other direction will twist the bottom reducer as well. Having four reducers joined with rods at 45 deg from each other will give the freedom for shifting the flexible tube in four direction while maintaining the last reducer vertical. More reducers and more axes of rotation will produce better results, but for all practical purposes four is found sufficient.
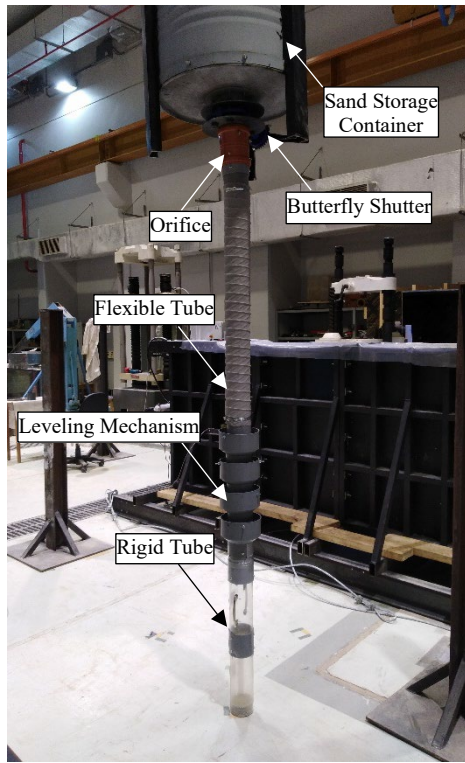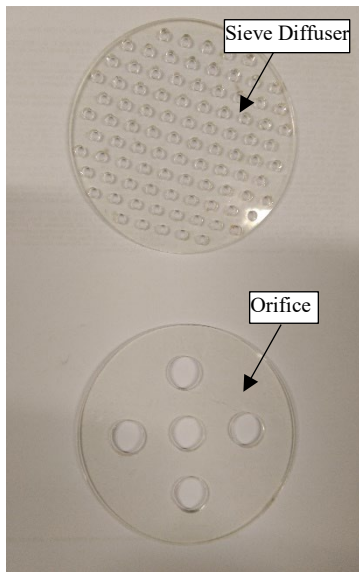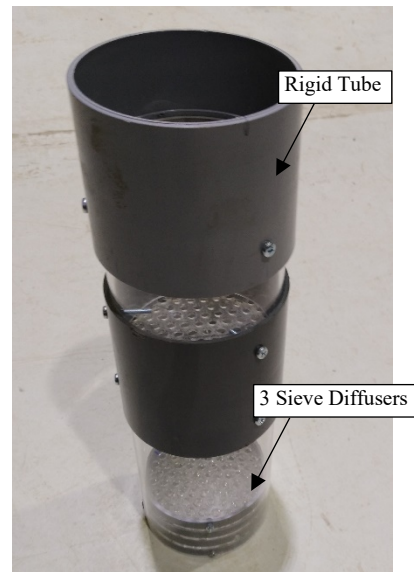
Figure 5.11 (a) Portable pluviator (b) sieve diffuser and orifice (c) leveling mechanism and (d) rigid transparent tube
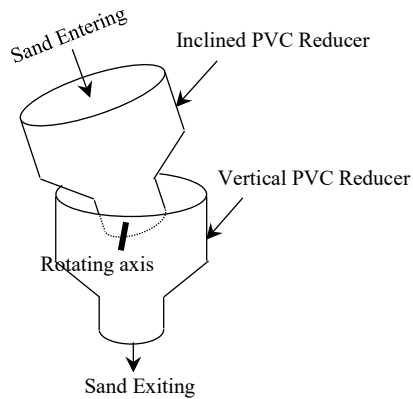
Figure 5.12 PVC reducer joined to form the leveling mechanism

The height of the sand drop and the size of the orifice needed to produce a specific density is determined by trial and error. Several pluviation tests were performed on a round mold, of known volume, using the hand-held pluviator described above (Figure 5.13a). Three sizes of orifice openings were evaluated: 5 opening – 6 mm in diameter, 5 opening – 10 mm diameter, and 5 opening – 15 mm diameter. For each size of orifice, the height of fall was varied and the density of the resulting sample was calculated. The results of the pluviation tests were plotted on a graph as shown in Figure 5.13b. With the aid of the graph shown on Figure 5.13b, the height of fall and the size of the orifice are selected based on the target density. For the given program, three densities will be used: 1550 $kg/m^3$, 1650 $kg/m^3$, and 1750 $kg/m^3$. Figure 5.15 shows the process of pluviation used to fill the soil retaining system. It should be noted that the density of the soil placed in the retaining system through pluviation is then validated twice. The first check is performed by keeping record of the weight of the total soil placed into the system and dividing it by the volume. The second check is performed by determining the density of a small container kept on the retaining system floor after emptying the system.

The retaining system carries approximately 2.5 tons of sand at a density of 1700 kg/m³. Emptying a retaining system of this scale repeatedly is an arduous and time-consuming task. In order to empty the soil, three holes are cut out of the floor of the retaining system and fitted with three gate valves. The whole system is placed on a steel platform. Once the experiment is completed, the steel structure with the soil retained are raised through cables connecting the steel platform to the crane and placed on four steel pedestals (Figure 5.14). Storage containers are slid underneath the steel platform to accept the soil that is emptied.



(a)                                                        (b)
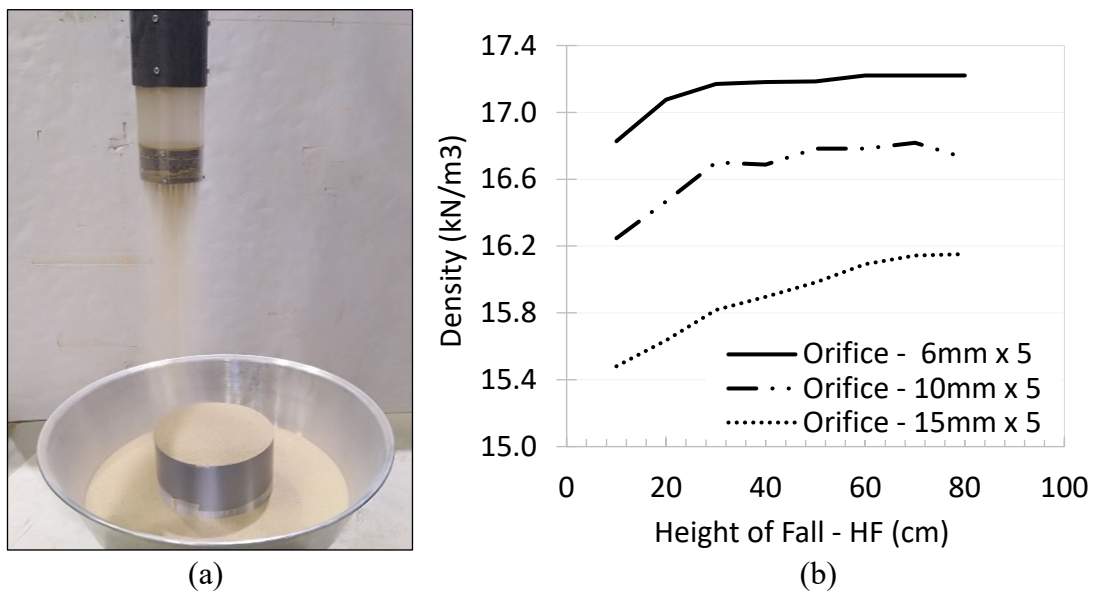
Figure 5.13 (a) Pluviation experiment conducted on small mold (b) Results of pluviation experiments
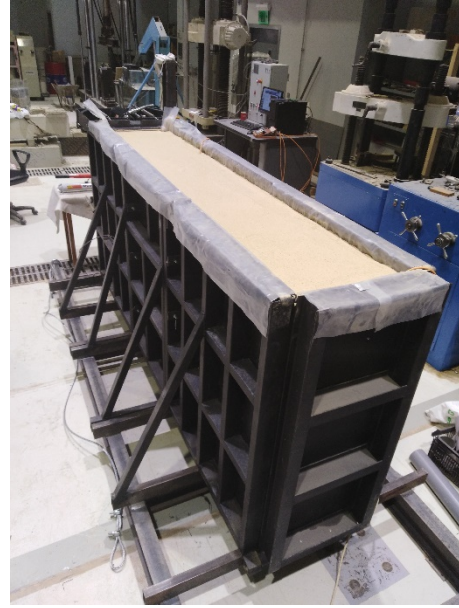
Figure 5.14 Filling the soil retaining system with sand using pluviation



Figure 5.15 Emptying retaining system in storage barrels

## C. Soil Characterization

### 1. *Index Property*

To characterize the index properties of the backfill sand, three types of tests were conducted: sieve analysis tests according to ASTM D-6913, specific gravity test according to ASTM D854, and finally maximum and minimum dry density tests according to ASTM D4253 and ASTM D4254, respectively. A typical grain size distribution for the backfill material resulting from a sieve analysis test is shown on Figure 5.16. The grain size distribution curve indicates that the soil sample is composed of 0% gravel, 99.5% sand, and 0.5% fines. The coefficient of curvature $C_c$ $(= \frac{(D_{30})^2}{D_{60}D_{10}})$ and the coefficient of uniformity $C_u$ $(= \frac{D_{60}}{D_{10}})$ were calculated to be 1.2 and 0.68, respectively. According to the United Soil Classification System, this soil is classified as poorly graded clean sand with little or no fines, SP. The average specific gravity from three tests was calculated as 2.64. The minimum and maximum void ratios for the sand were found to be 0.47 and 0.81, respectively.
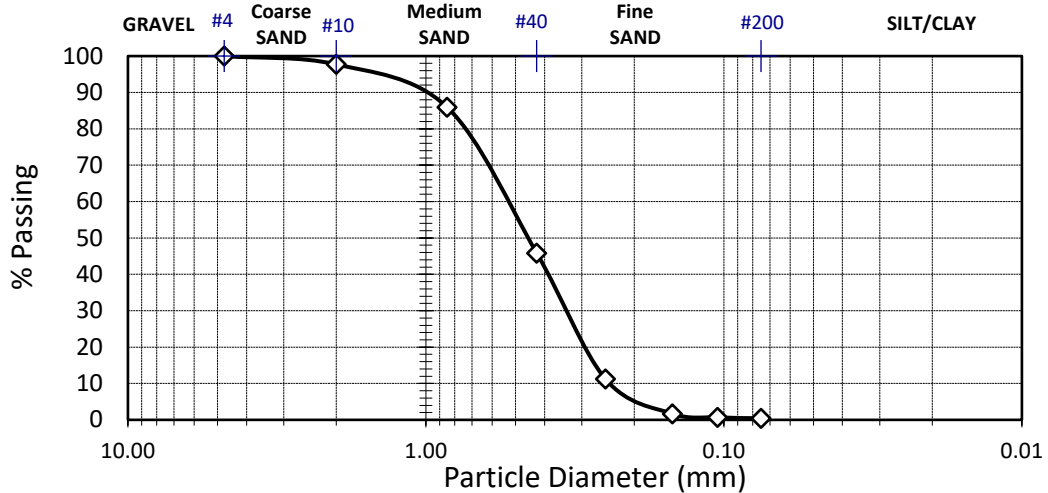


Figure 5.16 Grain size distribute for the backfill material

## 2. *Shear Strength Characterization*

The Mohr-Coulomb envelope that characterizes the shear strength of granular soils is typically approximated as a straight line in the typical pressure range expected in field applications involving retaining systems. However, given that the experimental setup that was used in this testing program involves a relatively small wall (1.2m height), the expected initial confining stresses in the sand bed are in a lower pressure range (5 to 20 kPa). While Mohr-Coulomb failure envelopes are commonly approximated by a straight line over the range of conventional confining pressures, experimental evidence shows that extrapolating a linear envelope over the range of low confining pressures may not be realistic given the curved nature of the envelope at very low confining pressure.

For illustration, Figure 5.17 shows a Mohr-Coulomb failure envelope for Compacted London Clay derived experimentally at low confining pressures. The solid line is an enhanced non-linear prediction of the failure envelope calibrated by two experimentally derived stress points at 5 kPa and 25 kPa confining pressures. The nonlinearity in the real failure envelope and the overprediction in Mohr-Coulomb failure envelope at low confining pressure is clearly shown in the figure.

The depth of the backfill material used in the retaining system constructed in the lab is 1.2 m. This suggests that if a realistic soil friction angle is to be determined, it is best computed for low confining pressures. The friction angle of soils is commonly obtained using two types of experiments: Direct Shear Test and Triaxial Test. The Direct Shear test is most popular and relatively easy to conduct. However, the mechanical friction that develops in the shearing box and the test setup of the Direct
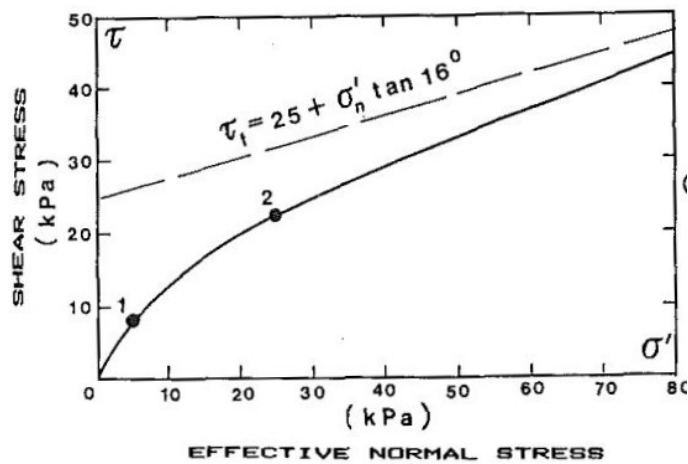
Figure 5.17 Failure Envelope for Compacted Clay Presented by Milan Maksimovic

Shear Test leads to significant errors in the inferred shear at low confining pressure. Triaxial tests, on the other hand, though more complicated, tend to be more suitable for the low confining pressures.

To characterize the shear strength of the sand,  the friction angle will be obtained for both large and low confining pressures. Direct shear tests will be utilized for determining the soil friction angle at large confining pressures while Triaxial tests will be utilized for determining the soil friction angle at low confining pressure. The procedure used in both experiments will be presented below.

a. Direct Shear Test

The direct shear machine used for determining the soil friction angle at large confining pressures was fabricated by ELE international (Figure 5.18). The machine is utilizes an S-type 5 kN load cell to measure the resisting shear load in the specimen, an LVDT for measuring the lateral movement in the shearing box, and a micro-processor

control drive unit capable of shearing the soil sample at speeds ranging between 0.00001mm/min and 9.9999 mm/min. The shear box accepts a 60x60x25mm specimen.

For the retaining wall experiment, 10 mm thick dry specimens having densities of 15.2 kN/m$^3$, 16.2 kN/m$^3$, and 17.2 kN/m$^3$ were prepared for direct shear testing. By controlling the mass and the thickness of each specimen, the correct density can be ensured. The specimens were sheared at normal stresses of 30 kPa, 80 kPa, and 130 kPa. The shear stress at every incremental displacement was determined by dividing the shear force by the corrected sheared area updated at every horizontal movement of the shear box. Each test was repeated three time and the mean value of the maximum shear stress is calculated and presented in Table 5.1. The angle of friction for each soil density is then calculated by plotting the maximum shear stress for each confining pressure against the confining pressure and back calculating the slope of the joining line as shown in Figure 5.19. The friction angles for the soil sample with densities of 15.2 kN/m$^3$, 16.2 kN/m$^3$, and 17.2 kN/m$^3$ is 34.9 deg, 36.5 deg, and 37.8 deg, respectively. The reported friction angles describe the Mohr-Coulomb envelopes presented in Figure 5.19 over a stress range of 30 kPa to 130 kPa, assuming no cohesion.

Figure 5.18 ELE Direct Shear Machine

Table 5.1 Maximum shear stress of different densities of granular soils sheared under large normal stresses.

| Confinement Pressure (kPa) | Density (kN/m³) | | |
|---|---|---|---|
| | 15.5 | 16.2 | 17.2 |
| | Maximum Shear Stress, $\tau_{max}$ (kPa) | | |
| 30 | 23.5 | 24.5 | 32.4 |
| 80 | 58.3 | 60.6 | 74.8 |
| 130 | 93.2 | 98.6 | 110.0 |
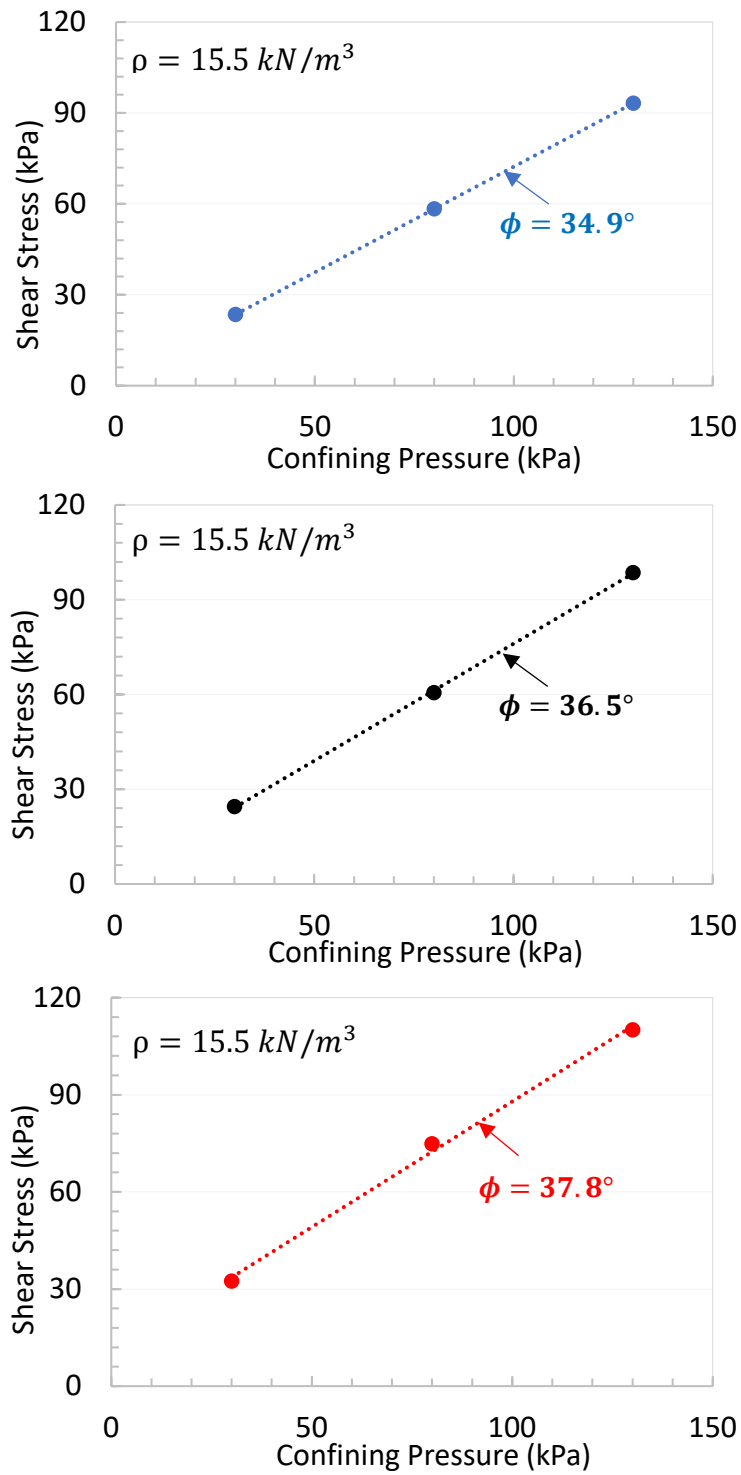
Figure 5.19 Angles of friction for different densities of the granular soil sheared under large confining pressures

b. <u>Triaxial Test</u>

A Humbolt triaxial testing system was used for determining the angle of friction of the granular soil at low confining pressure. The system consists of an automated loading frame and a flexpanel pressure control unit that utilizes a system of burettes for controlling compressed air, water, deaired water and vacuum. Consolidated Drained triaxial tests were conducted on dry sand specimens under confining pressures of 10 kPa, 20 kPa, and 50 kPa. Similar to the direct shear tests, the soil specimens were prepared at three densities: 15.2 KPa, 16.2 KPa, and 17.2 KPa.

i.  <u>Procedure</u>

The steps used for preparing the sample and conducting the test are presented below.

1. A cylindrical latex membrane is fitted over the pedestal base of the cell and secured with a rubber O-ring at its bottom end. Meanwhile, the four no-volume-change valves (two values to handle top sample drainage, two values to handle bottom sample drainage) are kept closed shut. The two tubes connecting the two values to the top cap are kept loose.

2. The 2-Part Split Miter Box (joined at this stage) is placed over the latex membrane and pushed against the bottom of the cell. Any excess membrane at the bottom is folded over and around the Miter Box. A filter paper strip is placed between the latex membrane and the Miter Box behind the vacuum nozzle opening. The filter paper restrains the latex membrane from clogging the nozzle when vacuum is drawn. Another O-ring is placed around the top Miter Box. The O-ringe will be slid around the top cap in later steps.

Figure 5.20 Latex membrane fitted over pedestal base



Figure 5.21 Split mold fitted around latex membrane
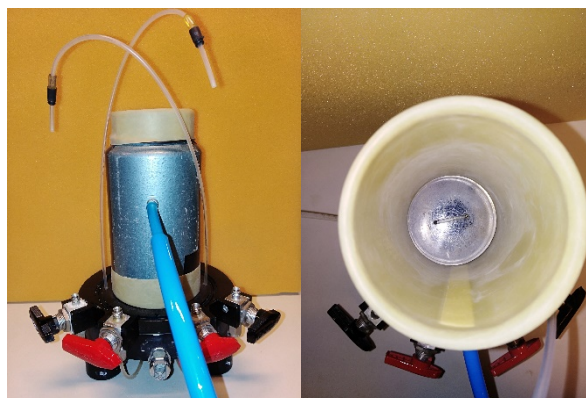


Figure 5.22 Vacuum drawn between membrane and split mold

3. The top latex membrane is folded around the Miter Box and vacuum is drawn from the nozzle. The difference in pressure between both sides of the membrane pulls the membrane back against the inner wall of the Split Box. This step is necessary to ensure that the volume to be filled by the soil sample is both controlled and measurable.

4. Before the soil is poured inside the Split Box, a porous stone overlain by a circular filter paper is set over the base pedestal. The mass of the sample is back-calculated from the chosen density and the inside volume of the Split Box. To create a uniform sample, the sample is built in three successive layers. For each soil layer, the associated soil mass is poured into the Split Box and the soil is compacted to the relevant height. This is repeated three times until the full sample height is attained.

5. Once the full height of the sample is reached, a filter paper, followed by a porous stone, and a top cap is placed over the sample. The latex membrane is then pulled over the top cap and the rubber O-ring is slid from the Split Box onto the top cap.

6. At this stage the sample is still contained within the Split Box. Removing the Split Box will lead to the collapsing of the soil sample. The soil sample is commonly held together by pulling a small amount of vacuum from the inside of the sample. This is done by first plugging the two tubes connecting the bottom valves into the top cap creating a closed system. Two valves, one handling the drainage to the pedestal base and another handling the drainage to the top cap, are connected to a vacuum pressure chamber. The valves are opened and vacuum pressure is released from the pressure chamber into the soil sample.
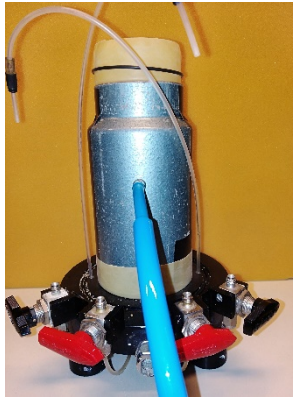
Figure 5.23 Vacuum pulled between the split mold and the latex membrane



Figure 5.24 Dry sand weighed for the sampling of triaxial test



Figure 5.25 Vacuum drawn from within the sample

It is vital that the amount of vacuum pressure pulled from inside of the sample does not exceed the confinement pressure chosen for the shearing of the sample. Once the specimen is checked for pressure leakage (drop in vacuum pressure), the valves are shut close and the split box removed. The sample should now retained its cylindrical shape.

7. The sample's diameter and length are measure and the density calculated and checked against the target density.

8. The cell chamber is reassembled and filled with water. Bleeding of the chamber is performed that all trapped air pockets escapes. The cell is placed in the Humbolt load master and sheared at a rate of 1.0 mm/min.

Figure 5.26 Soil sample with negative internal pressure
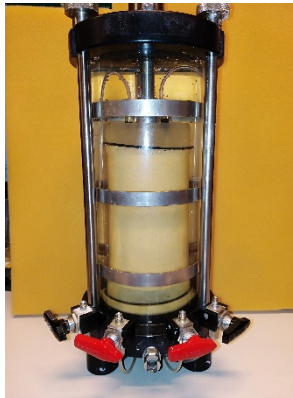


Figure 5.27 Soil sample placed in cell chamber and filled with water
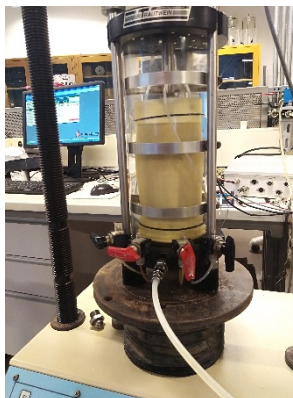


Figure 5.28 Soil sample sheared in Triaxial machine

ii.    Results

The triaxial test results for soil densities of $15.20 \, kN/m^3$ (loose), $16.20 \, kN/m^3$ (medium-dense), and $16.8 \, kN/m^3$(dense) are presented in Figures 5.28, 5.29, and 5.30, respectively. Figure 5.29 shows the deviatoric stress-axial stain graphs, Figure 5.30 shows the volumetric strain-axial strain graphs, and Figure 5.31 shows the secant friction angle-confining pressure graphs. The deviatoric stress-axial strain diagram provides insight on the stress-strain response leading to failure. The maximum shear stress at failure is defined as half of the deviatoric stress. The increase in confinement pressure and soil density is accompanied with an increase in shear stresses at failure as indicated by Figures 5.29. Shearing tests performed on sand with the densities of $16.20 \, kN/m^3$ and $16.80 \, kN/m^3$ under the confinement pressures of $10kPa$, $20 \, kPa$ and $50 \, kPa$ reveal a softening of shear stresses at large axial strain. This behavior is a characteristic of dense sand.

The volumetric strain-axial strain graphs shown in Figure 5.30 complement the results seen in the Figure 5.29. The volumetric strain in Figure 5.30a indicates a large decrease in the volume of the specimen followed by an increase under large axial strain. On the contrary, Figures 5.30b & c indicate a different behavior whereby the specimen undergoes a slight decrease in the specimen volume over a short portion of the total axial strain followed by an increase in the specimen volume. Both behaviors are consistent with behaviors observed in loose and dense sand, respectively. Finally, the secant friction angle of each soil density is plotted on Figure 5.31. As would be expected, soils with higher densities and under lower confinement pressures result in higher secant stiffness angles.
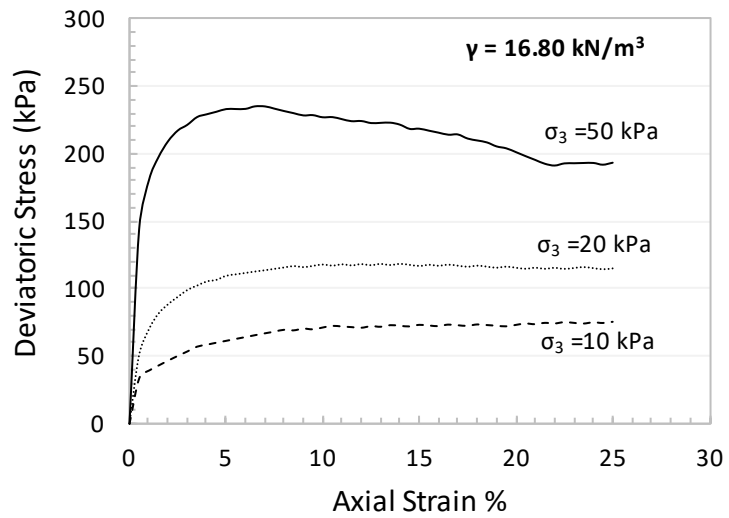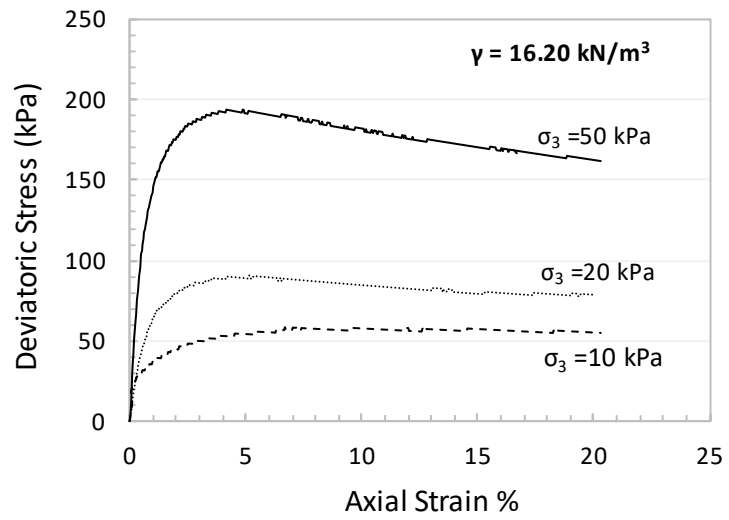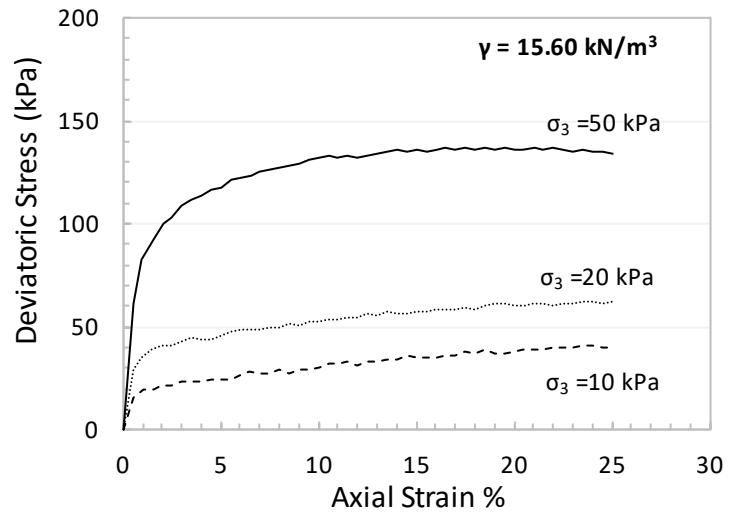
Figure 5.29 Deviatoric Stress-Axial Strain Graphs
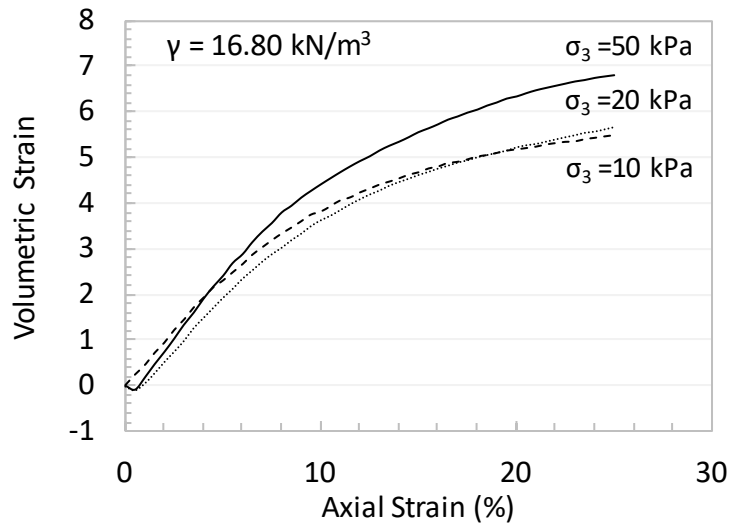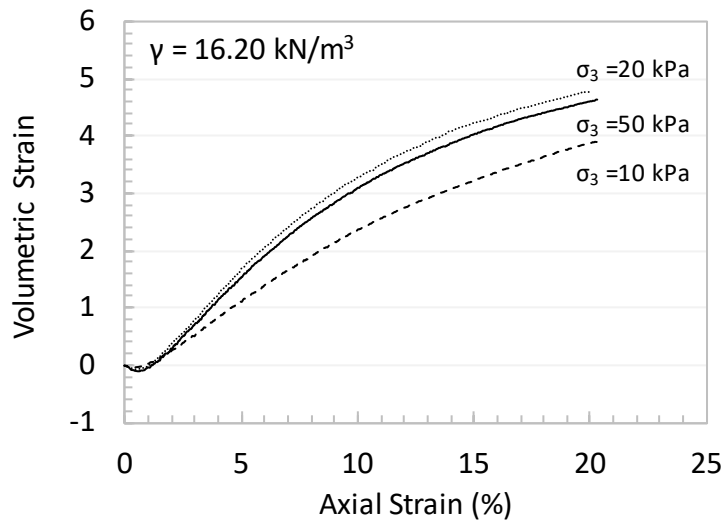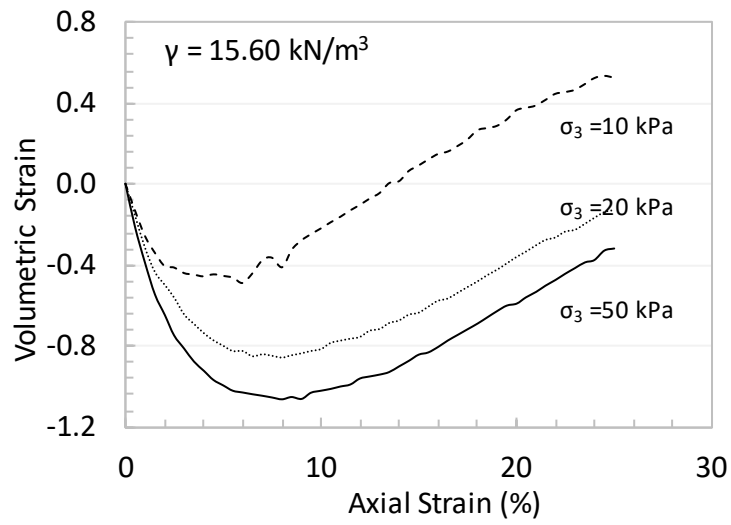
Figure 5.30 Volumetric Strain
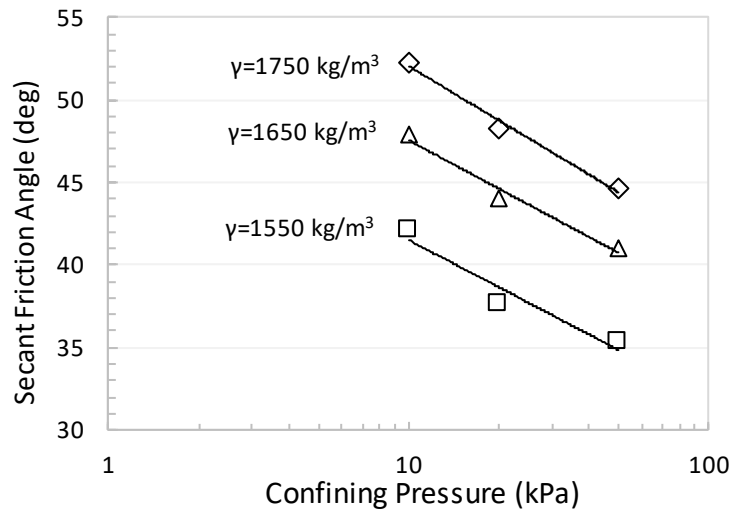
Figure 5.31 Secant friction angle for loose, medium-dense, and dense sand

## D. Calibration of Triaxial Test on PLAXIS 2D

PLAXIS 2D offers a way for simulating soil lab tests (direct shear tests, triaxial test and oedometer tests) numerically using a built-in algorithm called SoilTest. SoilTest can be used in conjunction with experimental results to calibrate complex soil models to predict the behavior of the tested soil. This exercise was implemented on the triaxial test results presented in the previous section. Table 5.2 presents the soil hardening model parameters used to best fit the triaxial test results shown in Figures 5.29 and 5.30. The simulated soil behavior given by SoilTest are superimposed over the triaxial test results in Figure 5.32 and given by the black dashed line. Simulated constitutive relationships provide an excellent prediction of the soil behavior. It should be noted that the soil hardening model is incapable of capturing soil softening behavior of dense soil as observed in Figure 5.32 (b & c) for a confinement pressure of 50 kPa.
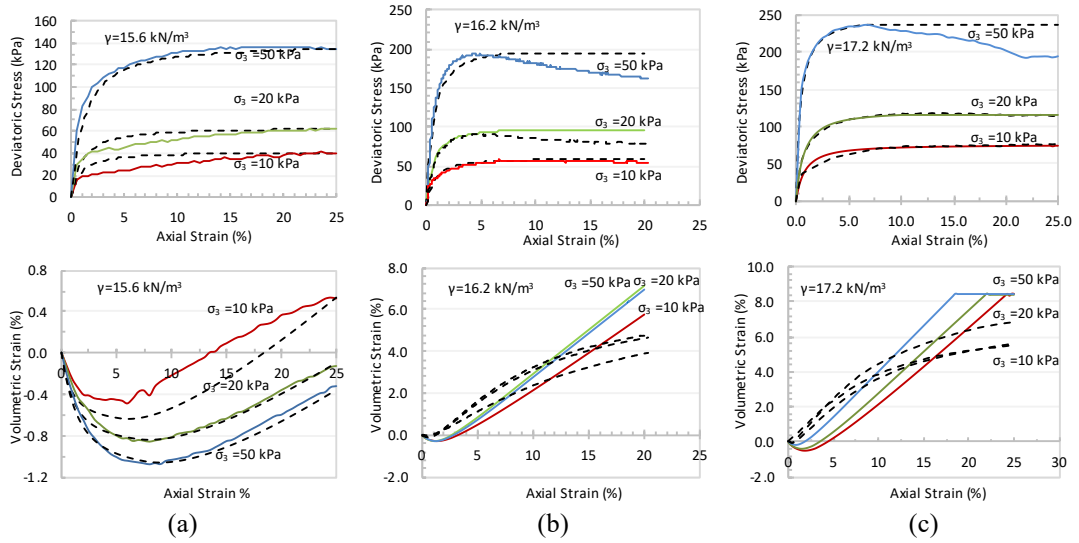
Figure 5.32 Soil hardening model predicting triaxial test results for a) loose soil b) medium-dense soil c) dense soil

Table 5.2 Calibration of soil hardening model parameters to match triaxial test results

| | DENSITY | | | | | | | | |
|---|---|---|---|---|---|---|---|---|---|
| | **15.2** | | | **16.2** | | | **17.2** | | |
| $\sigma_3$ (kPa) | 10 | 20 | 50 | 10 | 20 | 50 | 10 | 20 | 50 |
| E50$_{ref}$ (kPa) | 5000 | 6000 | 8000 | 12000 | 18000 | 25000 | 12500 | 17000 | 40000 |
| Eoed$_{ref}$ (kPa) | 5000 | 6000 | 8000 | 11700 | 18000 | 25000 | 10000 | 16000 | 40000 |
| Eur$_{ref}$ (kPa) | 200000 | 200000 | 200000 | 200000 | 200000 | 200000 | 200000 | 200000 | 200000 |
| m | 0.4 | 0.4 | 0.4 | 0.4 | 0.4 | 0.4 | 0.4 | 0.4 | 0.4 |
| v | 0.3 | 0.3 | 0.3 | 0.3 | 0.3 | 0.3 | 0.3 | 0.3 | 0.3 |
| $k_o$ | Auto | Auto | Auto | Auto | Auto | Auto | Auto | Auto | Auto |
| $p_{ref}$ (kPa) | 100 | 100 | 100 | 100 | 100 | 100 | 100 | 100 | 100 |
| c | 0 | 0 | 0 | 0 | 0 | 0 | 0 | 0 | 0 |
| $\phi$ (deg) | 42.1 | 37.6 | 35.3 | 47 | 44 | 41 | 52 | 48 | 44.6 |
| $\psi$ (deg) | 3 | 10 | 11 | 2.2 | 10 | 11 | 2.2 | 10 | 11 |
| $R_f$ | 0.98 | 0.98 | 0.98 | 0.95 | 0.95 | 0.95 | 0.98 | 0.95 | 0.95 |
| $\gamma$ (kN/m$^3$) | 15.2 | 15.2 | 15.2 | 16.2 | 16.2 | 16.2 | 17.2 | 17.2 | 17.2 |

121

**E. Interface Friction Angle**

The interface friction angle has a significant impact on the lateral earth pressure mobilized at the front wall of the soil retaining system. In the case of theconstructed soil retaining system, the backfill soil will shear against a 4mm acrylic plate mounted on the front wall. The acrylic plate was used on the front wall in order to reduce soil friction. It is imperative, therefore, to quantify the interface friction angle of sand against acrylic material.

The determination of the interface friction angle of sand on acrylic surface was done using the direct shear machine. Three sample densities of $1550 \ kg/m^3$, $1650 \ kg/m^3$, and $1750 \ kg/m^3$ were considered. An acrylic plate was fitted tightly in the lower shear box as shown in Figure 5.33. The Mohr-Coulomb failure envelopes that were fitted to the interface direct shear data for the three relative densities are presented in Figure 5.34. Results indicate that the interface friction angle between the sand and the acrylic ranged from 9.8 to 13.9 degrees, with the lower friction angles being consistent with the smallest relative density and the higher friction angle being consistent with the highest relative density used.
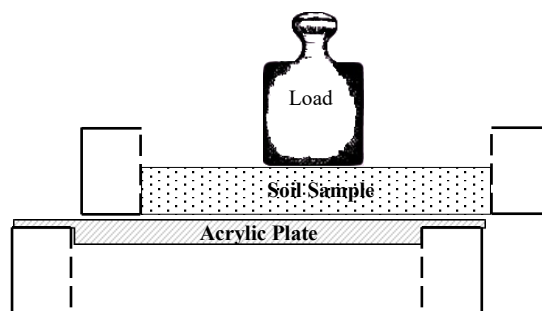
Figure 5.33 Shear box setup for sand-acrylic interface friction angle

122
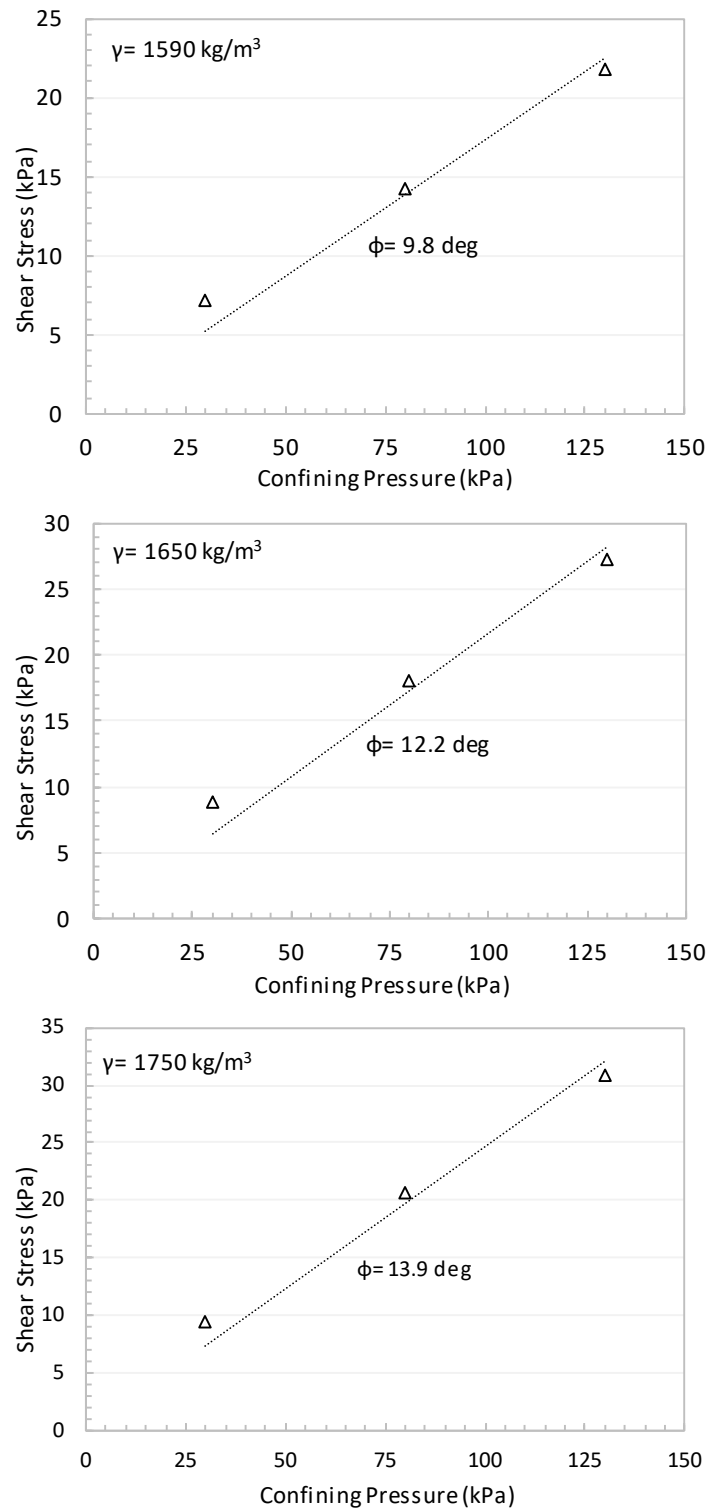
Figure 5.34 Results for angle of friction at interface between sand and acrylic plate

# CHAPTER 6

# EXPERIMENTALLY DERIVED P-Y CURVES UNDER STATIC PASSIVE AND ACTIVE LOADING

## A. Introduction

In this chapter, sand beds with three different relative densities will be used to quantify the effect of relative density on the static p-y response of the wall. The tests will involves full static cycles of loading, with each cycle initiating by displacing the wall from its at-rest condition to an active condition, followed by passive loading up to a maximum wall displacement of 10% of the height of the wall (around 120 mm). Two additional cycles which involve unloading the wall from passive to active and from active to passive are then enforced. The goal of these cycles is to quantify the changes that will occur to the p-y response if the wall is subjected to extreme displacements.

## B. Experimental Setup

Prior to conducting each experiment, the retaining system had to be carefully prepared. Beginning with an empty system, gravity loads are first connected to the rigid wall through a pulley system and hung in front of the rigid wall as shown in Figure 5.4. The gravity loads serve as external forces that pull back on the rigid wall to ensure that the rigid wall and the hydraulic piston remain in contact during the setup phase and throughout the experiment. The manual locks located at the top of the front wall are then released allowing the wall to be supported by the hydraulic piston. It is important to prepare the system such that no disturbance or unwanted movement is created by unlocking the wall prior to launching the experiment. The side walls are coated with a

124

layer of grease and then overlain by a polyethylene sheet. Since no significant movement is expected to take place at the floor level, the floor is covered by a polyethylene sheet without coating it with grease. It was found more convenient to keep the bottom floor free from greasy material to allow for continuous access inside the system after the experiment is completed. Once the inside surface of the system is prepared, all sensors are tethered before filling the system with dry granular soil.

At this stage, the retaining system is ready to be filled with the backfill material. P-y curves for three backfill densities are to be constructed and studied: $1550 \ kg/m^3, 1650 \ kg/m^3, 1750 \ kg/m^3$. To provide a uniform density throughout the retained soil bed, the system is filled with sand using pluviation (see Section 5.5). The height of the fall and the size of the orifice used to control the flow rate for each soil density are summarized in Table 6.1. A trial pluviation test is conducted on a miniature wooden box ($10 \times 40 \times 60 \ cm^3$) to ensure that the target density can be reached (see Figure 6.1). The traveling hopper is filled with sand and weighed before and after the raining of sand to determine the weight of soil dropped (see figure 6.2). The total weight of sand dropped is another method used to check the target density. The sand is dropped in layers 3-5cm thickness until the total depth of 120 cm is reached (see Figure 6.3). Before launching the experiment, readings indicating at rest pressures are recorded.

Table 6.1 The pluviation setup used to achieve the desired target densities.

| Target density (kg/m$^3$) | Actual Density (kg/m$^3$) | Height of the fall (cm) | # of opening x diameter of orifice | Flow rate kg/min/cm$^2$ |
|---|---|---|---|---|
| 1550 | 1547 | 10 | 5 x 20 mm | 0.481 |
| 1650 | 1668 | 35 | 4 x 13 mm | 0.145 |
| 1750 | 1748 | 60 | 4 x 8 mm | 0.033 |



Figure 6.1 Trail test on a miniature wooden box



Figure 6.2 Weighing the traveling hopper

Figure 6.3 Filling the retaining system with granular soil using pluviation

A hand-operated displacement-controlled hydraulic piston, capable of moving in increments of 0.01mm, was used to displace the top of the rigid wall horizontally. To limit the development of frictional sidewall forces, the speed of the top-wall movement had to be carefully monitored. Displacing the wall at a fast rate can result in an increase in the hydrostatic frictional forces produced by the grease layer at the side wall. The magnitude of the hydrostatic frictional forces was measured by the friction sensor installed at the sidewall. To keep the frictional forces at bay, several precautionary measures were considered. First, the rate of wall movement was kept as low as possible. This was accomplished by pumping the hydraulic piston using small numerous strokes. Second, after each increment of wall displacement, the wall movement was stopped (2 min – 10 min) in order for the system to release/dissipate any built-up frictional stresses at the sidewalls. This was repeated at all wall locations where the lateral earth pressure was recorded. At the end of each experiment, the soil retaining system is emptied as described in Chapter 5. The weight of small container buried inside the retaining system is measured and the density is checked for the third time.

## C. Testing Program for Static p-y Curves

The experimental program involves subjecting the top rigid wall to two successive phases of wall displacements. Phase 1 constitutes displacing the top wall from the at-rest position to -8 mm in the active direction, [0, -8 mm] while Phase 2, succeeding Phase 1, constitutes displacing the top wall from the -8mm to 120 mm in the passive direction, [-8, 120 mm]. The testing program is summarized in Figure 6.4. The characterization of static p-y curves (active and passive) is accomplished through these two phases of wall displacement. The -8mm top-wall displacement in phase 1 is considered sufficient to construct the active p-y curves needed and at the same time it is considered insignificant to influence the passive soil behavior in phase 2. This justifies the use of a single experiment instead of two independent experiments. The traveling distance within each phase is carried out using incremental steps. An intermittent waiting period of 2 mins to 10 mins was observed between each step to allow the dissipation of frictional forces built up at the sidewall.
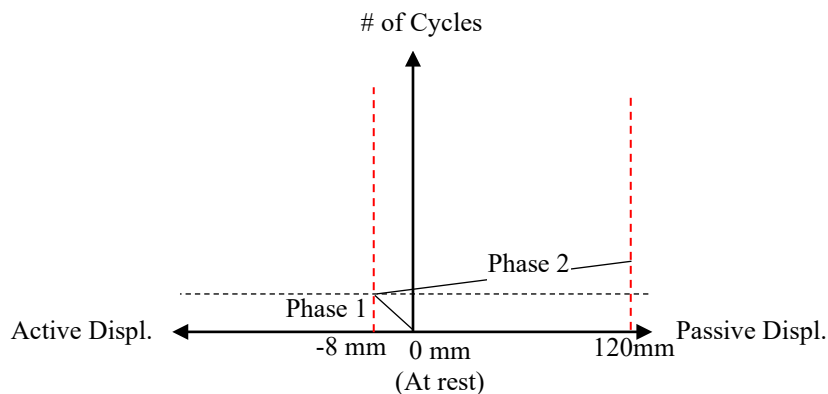


Figure 6.4 Experimental displacement (top of wall displacement)

## D. Results and Analysis

### 1. *Static Loading on Medium Dense Sand*

P-y curves constructed from the data collected at the four sensors for the case of medium dense soil ($\gamma = 1650 \; kg/m^3$) are shown on Figures 6.5 and 6.6. Figure 6.5 plots the lateral earth pressures as the wall is displaced in the active direction. The at-rest pressures and the limit-state Coulomb pressures are denoted on the figure by a green and red hatched lines, respectively. As shown in the figure, the experimentally derived pressures fall within the theoretical limits. This verifies the validity of the constructed experiment.

From the onset of the experiment, Sensor #1 read a constant pressure that is almost close to the active limit-state pressure. The proximity of Sensor #1 to the hydraulic piston at the top of the wall renders it sensitive to any accidental movement during the preparation process. From the shape of the p-y curves shown on Figure 6.5, few observations on the behavior of active p-y curves can be noted. Active p-y curves are characterized by a monotonic decrease in pressure from the at-rest pressure until limit-state active pressure. The curves are non-linear in shape with an observed decrease in the rate of stress loss with increased wall displacement. Active limit-state pressures are associated on the figure with stability in the recorded pressure. Figure 6.5 clearly indicates that the lateral earth pressures are highly sensitive to active wall displacement. A top wall displacement of -8mm was sufficient to drop the lateral pressures from the at-rest pressure to limit-state pressure at all sensors. In fact, local displacements as low as 2mm could be considered sufficient to mobilize the active limit state in the majority of the sensors.
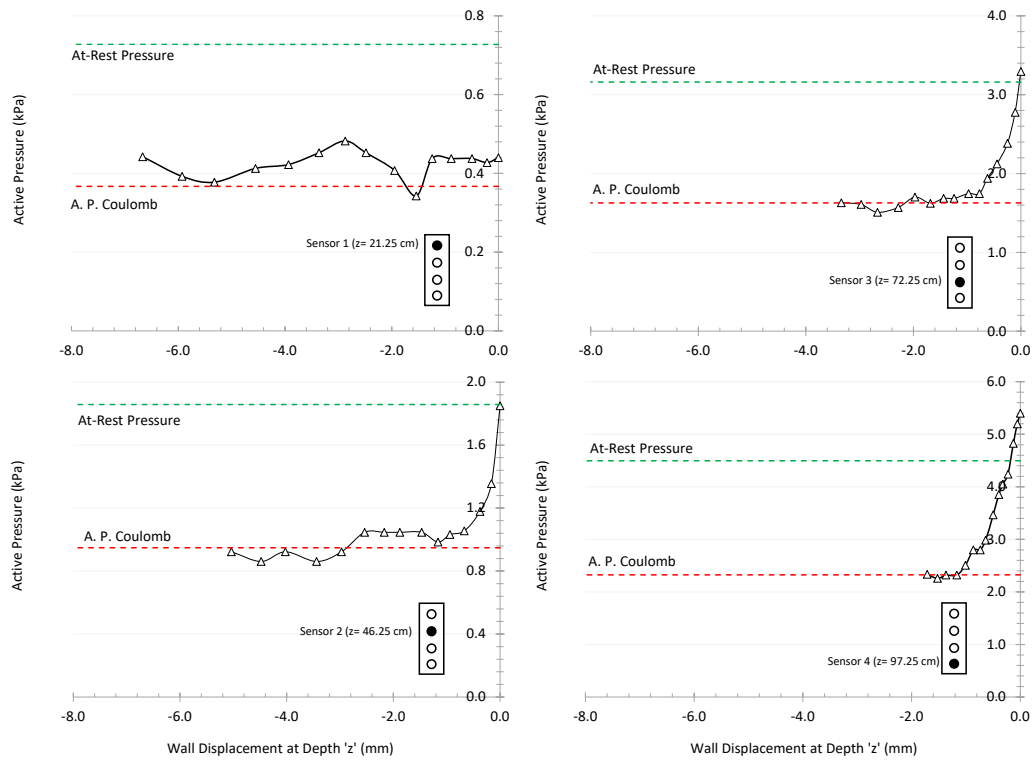
Figure 6.5 Static active p-y curve for medium-dense backfill ($1650\ kg/m^3$)

Figures 6.6 shows the lateral passive pressures recorded at four pressure sensors as the wall was pushed from the active side to the passive side. Originally, the curves were constructed between the top wall intervals of -8mm and 120mm, in line with the experimental program presented earlier. However, for better presentation, the passive p-y curves shown in Figure 6.6 were shifted to the right such that each p-y curve would start from the at-rest pressure. As noted earlier, the small active movement of -8mm at the top of the wall is expected to have an insignificant effect of the passive p-y response, and therefore, shifting the curves as done in Figure 6.6 is justified.

To put the measured passive p-y response in perspective, different limit-state pressures based on renown theories are superimposed on Figure 6.6. These include

Coulomb's theory, Lancellota's method, and Lui et al. method which is based on log-spiral theory. The theoretical passive pressures were determined from soil and interface properties, $\phi$ and $\delta$, that were extracted from the data presented in Figures 5.29 and 5.32, respectively. Values for $\phi$, $\delta$, and $k_p$ are summarized in Table 6.2. The parameters $k_{p,co}$, $k_{p,la}$, and $k_{p,lu}$ denote passive soil coefficients calculated using Coulumb, Lancellota, and Lui theories, respectively.

As expected, results on Figure 6.6 indicate that the measured p-y response is bounded by the at-rest pressure and the passive limit-state pressure. The measured at-rest to passive p-y response is characterized by a monotonic increase in lateral pressure with passive wall displacement. The responses are non-linear in shape with varying intensity depending on the location/depth of the sensor and the magnitude of applied displacement. The p-y response at Sensor #1 is S-shaped, presumably a characteristic of relatively unconfined sand. The p-y response at Sensors #2, #3 and #4 have a slight negative curvature which would be more visible if higher pressures were reached.

Among the four sensors, only Sensor #1 traveled enough distance (wall displacement of 70mm) for the mobilized stresses to stabilize at limit state. On the other hand, the mobilized stresses at Sensors #2, #3 and #4 increased either at the same rate or with a slightly reduced rate showing no signed of asymptotic behavior. This is due to the relatively small wall displacements that were applied at these sensors location. The small displacements were not large enough to induce non-linearity in the p-y response. As a result, passive limit state was not reached in the deep sensors. The variation in the wall deformations at different sensor locations is attributed to the pure rotational movement of the wall whereby Sensor #1 travels the most and Sensor #4 the least.

Table 6.2 Passive pressure coefficient for medium dense soil

| Sensor depth | $\phi\ (deg)$ | $\delta\ (deg)$ | $k_{p,Co}$ | $k_{p,La}$ | $k_{p,Lu}$ |
|---|---|---|---|---|---|
| #1 (z=21.5 cm) | 52.06 | 18.00 | 27.59 | 16.47 | 15.79 |
| #2 (z=46.5 cm) | 48.77 | 18.00 | 19.95 | 13.25 | 14.26 |
| #3 (z=76.5 cm) | 46.88 | 18.00 | 16.88 | 11.79 | 13.26 |
| # 4 (z=97.5 cm) | 45.62 | 18.00 | 15.19 | 10.94 | 12.53 |
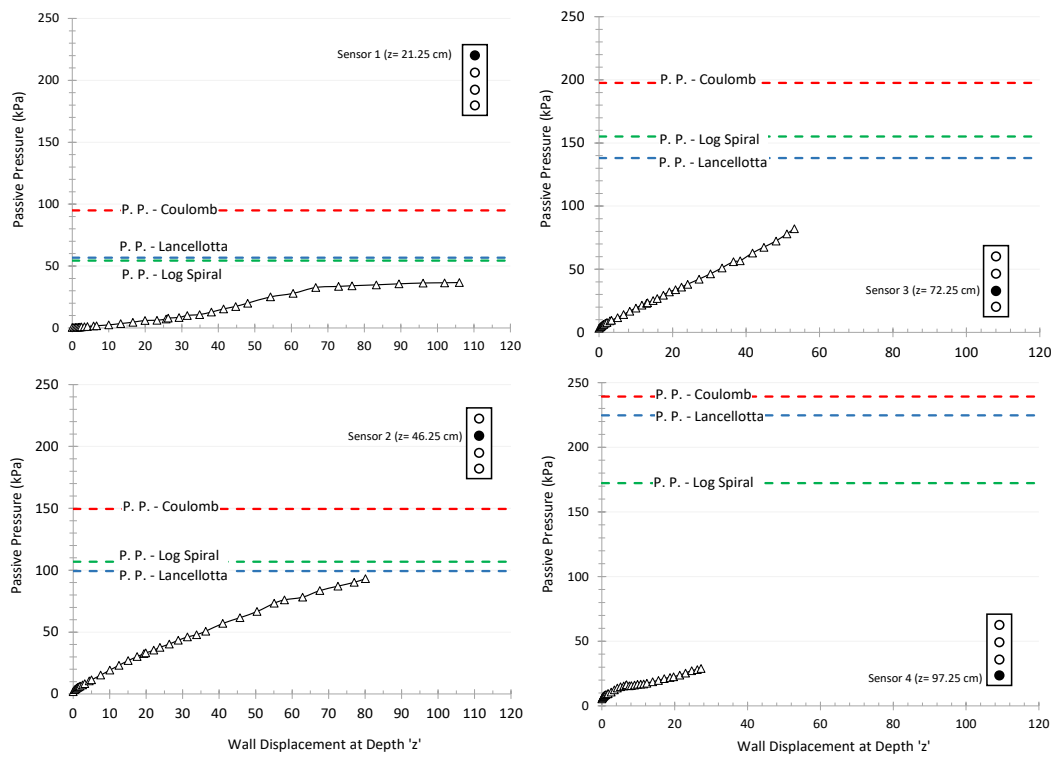


Figure 6.6 Static passive p-y curve for medium-dense backfill ($1650\ kg/m^3$)

Figure 6.7a & b compares active and passive p-y curves for all sensors. As shown in the figure, the rate of stress decrease in the case of active wall displacement or pressure increase in the case of passive wall displacement shows little dependency on the depth of the sensor (with the exception of sensor #1 in passive wall displacement). However, care should be taken before generalizing such a behavior. It should be kept in mind that the current experiments are conducted on a soil depth that is generally shallow (120 cm). Moreover, collecting data at four location within a wall height of 120 cm might not give enough variations between each sensor. These are reasons that can justify the rather consistent behavior between each sensor.

Figure 6.8 shows the pressure distribution along the wall height at top wall displacements of 30mm, 60mm, 90mm and 120mm. The pressure at the soil surface is assumed to be zero while the pressure at the bottom of the wall is assumed to be the at-rest pressure since no displacement takes place at the bottom hinge. According to Figure 6.8, the maximum pressure measured is recorded at Sensor #2 or at approximately 1/3 of the wall height from the surface. The pressure distribution shown in Figure 6.8 can be explained through the variations between the confinement pressure ($\gamma z$) and displacement of the wall at that given depth ($y$). It is known that lateral passive pressure increases with both confinement and wall displacement. In the case of a rigid wall pivoting about its bottom axis, larger depths of confinement are accompanied with smaller wall displacements. When the latter outweighs the former, a decrease in lateral pressure is registered as was the case in sensors #3 and #4.
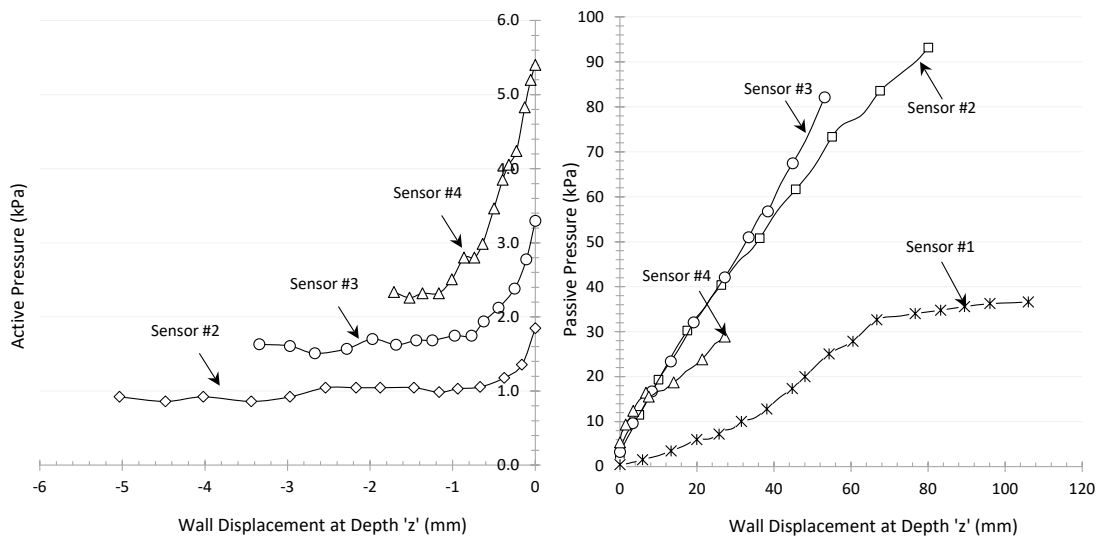
Figure 6.7 (a) Active p-y curves for medium dense soil for all sensors and (b) passive p-y curves for medium dense soil for all sensors
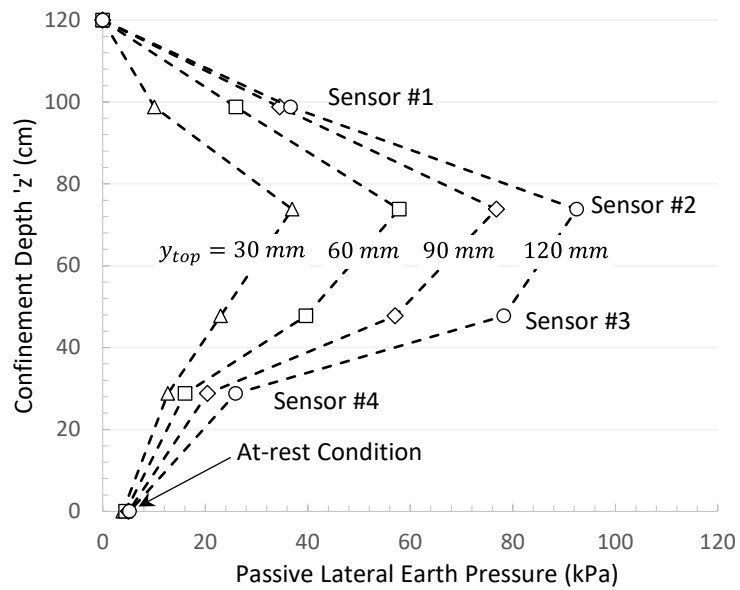


Figure 6.8 Lateral passive pressure recorded along the depth of the rigid wall at various top wall displacement 'y'

134

It should be noted that displacing the wall in the passive direction resulted in an upward deformation (surface heave) in the backfill, particularly in the vicinity of the wall. The distance over which heave was observed reached a maximum of 72cm from the face of the wall (~30% of the total length of the retaining system) at maximum wall displacement. At 80 mm of passive top wall displacement, a surface trace of one of the failure planes propagated to the surface (See Fig 6.9) at a distance of about 17.5 cm from the face of the wall. This was followed by another surface trace at a top wall displacement of 92.5mm (Figure 6.9). The second failure plane was observed at a distance of about 30cm from the face of the rotating wall.

The failure planes were marked with darker soil to increase their visibility. As shown in the Figure 6.9, the surface traces of both failure planes are non-planar in shape. They can be approximated as trapezoidal in shape with the two end segments pulled back towards the rigid wall (Figure 6.10). The shape of the failure plane is probably affected by the friction on the side walls. The sidewall friction restrains the sand bed at the edges of the tank from displacing horizontally as the wall is forced to rotate. The presence of a horizontal segment in the failure plane gives assurance that the central part of the failure plane is seems to be unaffected by the boundary effects due to side wall friction. Since all pressure sensors are located at the center of the rotating wall away from the side wall edges, it is expected that the pressure readings in the sensors were not affected by the side wall friction. It should be noted that the experimental setup was designed to minimize the sidewall friction to the smallest values possible using the alternating layers of nylon and grease.

Figure 6.9 Surface traces of two failure planes forming in front of the wall in the medium-dense soil
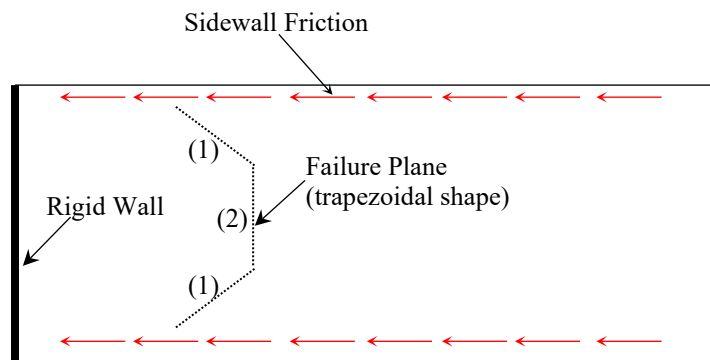


Figure 6.10 Shape of the failure planes as formed in the medium-dense soil
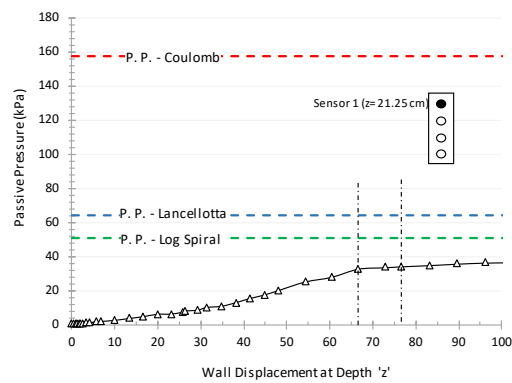


Figure 6.11 Location of the rigid wall when failure planes were observed

136

Figure 6.11 shows the passive p-y response of Sensor #1 with the wall displacements at which the failure planes surfaced marked on the figure by two dash-dotted lines. The figure indicates that the surface traces of the two failure planes were accompanied by a significant reduction in the rate of pressure increase whereby the p-y response shifts towards an asymptotic response. It is expected that when a failure plane completes its trajectory towards the surface of the soil (i.e. becomes visible), constant shear stresses along the failure plane are formed. This explains the approximate stable p-y response observed at Sensor #1. Meanwhile, no effect of failure-plane formation was observed on the p-y response of Sensors #2, #3, and #4. The distance from the rigid wall to failures planes 1 and 2 were measured to be 17.5 cm and 30 cm, respectively. The proximity of the failure planes to the rotating wall implies that the two planes originated from shallow depths that are expected to fall between Sensors #1 and #2.

The interface friction angle at the side wall was calculated during passive wall displacement using the friction sensor and the force sensor installed at the sidewalls as described in Chapter 5. Figure 6.12 plots the mobilized interface friction angle calculated at every incremental step of top wall displacement. Two readings are shown on Figure 6.12. The 1st reading denotes the interface friction angle calculated at the beginning of every intermittent pause while the 2nd reading denotes the interface friction angle calculated at the end of the intermittent pause. The 1st reading provides information on the effect of rate of loading while the 2nd reading provides information on the residual frictional forces remaining within the system before the second incremental displacement is launched.
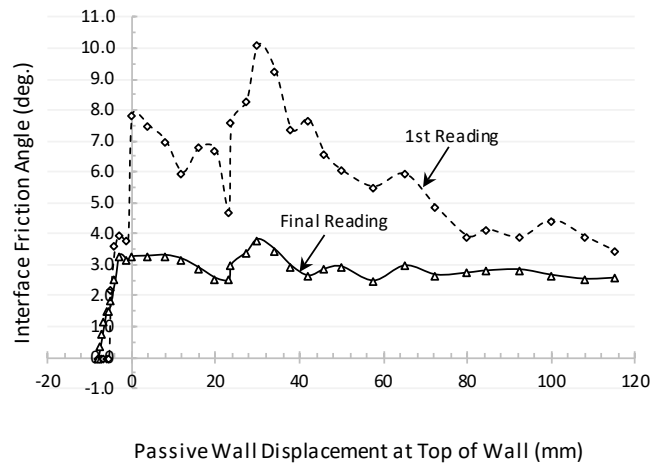
Figure 6.12 Interface friction angle calculated at side wall

During the experiment, the 1st reading was closely monitored as the velocity of the hydraulic pump was continuously modified to keep the 1st reading as low as possible but within practical consideration. As noted earlier, the velocity of the hydraulic pump and the magnitude of the side friction walls are related through the hydrostatic pressure produced by the grease layer placed between the polyethylene sheet and the acrylic plate (see Chapter 5.B.3). Figure 6.12 indicates that the maximum interface friction angles at the sidewalls when the lateral pressures were recorded did not exceed 4° deg. This is relatively low therefore, validating the process adopted for reducing the side wall friction in the experimental setup/

### 2. *Effect of Relative Density of the Backfill on the P-Y Response*

The experiment conducted on medium dense soil was repeated for the cases of loose and dense backfill. The material properties for both types of soils are given in Section 5.C. Active and passive p-y responses at Sensors #2 and #3 for the three types of soils (loose, medium-dense, and dense) are compared in Figure 6.13a & b.

138
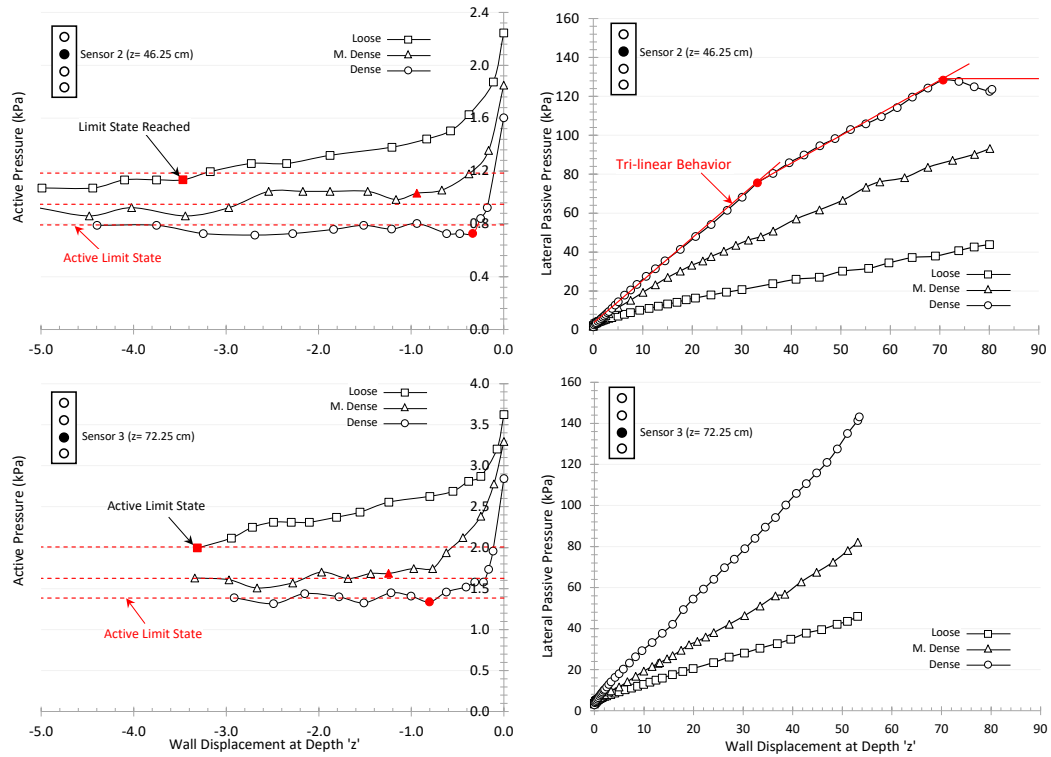
Figure 6.13 Active and passive p-y response recorded at sensors #2 and #3 for loose, medium-dense and dense soils

The at-rest to active p-y response of loose and dense sands was relatively similar to the response observed in the case of medium-dense soil. However, as shown in Figure 6.13a, the rate at which active p-y curves approach their asymptotic values varies with relative density. The solid markers shown on Figure 6.13a denote the wall displacement at which active limit-state is reached for each soil. As indicated in the figure, loose soil was the slowest to approach the limit-state followed by medium-dense and dense sand, respectively. The amount of wall displacement required to mobilize active conditions for the case of loose soil (3 to 4 mm) is approximately 3.5 times that for medium-dense soil and 8.0 times that of dense soil. Since the rate of decrease in lateral pressure with active wall displacement is expected to be correlated to the

stiffness of the backfill, it is expected that the active limit-state for looser soils will require larger wall displacements in order for the lateral pressure at the wall to stabilize at active conditions.

Figure 6.13b shows the passive p-y response at Sensors #2 and #3 for the three types of soils. Here too the sensitivity of passive p-y response to the type of soils is clearly visible. Denser soils tend to exhibit stiffer p-y responses compared to looser soils. For all p-y responses, a monotonic increase in passive pressure is recorded except for the p-y response given at Sensor #2 for the case of dense soil. For that particular case, soil softening was recorded after the peak passive pressure was reached, a common characteristic of dense soil. A non-linear behavior in passive p-y response is observed at Sensor #2. Such behavior can also be seen at Sensor #3, but with less intensity due to the small wall movement recorded at that sensor. A tri-linear model can be used to fit the passive p-y response as shown on Figure 6.13b. However, for practical reasons, a hyperbolic model similar to that presented in Chapter 5 would serve as a simpler alternative that requires less parametric calibration.

Figure 6.14 shows two failure planes that formed during the passive displacement of the retained dense soil. No failure planes formed for the case of loose sand. The first and second failure planes occurred at a top wall displacement of $100mm$ (~8% drift) and $110mm$ (~10% drift), respectively. The magnitude of the wall displacements corresponding to the formation of the failure planes are shown with the measured p-y curve on Figure 6.15 for the case of dense backfill. As shown in the figure, the surfacing of the failure planes was associated with the registration of a peak pressure at one of the sensors (Sensor #2). The fact that the recorded pressure at Sensor

#3 was not affected by the formation of the failure plane indicates that the lower tip of

the failure plane lies at or slightly above Sensor #2.



Figure 6.14 Formation of failure planes for the case of dense soil
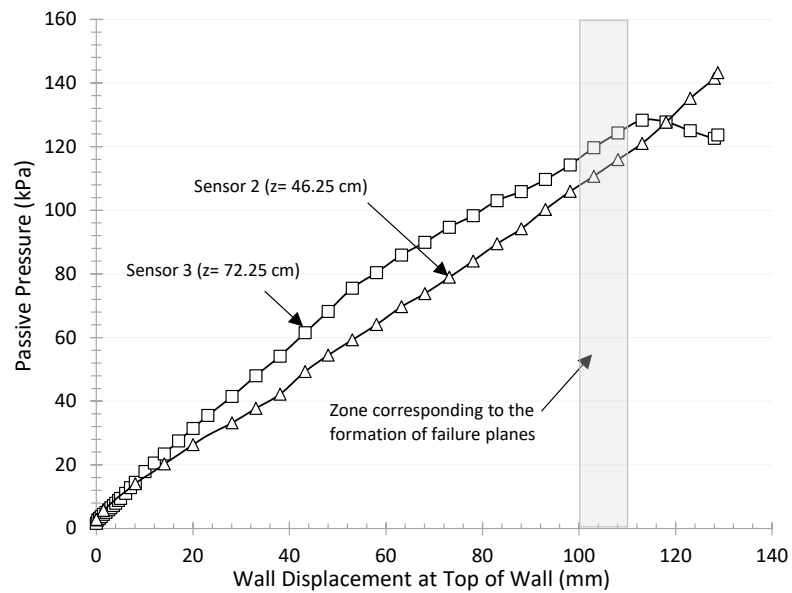


Figure 6.15 Wall displacement corresponding to the formation of failure planes

Both failure planes were non-planar in shape having a concavity directed towards the rigid wall. As noted earlier in the case of the medium-dense soil, the non-planar failure planes are indicative of the presence of sidewall frictional forces. The distances from the rigid wall to the crest/tip of the 1st and 2nd failure planes were measured to be 36cm and 81cm, respectively. In comparison with the failure planes that occurred in the case of medium-dense soil (Figure 6.9), the failure planes in dense soil occurred at larger distances from the rotating wall than that of the medium-dense soil. This indicates that denser soils form shallower passive failure wedges than looser soils. This falls in-line with the general understanding of Rankine's theory where the angle which the failure plane makes with the vertical depends on the soil angle of friction and is calculated to be $45 + \phi/2$. Since denser soils have larger values of $\phi$, it would be expected that denser soils result in less steep (with the horizontal) failure wedges than looser soils (Figure 6.16).
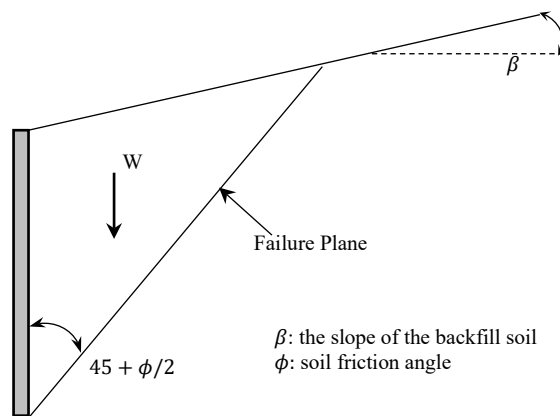


Figure 6.16 Failure wedge in soil retained by Rankine's wall (frictionless wall)

### E. Comparison with Proposed Models

In chapters 3 and 4, prediction models were proposed for active and passive p-y curves for granular soil retained by rigid walls. The proposed active model had two major limitations. First, it applies for rigid walls with heights greater than 5m and second the wall interface friction angle $\delta$ should be greater than $0.6\phi$. Both considerations are not met in the above conducted experiments and therefore no comparison between the experimentally recorded data and the proposed numerical expression for the prediction of active p-y curves can be made. On the other hand, the model used for the prediction of passive p-y response is more general and therefore can be used it check its validity against experimental results.

Figure 6.17 compares the p-y model proposed by Briaud and Kim and the hyperbolic model presented in Chapter 4 with the experimentally derived passive p-y curves. Basing their finding on large scale experiments, Briaud and Kim proposed an elastic perfectly plastic model for the prediction of the p-y response for soil retained by flexible walls. The elastic portion of the proposed model is delimited by the at rest pressure at $y = 0\ mm$ and Coulomb's passive pressure assumed at a wall displacement $y = 13\ mm$. When comparing their proposed model with the experimental results recorded for medium-dense granular soil, Briaud and Kim's model is found to clearly overestimate the experimental p-y response. Their proposed model prematurely assumes the occurrence of passive limit-state. The experiment conducted on medium dense soil, for instance, indicated that a wall displacement of more than $y = 70mm$ is necessary for plastic deformation in the soil to be reached. This is much larger than the 13mm proposed by Briaud and Kim. The hyperbolic model, on the other hand, presents a better

fit, though it tends to overestimate the passive pressure. The parameters used for the

hyperbolic model are given in Table 6.3.
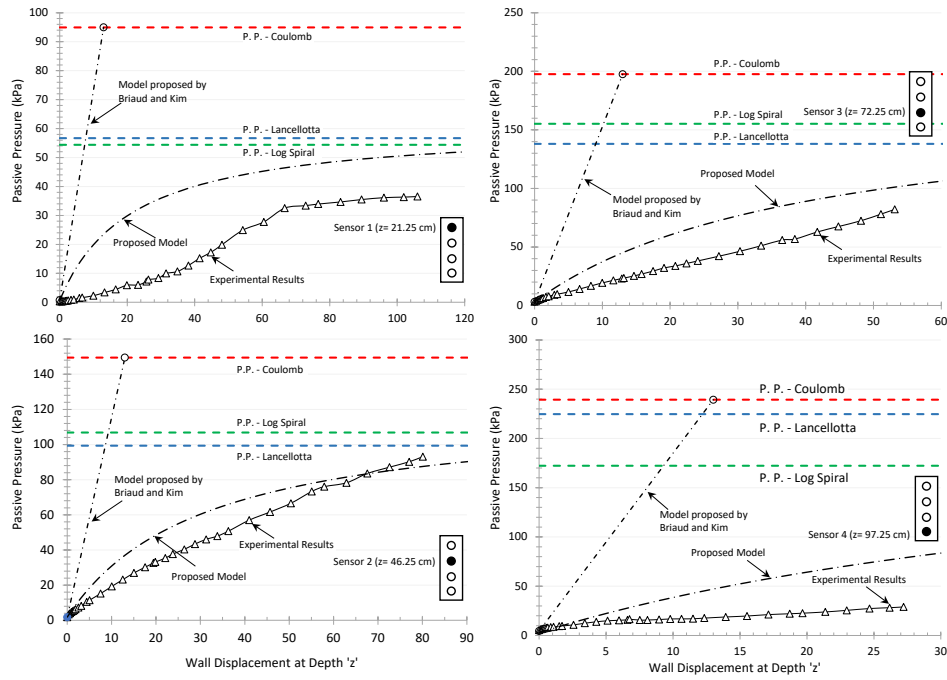


Figure 6.17 Comparison between p-y curve constructed experimentally and the model
proposed in Chapter 4 and model proposed by Briaud and Kim (medium sand)

Table 6.3 Parameters used for the hyperbolic model

|  | Sensor #1 | Sensor #2 | Sensor #3 | Sensor #4 |
|---|---|---|---|---|
| z (m) | 0.2125 | 0.46 | 0.72 | 0.97 |
| $E_{50}^{ref}\ (kPa)$ | 11.7 | 11.7 | 11.7 | 11.7 |
| $\varphi\ (^o)$ | 52 | 48.7 | 47.0 | 45.6 |
| $\delta\ (^o)$ | 18 | 18 | 18 | 18 |
| $\gamma\ (kN/m^3)$ | 16.2 | 16.2 | 16.2 | 16.2 |
| $p_o$ (kPa) | 0.73 | 1.86 | 3.16 | 2.85 |
| $p_f$ (kPa) | 54.37 | 106.9 | 155.2 | 197.5 |
| $R_f$ | 0.9 | 0.9 | 0.9 | 0.9 |
| Co | 2.82 | 3.84 | 4.26 | 4.26 |
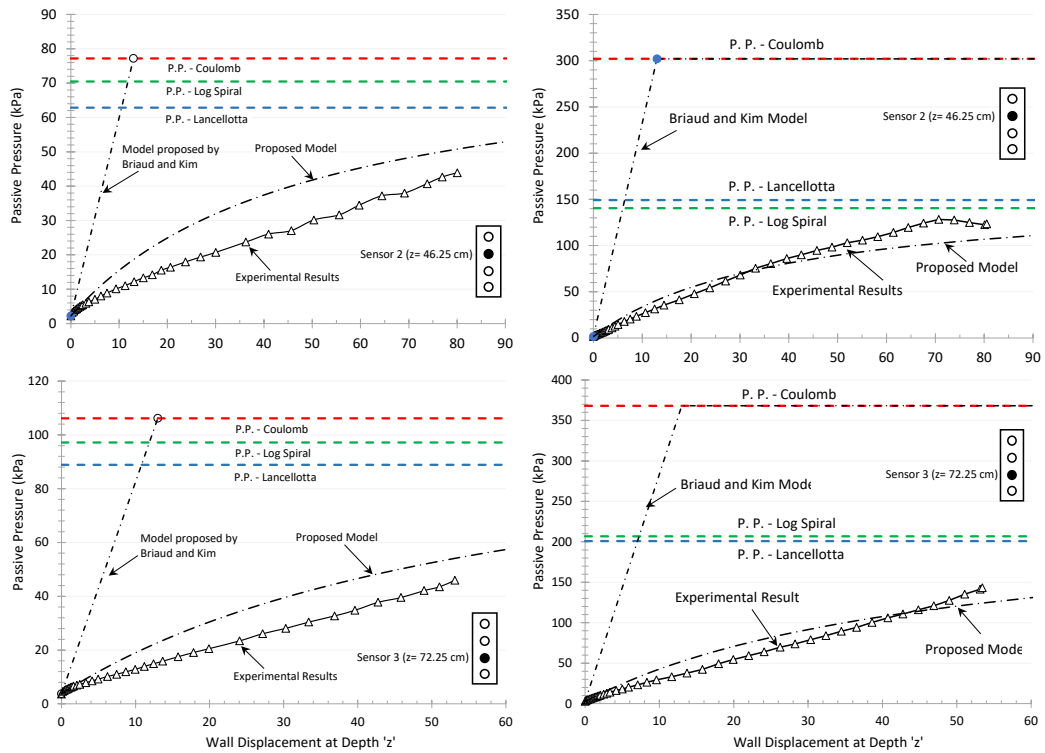
Figure 6.18 Comparison between the model presented in Chapter 4 with that proposed by Briaud and Kim for the cases of loose and dense soil

similar comparison was conducted on the experimental p-y curves derived for the cases of loose and dense soil. The comparison is presented on Figure 6.18. Again, for the cases of both loose and dense soil, the model presented in Chapter 4 presents a better fit for the data than the model proposed by Briaud and Kim.

### F. Additional Cyclic Loading

In this section, the effect of "large-displacement" cycles of loading on the p-y response of retained loose, medium-dense and dense granular soils will be discussed. The term 'large-displacement' is used in this section to differentiate these cycles from the "smaller-displacement" repetitive cycles that will be investigated in Chapter 7 to

mimic seismic loading of the wall. The large cyclic loadings that will be discussed in this section were conducted as a continuation to the static experiments discussed earlier. At the end of every previous experiment, the pivoting rigid wall was further oscillated three times between the two preset top wall displacements of -8mm and +120mm to form a total of three successive cycles.

Figure 6.19 shows the experimental program that was adopted for the large-displacement cyclic loading. As shown in the figure, the first cycle includes the results from the passive p-y response in addition to the active displacement that is needed to bring the wall back to -8mm wall displacement. It should be noted that such large cycles are improbable in real life; however, subjecting backfill soils to large passive displacements gives important information on the behavior of the retained soil loaded near its limit-state (assuming that the limit-state pressure will be achieved).

Figure 6.20 shows the p-y response for medium-dense soil when subjected to the three cyclic loading described above. The cycles are color coded and labeled per cycle number. Several behavioral traits can be observed and define the p-y response of granular soil subject to large cyclic loading.

Beginning with the passive p-y response, Figure 6.20 shows that there is an increase in the passive soil resistance with each loading cycle. This is probably attributed to a change in the backfill density following each passive cycle of loading. It is expected that the large passive displacement will deform the soil largely into a plastic phase. Returning the wall back to its original position, on the other hand, will not revert the soil density to its original conditions. As a result, densification of the backfill soil will occur after each cyclic loading.

Second, the peak pressure recorded at the end of each cycle increases with each cycle as shown by the pressure recorded by Sensors #2 and #3. This holds true as long as the recorded peak pressure does not reach the limit-state pressure.
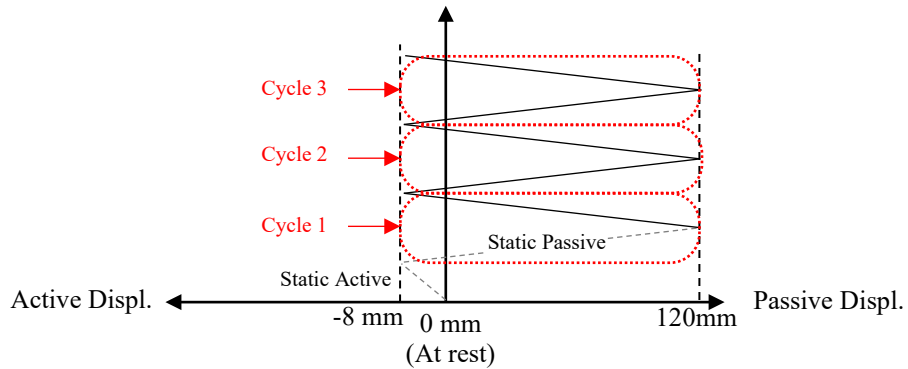


Figure 6.19 Large-Displacement cyclic loadings schedule (top of wall displacement)
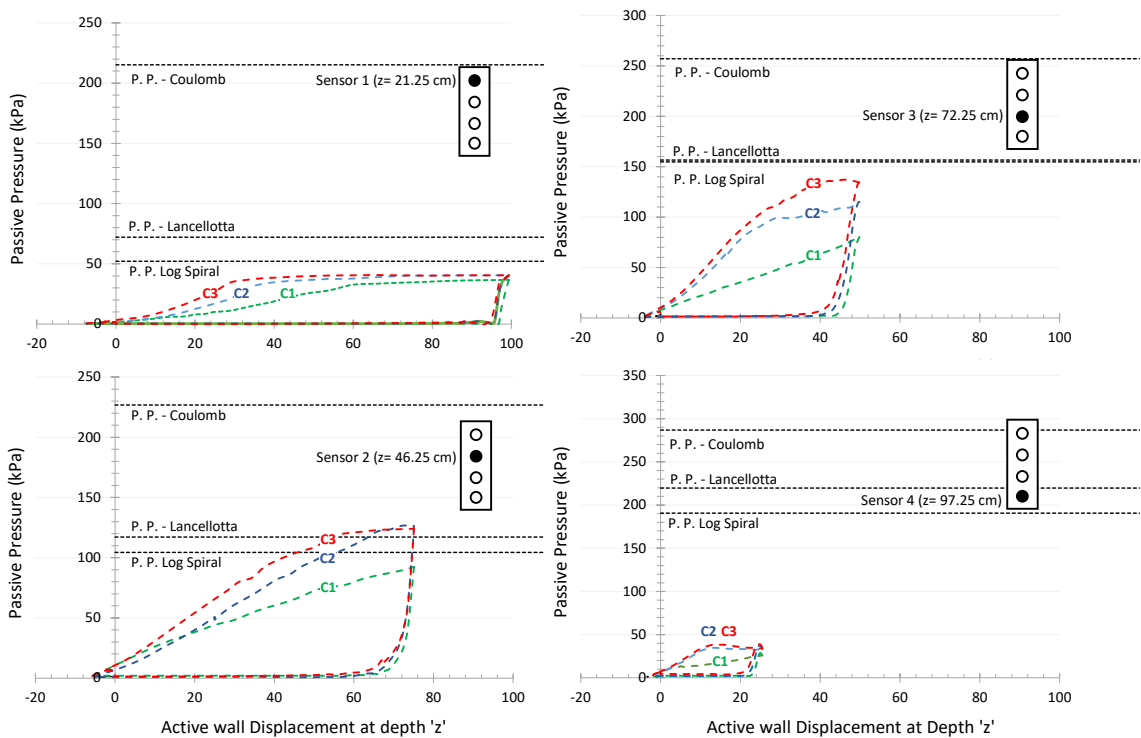


Figure 6.20 P-y response for medium-dense backfill when subjected to three large cyclic loadings

147

Third, a change in the shape of the passive p-y curves is observed. This is observed by comparing the passive p-y responses of cycles #1 with cycles #2 and #3. The passive p-y response of cycle #1 is most non-linear with a negative concavity. However, in cycles #2 and cycles #3, the p-y responses take on an S-shape. S-shaped p-y curves often result from the presence of a looser layer of soil behind the wall. The looser soil usually forms from the caving of top soil as the wall is displaced in the active direction. Once loaded the soft soil gradually densifies to form the lower part of an S-shaped curve.

Fourth, Figure 6.20 indicates that a large amount of top wall displacement is required for passive limit-state to be reached. Except for Sensor #1which is located at a depth of 20% of the wall height, none of the other sensors reached the limit-state during the first cycle of passive displacement. Only after the densification of the soil had taken place did the soil reach its limit-state. Finally, the theoretical passive limit-states determined by both log-spiral theory and Lancellota's lower bound theory seemed to best capture the passive pressure at the limit-state. Coulomb theory, on the other hand, over-estimated the limit-state by far. It has been shown that Coulomb's theory, based on the equilibrium of forces of a wedged plane, over predicts passive pressures for walls when $\delta > \phi/2$ (Kramer, 1996).

The term 'Preloaded active p-y curve' will used to denote the part of the curve that extends from the peak passive pressure recorded at $y = 120\ mm$ to the lowest lateral pressure recorded at $y = -8\ mm$. From Figure 6.20, several behavioral trends of preloaded p-y curves can be deduced. First, preloaded p-y curves can be characterized as monotonically decreasing curves that are nonlinear in shape. Second,

148

the shape of the curve is mainly dominated by the steep drop in lateral pressure recorded at the beginning of the curve. The lateral earth pressure accumulated from the passive wall displacement is lost within the first few millimeters of active wall displacement ($\approx$ $5mm$). Third, Figure 6.20 indicates that the initial slope of the active p-y response is independent of both the magnitude of the preloaded pressure and the number of cycles the retained soil has been subjected to. At any given sensor, there is almost an identical response in the three preloaded active p-y curves. Fourth, the initial slope of the loading curve and the initial slope of the unloading slope is significantly different with the latter being much steeper than the former. The unload-reload behavior of any prediction model that aims at incorporating the unloading portion of a previously loaded wall should reflect this observation. Finally, the shape of the active p-y curves originating from at-rest pressures differs from the preloaded p-y curves especially in terms of the rate of pressure dissipation. In this regard, a unified model for static and cyclic loading should be avoided.

In addition to the two failure planes presented in Figure 6.9, a new failure plane surfaced during the 3<sup>rd</sup> cycle (see Figure 6.21). What distinguished the 3<sup>rd</sup> failure plane from the rest is the distance from the face of the rotating wall at which it surfaced. The first two failure planes formed close to the rotating wall while the 3<sup>rd</sup> one formed at an approximate distance of 150 cm ($\approx$ 60% of the length of the bed). To assess the depth of the failure wedge, the p-y response for the 3<sup>rd</sup> cycle shown on Figure 6.22 is marked at the location were the 3<sup>rd</sup> failure plane was observed. Figure 6.22 indicates that all four sensors reached limit-state passive pressures when the failure plane was observed. This is indicative of the depth of the failure plane, which seems to have extended beyond the first three sensors.

Figure 6.21 Formation of a 3$^{rd}$ failure plane in response to three cyclic loading
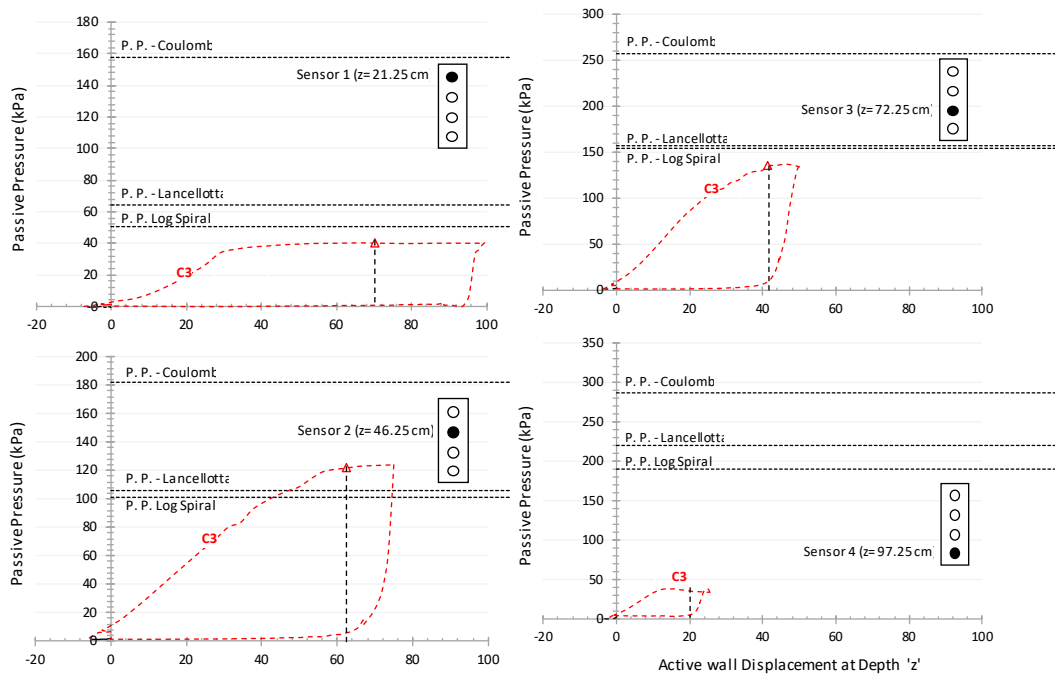


Figure 6.22 Surfacing of the third failure plane in relation to the observed p-y curves

The p-y responses for loose and dense soil due to large cyclic loading are shown on Figure 23. The p-y responses are shown only for Sensors #2 and #3. The effect of the soil density on the response of soil following large-displacement cyclic loading is clearly indicated in Figure 23. First, in regard to the limit-state pressure, for the case of loose soil, it took three cycles for Sensors #2 to reach the limit-states pressures; meanwhile, limit-state pressures were noticed in the first cycle for the case of dense soil. Second, densification of soil by large cyclic loading is more pronounced on loose soil than dense soil. The percent increase in lateral pressures between two successive cycles at any given wall displacement is more significant in the case of loose soil than dense soil. Finally, the small error between the theoretically calculated and experimentally determined limit-state pressures gives confidence in the characterization of the retained soil and the methodology used to conduct the experiments.

Figure 6.24 shows the three failure planes that formed within the soil bed for the case of the dense soil. The first and second failure planes formed during the first passive cycle while the third failure plane formed during the third cycle. The distances from the rigid wall to the crest of the 1$^{st}$, 2$^{nd}$, and 3$^{rd}$ failure planes were measured to be 36cm, 81cm, and 106cm, respectively.
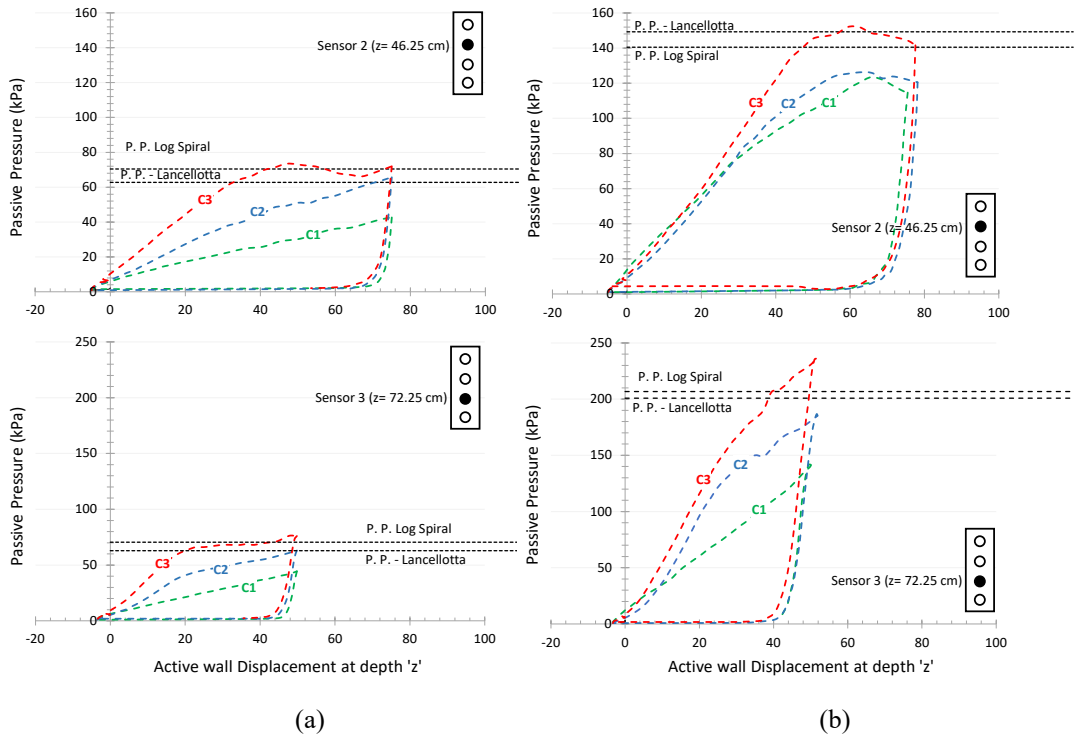
Figure 6.23 P-y response for (a) loose soil and (b) dense soil due to three cyclic loadings



Figure 6.24 Failure planes formed in the experiment conducted on dense soil

152

### G. Conclusion

Based on the results of three static tests (three relative densities) that were conducted by displacing the wall from its at-rest condition to an active condition, followed by passive loading up to a maximum wall displacement of 10% of the height of the wall (around 120 mm), the following conclusions can be made:

1. At-rest to active p-y curves are relatively curved with an observed decrease in the rate of stress loss with increased wall displacement. The measured p-y response is highly sensitive to the active wall displacement with a top wall displacement of -8mm being sufficient to reduce the lateral pressures from the at-rest pressure to active limit-state pressure at all sensors.

2. At-rest to passive p-y curves are characterized by a monotonic increase in lateral pressure with passive wall displacement. The responses are non-linear in shape with varying intensity depending on the location/depth of the sensor and the magnitude of applied displacement. Among the four sensors, only the upper sensor recorded stresses that reached passive conditions. The stresses in the deeper sensors showed no signs of asymptotic behavior due to the relatively small wall displacements that were not large enough to induce non-linearity in the p-y response. As a result, passive limit state was not reached in the deep sensors.

3. The effect of relative density on both the active and the passive p-y responses was significant. Loose sand was the slowest to approach the active limit-state, with the amount of wall displacement required to mobilize active conditions for the case of loose soil (3 to 4 mm) being approximately 3.5 times that for medium-dense soil and 8.0 times that of dense soil. On the other hand, the

passive response indicated that denser soils tend to exhibit stiffer p-y responses compared to looser soils.

4. For all the cases tested, results indicated that the passive p-y curves proposed by Briaud and Kim prematurely predict the occurrence of passive limit-state. As an example, the experiment conducted on medium dense soil indicated that a wall displacement of more than y=70mm is necessary passive conditions to be achieved. This is much larger than the 13mm proposed by Briaud and Kim. The hyperbolic model that was proposed in this dissertation based on the finite element analyses presented a better fit to the measured p-y response, though it tends to overestimate the passive pressure.

# CHAPTER 7

# ACTIVE AND PASSIVE P-Y RESPONSE UNDER CYCLIC

# LOADING

### A. Introduction

In this chapter, the test setup will be used to measure the cyclic p-y response of the wall supporting medium dense sand. The procedure that is followed involves initiating a 2-mm displacement cycle where the wall is moved from the at-rest position towards the active side until reaching -2 mm, and then pushed in the passive direction by 4 mm to reach +2 mm. This cycle is repeated 10 times. Once the set is completed, cycles with the other displacement amplitudes are initiated (5 mm, 10 mm, and 20 mm) in chronological order, and at the end of the 20 mm set, a static push of 120 mm is executed towards the passive side. The results from this test will also be compared to the cyclic p-y curves reported in Ghanem (2019) for the cases of loose and dense sand backfill.

### B. Experimental Setup

As in the case of the tests reported in Chapter 6, the sidewalls of the test tank are first coated with a thin layer of grease and covered with a thin plastic sheet. Using a permanent marker, the plastic sheet is marked at a height of 120cm from the bottom of the retaining system. This mark is used to locate the top surface of the soil bed. The manual locks at the top of the rigid wall are released and the steel plates are hung from the pulley system to provide a continuous contact between the hydraulic piston and the rigid wall throughout the experiment. The LVDT, force sensors, and vibrating wire

sensors are tethered. A small round container used to check the density is placed at the back end of the retaining system. Once the experiment is finished and the soil emptied, the container is weighed and the backfill density calculated.

The dry sand is rained inside the retaining system using pluviation. Three orifices, each having a diameter of 13mm, were used to control the flow of the sand from the hopper. The sand was dropped at a height of 35cm in consecutive layers of 3-5cm. The size of orifice and the height of the drop were specifically chosen to produce a medium-dense soil with a density of $\rho = 1650\ kg/m^3$. Once the retaining system is filled to a height of 120cm, the actual density is back-calculated by dividing the total weight of the sand dropped into the system by the volume of the soil bed. In the present case, the actual density was calculated to be $\rho = 1663\ kg/m^3$. This shows the accuracy that can be achieved by the specifically designed pluviator for the current experiment.

### C. Testing Program

The experimental program involved subjecting the top of the rigid wall to 40 consecutive cycles of lateral displacement. The 40 cycles are sub-divided into four displacement intervals: [$\pm$ 2mm] (0.17% drift), [$\pm$5mm] (0.41% drift), [$\pm$10mm] (0.83% drift), and [$\pm$20mm] (1.67% drift). The cyclic testing program is summarized on Figure 7.1. Each displacement interval was cycled 10 times before moving to the higher interval. A complete cycle is defined by the distance the wall moves between two consecutive lower bounds of a given interval. A cycle consists of a passive wall movement (wall moves into the backfill) followed by an active wall movement. When the number of cycles in a given interval was completed, the wall was moved to the lower bound of the next displacement interval and a new set of cycles is initiated. The

156

1st cycle in the new displacement interval is referred to as a transitional cycle. Transitional cycles are marked on Figure 7.1 by a heavy solid line. They are distinguished from the rest of the cycles within the same drift level because of their distinctive response as will be seen in the Results and Analysis section.

### D. Results and Analysis

The raw data that was collected in each displacement cycle consists of pressure readings recorded by the pressure sensors and a horizontal displacement reading recorded by the LVDT located at the top of the wall. The pressure sensors were located along the center of the wall at depths of 21.25cm, 46.25cm, 72.25cm and 100cm from the top of the soil bed. Throughout the rest of the chapter, the sensors will be referred to as Sensor #1 to Sensor #4 whereby Sensor #1 is the shallowest and Sensor #4 is the deepest. Given that the rotating wall was designed and constructed to be rigid, the top wall displacement was used to predict the displacement at every sensor location using linear interpolation. This allowed for constructing p-y curves at each sensor location.

Figure 7.2 shows the p-y response recorded at Sensors #1, #2, and #3, respectively, as the rigid wall was cycled between the four displacement intervals described in Figure 7.1. The lateral movement at Sensor #4 was relatively small due to its proximity to the bottom hinge. As a result, the p-y response at that level showed a lot of irregularities and was excluded from the presented results. The limits of the distance traveled by each sensor is indicated on the figures by two vertical lines extending from the horizontal axis.
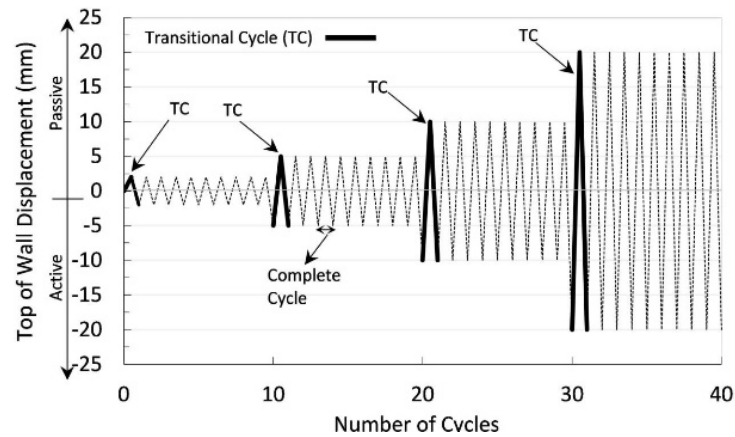
Figure 7.1 Testing program for the cyclic loading of medium-dense sand

To put the results into perspective, the theoretical active and passive limit state pressures as computed from the theories of Coulomb (1776) and Lui et. al (2018) were calculated and superimposed onto Figure 7.2. The soil parameters used in determining the lateral pressures by both theories are summarized in the previous chapter in Table 6.2. When determining the interface friction angle at the rigid wall, whose surface consists partly of an acrylic plate and partly of steel plates (sensors), a weighted average of both materials was used. The sand/steel interface friction angle was taken from the literature as $0.66 \times \phi_{soil}$ and was distributed over 16.6% of the rigid wall surface area, while the sand/acrylic interface friction angle taken from the results of the interface direct shear test described in Chapter 5 ($\delta = 12^o$) and was distributed over the remaining surface area. The friction angle of the sand was determined from the triaxial test results presented in Chapter 5. As a result, the calculated interface friction angle adopted at the rigid wall was 18°.
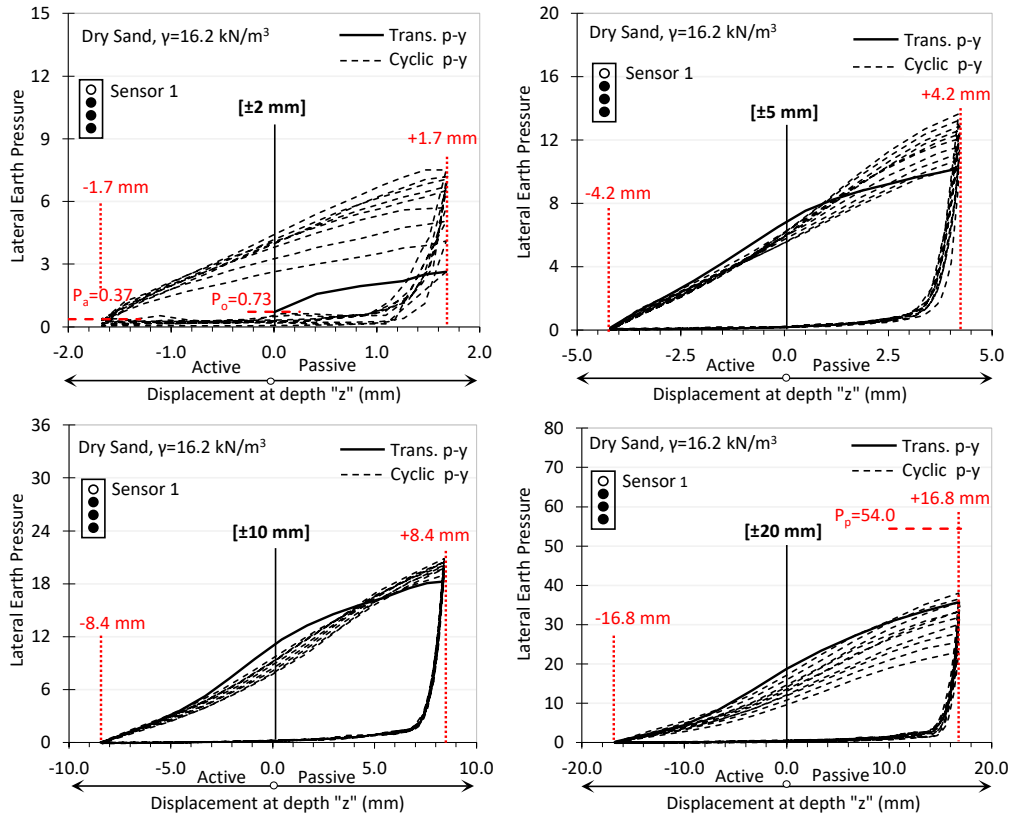
(a) Sensor 1



(b) Sensor 2

159
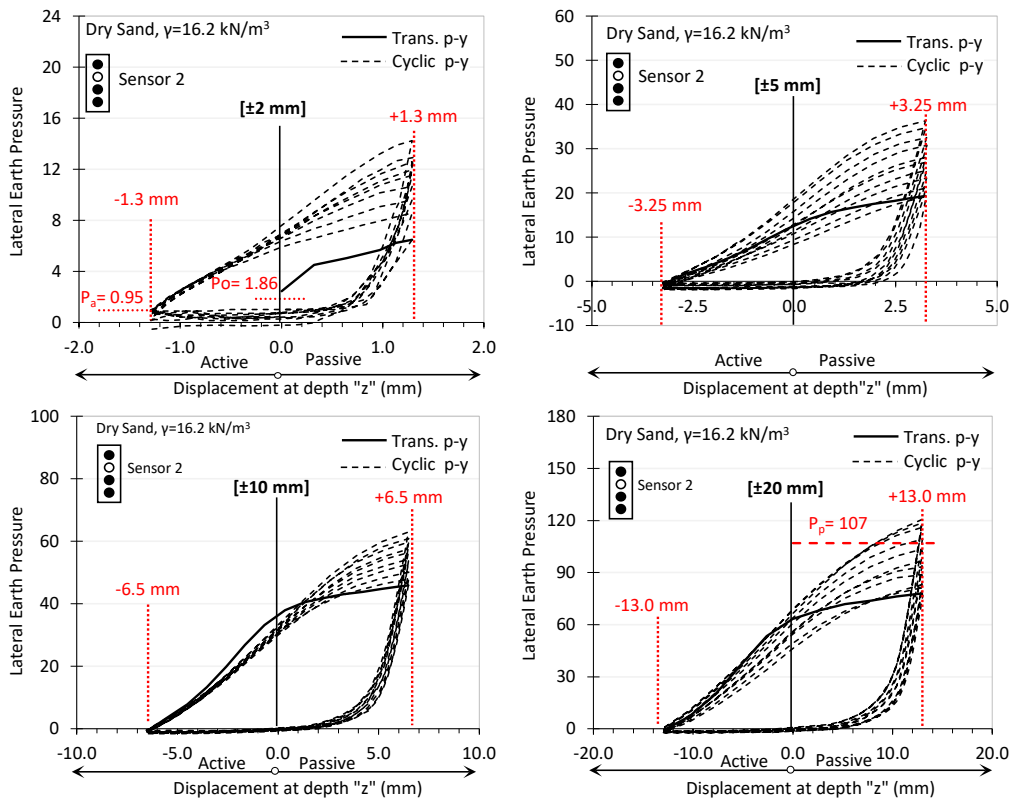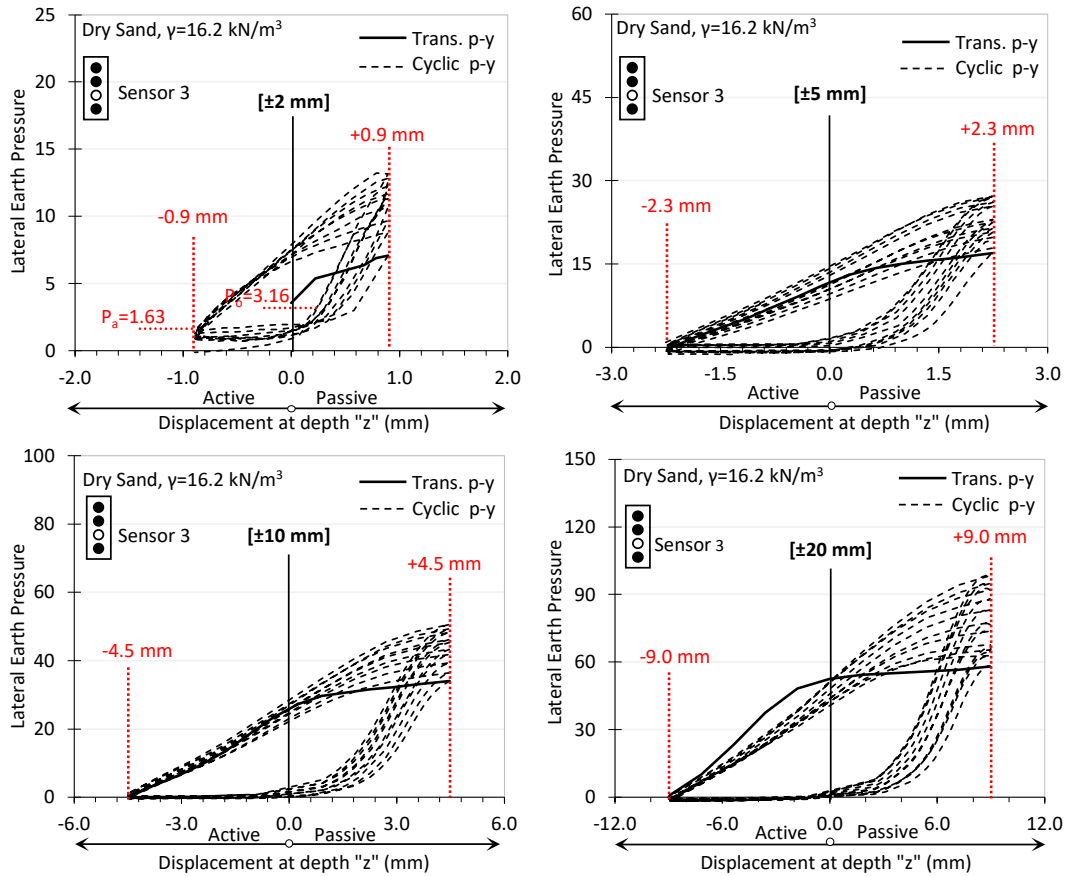
(c) Sensor 3

Figure 7.2 P-y response due to cyclic loading for Sensors #1, #2, and #3 for the case of medium-dense soil

Comparison with the active experimental response is shown at the lower cyclic amplitudes (2mm) while comparison with the passive response is shown at the highest cyclic amplitudes (20mm). The active pressures recorded for the first cycle indicate an acceptable level of agreement with Coulomb's theory. However, with increased number of cycles, the predicted active pressures overestimate the measured values. This is expected given that densification of the soil is expected to occur in the sand with repeated cyclic loading and unloading.

The passive pressures at limit state as predicted by the log-spiral method proposed by Lui et al. method are plotted on Figure 7.2 for the 20mm displacement cycle. Results show that the lateral stresses measured by Sensors #2 was the only sensor to have its peak pressures approach the limit-state passive pressure after several cycles. As for the rest of the sensors, their peak pressures fell shy of the limit state pressures. At Sensor #3, the calculate limit state pressure was located outside the figure scale and therefore could not be presented on the figure.

A closer look at the cyclic p-y response in Figures 7.2 leads to several interesting observations. First, the observed p-y curves that describe the response of the soil as the wall is moved in the passive and active directions are non-linear for all magnitudes of displacement intervals. This observation is in line with finite element results presented in Elchiti et al. (2017, 2018) for the active response. This indicates that simple elastic-perfectly plastic p-y models may not be representative of the actual lateral earth pressure response of sands during cyclic loading.

Second, the results point to the importance of cyclic loading on the overall p-y response. At any given wall displacement in the passive direction, the lateral stress behind the wall is found to increase incrementally following each cycle. This holds true for the pressures recorded at Sensors #2 and #3. Sensor #1, on the other hand, behaved distinctively from other sensors at large displacement intervals. At $\pm10$mm displacement interval, Sensor #1 maintained approximately the same peak pressures throughout the 10 cycles while at $\pm20$mm displacement interval, it experienced a drop in lateral pressures with increased number of cycles. This distinctive behavior is attributed to the low confinement depth at Sensor #1. It should be kept in mind that Sensor #1 is relatively shallow and is affected by the soil depression observed at the

161

surface of the soil during active displacement of large cyclic intervals (see Figure 7.3). The size of the cavity is mainly affected by the magnitude of the deformation of the wall with larger displacements leading to densification of the sand behind the wall leading to a larger cavity size. This phenomenon resulted in a decrease in the lateral pressure as recorded by Sensor #1 for the case of ±10mm and ±20mm displacement interval.

To illustrate the effect of cyclic loading on the lateral earth pressure, the first and last passive p-y curves of each interval are selected and plotted on Figure 7.4. The percent change in the peak lateral earth pressure is tabularized on each figure. The largest increases are noted for the cases of small displacement intervals (2mm and 5mm) which seem to benefit mostly from cycled loading. The improved p-y response as a result of cyclic loading for this medium dense sand may be associated with a process of densification of the sand with repeated loading cycles.



Figure 7.3 Soil cavity forming in front of the rigid wall during large active wall displacement
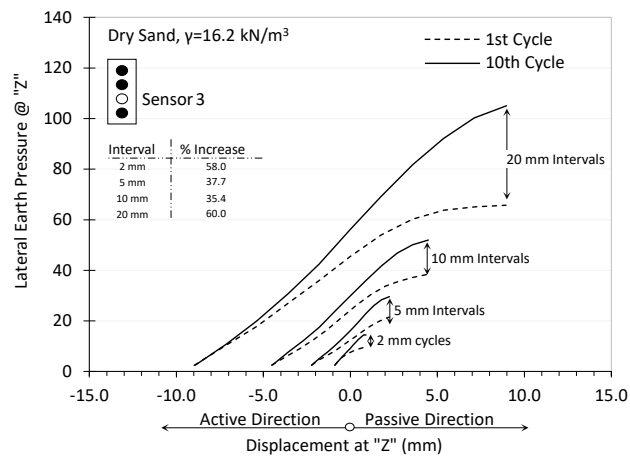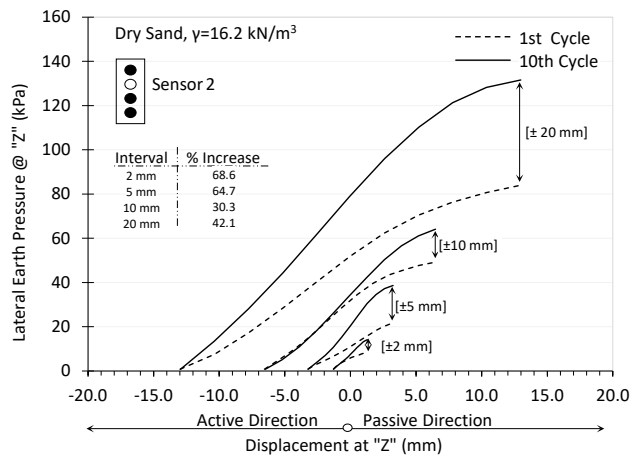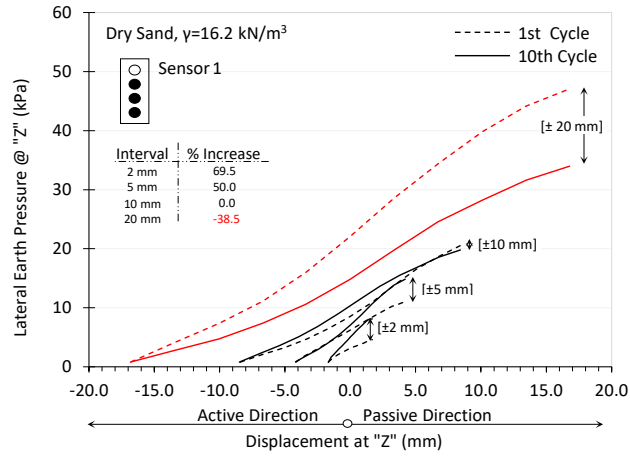
Figure 7.4 Passive p-y response recorded at 1st cycle vs. passive p-y response recorded at the 10th cycle

Third, an examination of the p-y response in the unloading portion of the p-y curves (passive side to active side) indicates that the lateral stress drops at a very fast rate as the direction of wall movement is reversed from passive to active. The rate of decrease in the lateral stress seems to be insensitive to the number of loading cycles and to the magnitude of the peak pressure. This can be observed by highlighting the remarkable consistency of the unloading sections of the p-y curves between cycles. The shape of the active section of the p-y curve is "hyperbolic" and consistent with numerically derived curves as reported in El-Chiti et al. (2018). The transition from the "passive" to the "active" side is characterized by an initial sharp decrease in lateral stress followed by a gradual reduction in stiffness leading eventually to the mobilization of full active conditions behind the wall. It is interesting to note that the wall displacement required for the lateral stress to reach active conditions increases as the range of the displacement interval increases. For instance, at the location of Sensor 2, the wall displacement needed to reduce the maximum pressure to the active limit state pressure increases from about 1mm for the 2mm displacement cycles to around 10mm for the 20mm displacement cycles.

Fourth, the results show a clear difference between the response of the transitional p-y curve (the first loading curve in a new displacement interval) and the rest of the curves. Transitional passive p-y curves show an approximate bi-linear p-y response (solid lines) while the rest of the p-y curves are represented by "s-shaped" curves. This difference in response could be attributed to the fact that the transitional p-y curve for any given interval is affected by the stiffness of the soil reached in the last cycle of the preceding interval (which has a smaller drift compared to that of the current interval).

The "s-shaped" p-y response that is observed in passive cycles following the transitional cycle seems to become more defined as the range of the cyclic wall displacement is increased from 2mm to 20mm. It can be noted that the first p-y curve that follows the transitional p-y curve experiences a drop in passive soil stiffness (compared to the transitional curve). After that, gradual increases in stiffness are observed in the passive p-y curves of consecutive cycles. This gradual increase in stiffness seems to decrease as the number of cycles increases. Convergence in the passive stiffness was observed at the terminal displacement cycles (9 and 10 cycles) for almost all displacement intervals.

The formation of "s-shaped" p-y curves in soil-structure-interaction problems that involve cyclic loading has been observed by others (Yankelevsky 1989). A typical s-shaped curve is shown in Figure 7.5a. Possible explanations for the formation of the "s-shaped" p-y response focus on the formation of three distinct zones of different soil densities just behind the moving wall (Figure 7.5b) as a result of cyclic movements. Zone 1 is a zone of loose soil formed by excess active wall movement in a previous unloading cycle. Excess active displacement denotes wall movement in the active direction beyond the displacement needed to mobilize the active limit state. Zone 1 contains soil of least density among the three zones. Zone 2 represents the soil affected by the loading/passive cycle of the previous interval and is expected to contain soil of the highest density among the three zones. Zone 3 represents soil that is being affected by the current interval displacement and contains a soil density equal to that of the undisturbed soil in the bed (initial density). As indicated in Figure 7.5a, the shape of each segment of the s-shaped curve can be attributed to straining soil in each of the aforementioned zones.
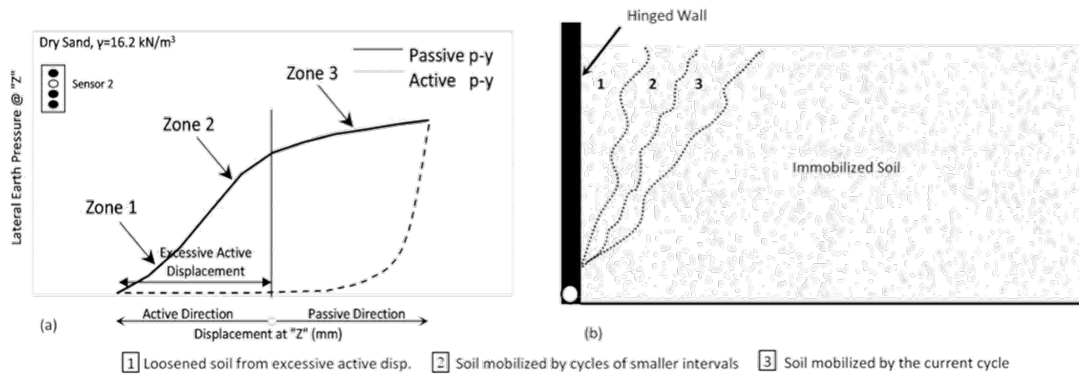
Figure 7.5 (a) Typical p-y curve (b) the formation of zones of different densities behind the wall as a result of cyclic loading

It is worth noting that the reduced stiffness that is exhibited in the transitional p-y curve could be explained by the shifting of zone 3 to new regions of immobilized soil at the new drift level of wall displacement. This leads to the redefinition of zone boundaries resulting in a drop in passive soil stiffness in the following p-y curve. As for the rest of the passive p-y curves, a gradual increase in stiffness with each cycle is recorded due to densification as indicated previously.

### E. P-Y Response at Large Displacements

At the end of the cyclic test, an additional large cycle was added to the experimental program. The top of the wall was displaced in the passive direction to the full stroke of the hydraulic piston, from a location of -20mm to +75 mm. The resulting p-y responses of the additional large displacement cycles are plotted on Figure 7.6. To place the additional large displacement within the context of the soil loading/unloading history, the p-y response of the 10$^{th}$ cycle for the case of $\pm 20mm$ displacement interval was plotted on Figures 7.6. Finally, the passive limit-state pressure using log-spiral method as proposed by Lui et al. is also shown on the figure using a horizontal red line.

166
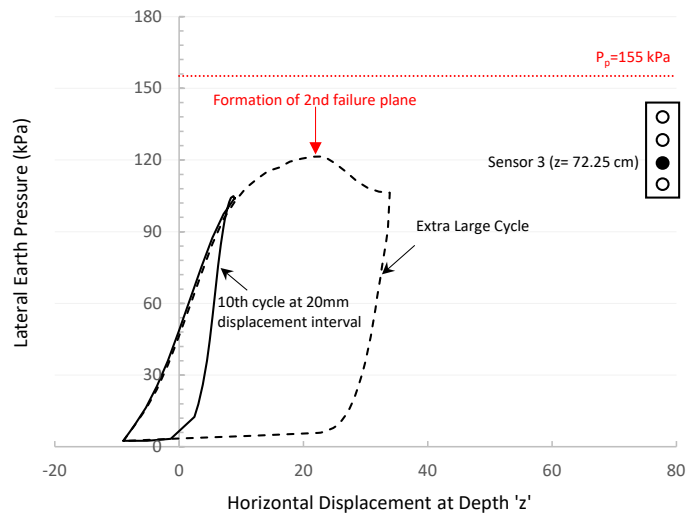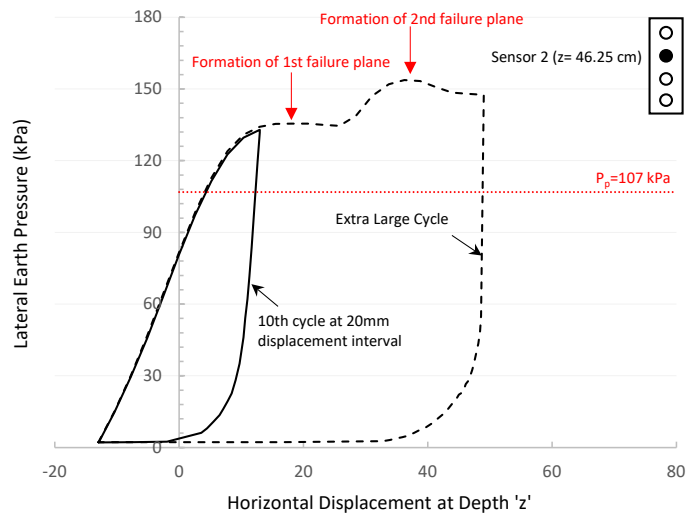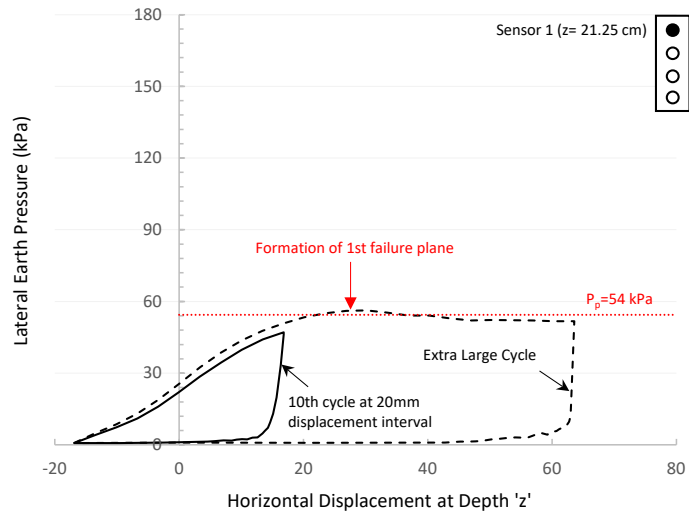
Figure 7.6 P-y response for the additional large displacement cycle
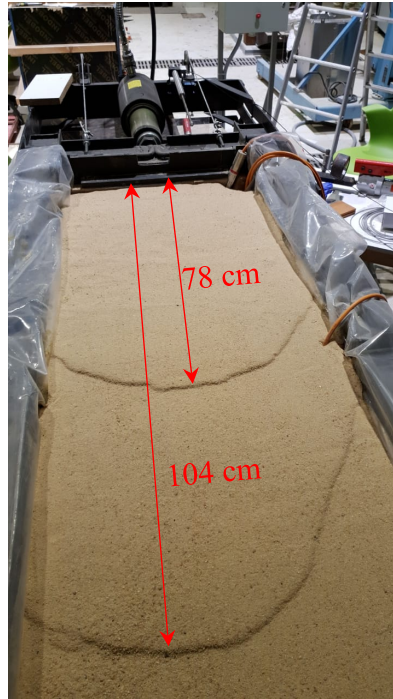
Figure 7.7 Formation of two failure planes during the additional large displacement cycle

An investigation of the data presented in Figure 7.6 indicates several interesting observations. First, the p-y response at all three sensors portrayed clear peaks followed by a strain softening. In the case of dry sand, strain softening following peak pressures are indicative of dense sand. The densification of the soil bed most probably occurred in the sand bed as a result of the previous loading cycles.

Second, the double hump shaped p-y response recorded at Sensor #2 could be explained by the formation of two failure planes in the soil bed as shown on Figure 7.7. The 1st failure plane was observed when Sensor #1 recorded its peak lateral pressure. At that wall displacement, Sensor #2 was in a state of stable lateral pressure. With additional top wall displacement, the lateral pressure at Sensor #2 accrued more pressure resistance indicating that the 1st failure plane did not fully encompass Sensor #2. The lateral pressure at Sensor #2 continued to rise until a 2nd failure plane formed at

the soil surface. The $2^{nd}$ failure plane was observed at the same time when Sensors #2 and #3 were registering their peak pressures. This implies that the $2^{nd}$ failure plane was much deeper than the $1^{st}$ failure plane.

Finally, the log-spiral limit-state passive pressure as proposed by Lui et al. agreed well with the soil response measured at Sensor #1. However, at Sensor #2 and #3, the theory either underestimated or overestimated the peak pressures. It should be noted that the Lui et al. theoretical pressures that are reported in Figure 7.7 were calculated assuming friction angles that are consistent with the density of the sand prior to cyclic loading. The friction angle is expected to change as the density in the bed changes during cyclic loading. This is not reflected in the Liu et al. pressures presented in Figure 7.7.

To  assess the impact of cyclic loading on the p-y response, the percent increase in the maximum passive stresses between the first and last ($10^{th}$) loading cycle in each wall displacement range was computed and plotted in Figure 7.8 as a function of the number of cycles. Three plots are presented on Figure 7.8, one for each sensor. The plots are color coded to denote the different interval displacement. The importance of this plot lies in quantifying the increase in the peak passive pressures after each cycle and in assessing whether an upper limit for the increase in peak passive pressure was attained after 10 cycles.

As shown by Figure 7.8, none of the plots reached a constant increase in peak pressure within 10 cycles. This implies that either more cycles are needed for this purpose or a peak pressure may not be attainable due to the changes occurring in the soil property after each cycle. For all sensors, the smallest displacement interval, $\pm2mm$,

was the one that benefited the most from cyclic loading. The decrease in peak pressures observed at Sensor #1 for the larger displacement interval is attributed to the cavity formed at the front of the wall as discussed earlier in this chapter.
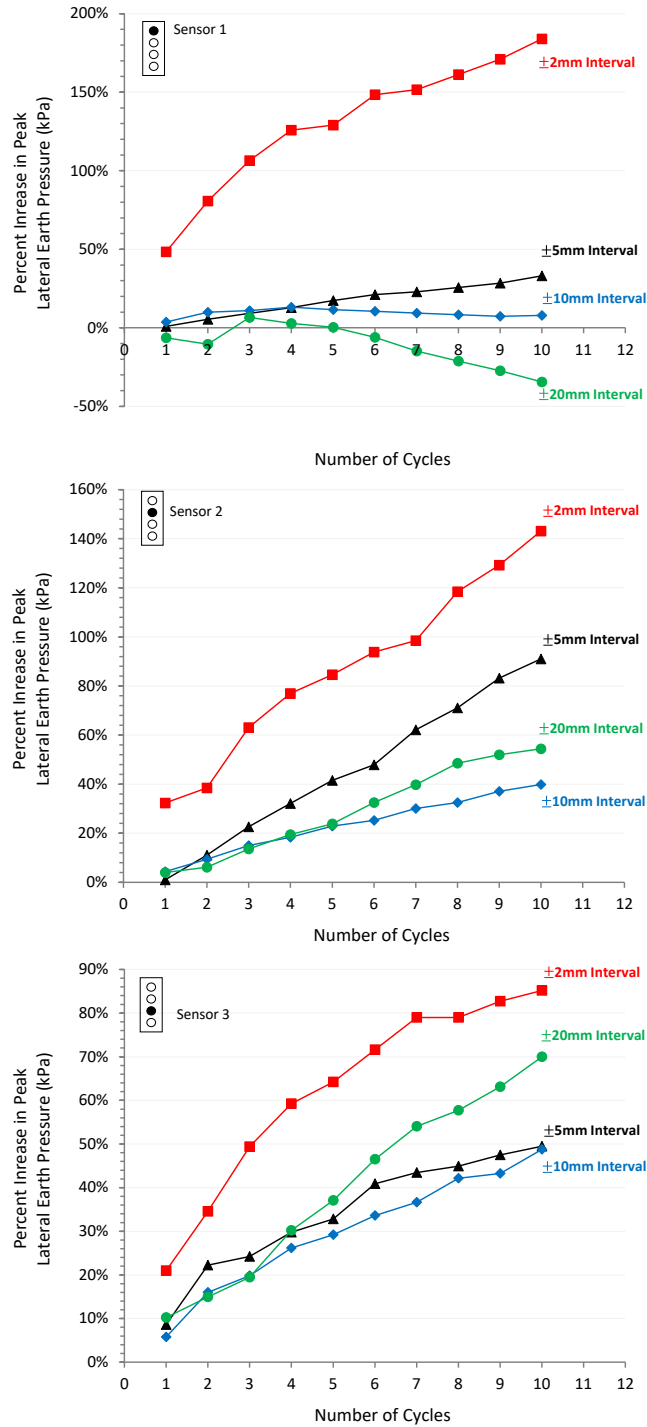


Figure 7.8 Percent increase in peak pressures for different wall intervals

## F. Sidewall Interface Friction Angle

The inner side walls of the tank were covered with grease coating and a plastic wrap to minimize the interface friction between the inner faces of the side walls and the sand. As the wall is displaced, the friction stresses, mobilized between the side wall and the sand, are measured using the custom-made friction sensor (refer to Chapter 5). Along with the force sensor that is placed at the same elevation but on the opposite wall, the friction sensor and the force sensor were used to back-calculate the interface friction angle between the wall and the soil. Figures 7.9 shows the back-calculated interface friction angles measured during the passive displacement of the wall for the case of medium-dense sand. Only the $\pm$5mm, $\pm$10mm, and the $\pm$20mm displacement intervals were used in the presentation of the data. The interface friction angles calculated during $\pm$2mm displacement interval were too small to be presented on the figure. Each displacement interval is color coded and specifically marked. All 10 cycles are plotted on the figure.

The results indicate that the mobilized friction angle increases as the wall is pushed in the passive direction reaching a maximum value of 2.6°. This value is relatively small demonstrating that the technique used to minimize the interface friction at the sidewall using grease covered with thin plastic sheet was successful. Reducing the interface friction on the side walls minimizes the impact of the boundary conditions on the lateral earth pressures that are measured by the pressure sensors in the middle of the wall at different depths. Minimal side friction will ensure that the measured lateral earth pressures are more or less indicative of the plain strain conditions that are typically encountered in practical basement/retaining walls.

A more detailed investigation of the data presented on Figures 7.9 indicates that the interface friction angle for all the interval displacements showed a trend whereby the interface friction angle at any given wall displacement decreased slightly with increasing number of cycles. This is most probably caused by the densification process occurring in the retained soil which results in larger Poisson ratio and finally with larger normal stresses at the sidewalls. Since the interface friction angle and normal stress are inversely related to each other, lower values of the interface friction angle result from higher values of normal stress.
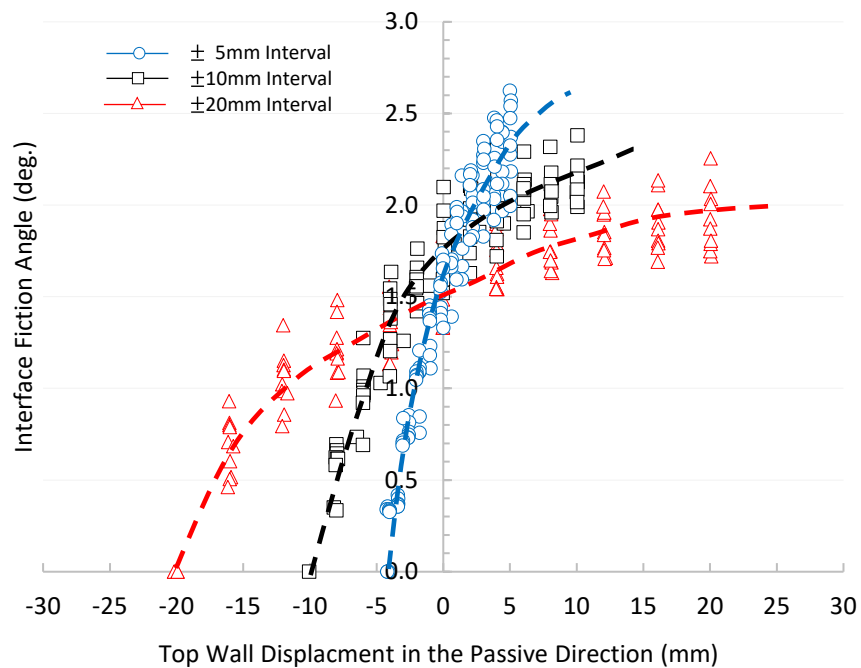
Figure 7.9 Sidewall interface friction angle for medium-dense sand subjected to cyclic loading

### G. Comparison with Loose and Dense Soil Subjected to Cyclic Loading

In 2020, a study was presented by Joseph Ghanem as part of his master's program that entailed the determination of cyclic p-y curves for loose and dense sand using the same material and test setup adopted in the present study. The density of the backfill materials used was 1550 kg/m$^3$ for loose sand and 1750 kg/m$^3$ for dense sand. A comparison between the maximum passive pressures that were measured at the end of each loading cycle for the different relative densities is presented in Figure 7.10. All responses follow the same increasing trend of passive pressure with cyclic loading. As expected, the passive lateral stresses that were measured in the case of the medium dense sand bed fell between the passive pressures measured for the cases of loose and dense sand as presented by Ghanem.

Interestingly, the maximum lateral stresses that were measured in the case of loose and medium-dense sand were close to each other at Sensor #1 (z=21.25cm). For the deeper sensors, the maximum passive pressures were more systematically affected by increasing the sand density from 1550 to 1750 kg/m$^3$. This difference in the response observed at Sensor #1 may be related to slight differences in the testing procedure adopted between the current study and those used by Ghanem for the cases of loose and dense soil. As noted earlier, a cavity was formed in front of the rigid wall during the active wall displacement (Figure 7.3). The resulting effect was a slight decrease in passive earth pressures at Sensor #1 due to the undermining of the vertical stresses at that sensor. However, with the tests conducted by Ghanem, a decision was made to re-level the sand bed to 1.2m after the end of the 10 cycles in each cyclic displacement interval. This may explain the reason why the top sensor behaved similar to the other sensors in the experiments conducted for loose and dense sand.

173
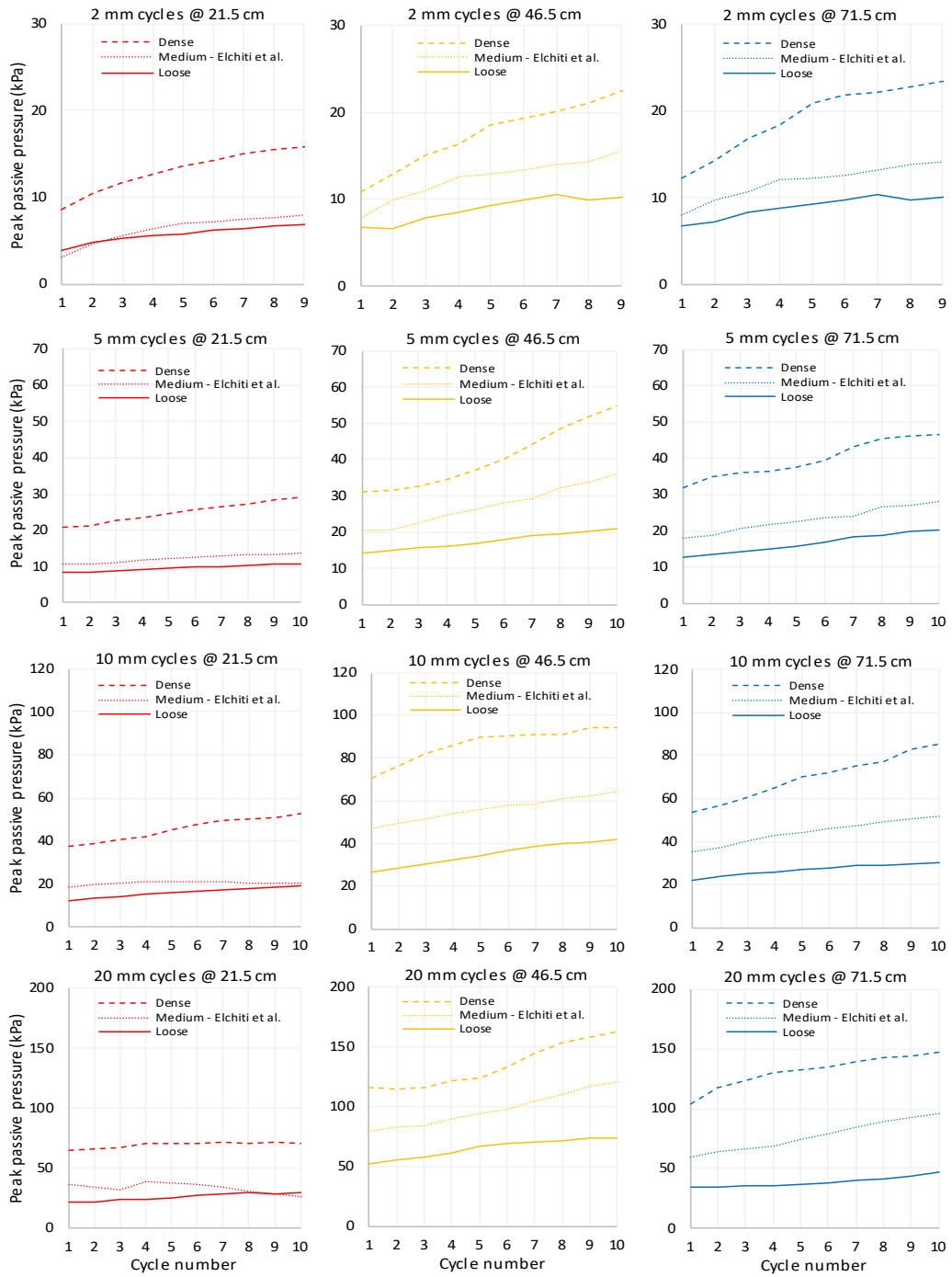
Figure 7.10 Peak passive pressures per cycle for the case of loose, medium-dense and dense soil

**H. Conclusion**

In this chapter, an experimental test setup was designed and constructed to measure the relationship between rigid wall movements and the mobilization of lateral earth stresses in the retained soil under cyclic loading conditions. This effort is the first in the literature and comes at a time when interest in applying the concept of p-y curves in the analysis of structures with basement walls is on the rise. Based on the cyclic p-y response of a wall supporting medium dense sand, the following conclusions can be made:

1. Cyclic p-y curves that represent the mobilization of lateral earth pressure behind the rigid rotating wall are highly nonlinear and cannot be adequately represented by the simple elastic-perfectly plastic model that was adopted in the literature in modeling soil-structure interaction between basement walls and sand backfill.

2. Due to a process of densification that must have dominated the volumetric tendency of the sand behind the wall during cyclic loading, the p-y curves showed a significant increase in the maximum pressure at the passive side after 10 loading cycles. An observation of the initial stiffness that characterizes the p-y response in the passive direction also showed a gradual increase in stiffness with consecutive loading cycles. This gradual increase in stiffness decreased with the number of cycles until convergence in the passive stiffness was observed at the terminal displacement cycles (9 and 10 cycles) for almost all displacement intervals.

3. Unlike the passive response, the p-y curves representing the unloading cycles (from passive to active) were insensitive to the cycled loading and showed remarkable consistency between cycles. However, it was observed that the

displacement required for the lateral stress to drop from passive to active during the unloading cycle increased as the cyclic displacement interval increased.

4. The measured p-y curves for loading in the passive direction portrayed an "s-shaped" response which was previously noted by others in the literature. The "s-shaped" response was mapped to the formation of three distinct zones of different soil densities just behind the moving wall. Zone 1 is a zone of loose soil resulting from a previous unloading cycle. Zone 2 represents the soil affected by the loading/passive cycle of the previous interval and Zone 3 represents soil that has not been affected by the current interval displacement and contains a soil density equal to that of the undisturbed soil in the bed (initial density).

The hypothesis of the zonation behind the wall has to be verified in the future with experimental tests that allow for monitoring the development of strains behind the wall possibly using PLEXI-glass side walls. Alternatively, the hypothesis could be verified using numerical simulations.

# CHAPTER 8

# CONCLUSION

**A. Research Context and Summary**

P-y curves have been widely used in the analysis of piles under lateral loads. However, the use of p-y curves for the analysis of rigid walls is still in its early stages. There is a need for realistic and simplified models that could describe the p-y relationship for rigid walls to be used as input in robust soil-structure-interaction problems in the context of performance-based design. The proposed dissertation aims explicitly at satisfying this need. The study consists of two parts.

1. Investigate and determine the non-linear p-y response for granular soils supported by full-scale rigid walls using the finite element method. An expression for the backbone model is proposed that takes into account the effect of the wall height, soil properties (relative density, soil friction angle, and the modulus of elasticity), wall friction, and confinement pressure.

2. Design and construct a laboratory-scale rigid wall prototype that could be used to measure the p-y response for granular soils under static and cyclic loading conditions. The wall, having a width of 0.5m and a height of 1.2m, will be hinged at its bottom and forced into rotation using a hydraulic piston applied at its top. Pressure sensors as well as LVDT's will be installed at necessary locations to record soil stresses and wall displacements at several depths. P-y curves for active, passive and cyclic motion will be determined, analyzed and compared to p-y curves found in literature.

**B. Research Conclusions**

Based on the numerical simulations conducted on PLAXIS 2D for the investigation of p-y curves for the case of rigid walls retaining granular soil, the following conclusions can be made:

1. The use of the Hardening soil model in the FE analysis resulted in p-y relationships that are reasonable.

2. P-y relationships were found to be sensitive to the depth below the ground surface $z$, the soil modulus $E$, the relative density, and the height of the wall $H_w$. The interface friction angle at the soil/wall boundary affected the p-y response for active wall displacement but had little influence on the p-y response of small passive wall displacement.

3. Results showed that the 1.3mm displacement criterion for active wall displacement and the 13mm for passive wall displacement that is typically referenced in the literature for the mobilization of active conditions in p-y curves is not realistic for full scale rigid walls.

4. For the case of active wall displacement, p-y relationship for a frictional wall could be derived from the p-y relationship of an identical non-frictional wall provided that the variation of the frictional shear stresses along the wall soil interface with displacement could be identified. A simplified hyperbolic expression was developed to model active p-y curves for non-frictional walls while a bilinear model was used represent the mobilization of the frictional shear stresses at the soil-wall interface $\tau_i$ with displacement.

5. For the case of passive wall displacement, a hyperbolic model that is based on the Ramberg-Osgood equation was used for the prediction of passive p-y response. The

equation is dependent on two parameters, namely the passive pressure at limit state and the initial stiffness, $C_o$. For calculating the passive pressure at limit state, the log-spiral method proposed by Liu et al (2017) was adopted since it was found to produce results that matched with acceptable accuracy the limit state values calculated by FE analysis. On the other hand, a simplified empirical model was derived to express the initial stiffness $C_o$ as a function of the depth below the surface, modified height of wall, and modulus of elasticity. The proposed hyperbolic model was shown to yield reliable predictions of the passive p-y response for all the cases analyzed in this study.

6. It is worth noting that the intent of this study is to provide a methodology for modeling p-y curves for cohesionless soils that are used as backfill behind rigid basement walls. In the finite element analyses that were conducted, the soil properties that were used pertain to those of Ottawa sand. As a result, the numerical results and the associated simplified model parameters are expected to be affected by the choice of the soil type used. Moreover, while the choice of the hardening soil model is adequate for loose and medium dense sands that do not exhibit significant post-peak softening in the stress-strain relationship, its use is questionable for dense sands that exhibit significant dilation and softening at large strains. The use of the hardening soil model for dense sands is a limitation that needs to be investigated further in future studies.

Based on the results of three static tests (three relative densities) that were conducted by displacing the wall from its at-rest condition to an active condition, followed by passive loading up to a maximum wall displacement of 10% of the height of the wall (around 120 mm), the following conclusions can be made:

1. At-rest to active p-y curves are relatively curved with an observed decrease in the rate of stress loss with increased wall displacement. The measured p-y response is highly sensitive to the active wall displacement with a top wall displacement of -8mm being sufficient to reduce the lateral pressures from the at-rest pressure to active limit-state pressure at all sensors.

2. At-rest to passive p-y curves are characterized by a monotonic increase in lateral pressure with passive wall displacement. The responses are non-linear in shape with varying intensity depending on the location/depth of the sensor and the magnitude of applied displacement. Among the four sensors, only the upper sensor recorded stresses that reached passive conditions. The stresses in the deeper sensors showed no signs of asymptotic behavior due to the relatively small wall displacements that were not large enough to induce non-linearity in the p-y response. As a result, passive limit state was not reached in the deep sensors.

3. The effect of relative density on both the active and the passive p-y responses was significant. Loose sand was the slowest to approach the active limit-state, with the amount of wall displacement required to mobilize active conditions for the case of loose soil (3 to 4 mm) being approximately 3.5 times that for medium-dense soil and 8.0 times that of dense soil. On the other hand, the passive response indicated that denser soils tend to exhibit stiffer p-y responses compared to looser soils.

4. For all the cases tested, results indicated that the passive p-y curves proposed by Briaud and Kim prematurely predict the occurrence of passive limit-state. As an example, the experiment conducted on medium dense soil indicated that a wall displacement of more than y=70mm is necessary passive conditions to be achieved. This is much larger than the 13mm proposed by Briaud and Kim. The hyperbolic

model that was proposed in this dissertation based on the finite element analyses presented a better fit to the measured p-y response, though it tends to overestimate the passive pressure.

In addition to the static test, the p-y response of a rigid wall supporting medium dense sand subjected to cyclic loading was conducted. Based on the test results, the following conclusions can be made:

1. Cyclic p-y curves that represent the mobilization of lateral earth pressure behind the rigid rotating wall are highly nonlinear and cannot be adequately represented by the simple elastic-perfectly plastic model that was adopted in the literature in modeling soil-structure interaction between basement walls and sand backfill.

2. Due to a process of densification that must have dominated the volumetric tendency of the sand behind the wall during cyclic loading, the p-y curves showed a significant increase in the maximum pressure at the passive side after 10 loading cycles. An observation of the initial stiffness that characterizes the p-y response in the passive direction also showed a gradual increase in stiffness with consecutive loading cycles. This gradual increase in stiffness decreased with the number of cycles until convergence in the passive stiffness was observed at the terminal displacement cycles (9 and 10 cycles) for almost all displacement intervals.

3. Unlike the passive response, the p-y curves representing the unloading cycles (from passive to active) were insensitive to the cycled loading and showed remarkable consistency between cycles. However, it was observed that the displacement required for the lateral stress to drop from passive to active during the unloading cycle increased as the cyclic displacement interval increased.

4. The measured p-y curves for loading in the passive direction portrayed an "s-shaped" response which was previously noted by others in the literature. The "s-shaped" response was mapped to the formation of three distinct zones of different soil densities just behind the moving wall. Zone 1 is a zone of loose soil resulting from a previous unloading cycle. Zone 2 represents the soil affected by the loading/passive cycle of the previous interval and Zone 3 represents soil that has not been affected by the current interval displacement and contains a soil density equal to that of the undisturbed soil in the bed (initial density).

# REFERENCES

Allotey, N. (2007). Nonlinear Soil-Structure Interaction in Performance-Based Design [Doctoral dissertation, University of Western Ontario, Canada].

Allotey, N., & El Naggar, M. H. (2007). Generalized dynamic non-linear winkler model of soil-structure interaction analysis. *Canadian Geotechnical Journal, 45*(4), 560-573.

Allotey N., El Naggar, M. H. (2008). A numerical study into lateral cyclic nonlinear soil– pile response. *Can Geotech J, 45*(9), 1268–81.

American Petroleum Institute. API Recommended Practice for Planning, Designing, and Constructing Fixed Offshore; 1993.

Badoni, D., & Makris, N. (1988). Nonlinear response of single piles under lateral inertial and seismic loads. *Soil Dyn Earthq Eng*, *15*(1):29–43.

Bathurst, R. J., & Benjamin, D. J. (1988). Preliminary Assessment of Sidewall Friction on Large-Scale Models in the RMC test Facility. *The Application of Polymeric Reinforcement in Soil Retaining Structures,* 181-192.

Boulanger, R. W., Curras, C. J., Kutter, B. L., Wilson, D. W., & Abghari, A. (1999). Seismic soil-pile-structure interaction experiments and analyses. *Journal of Geotechnical and Geoenvironmental Engineering, 125*(9), 750-759.

Briaud, J.-L. K.-K. (1998). Beam-Column Method for Tieback Walls. *Journal of Geotechnical and Geoenvironmental Engineering, 124*(1), 67-79.

Brown, D. A., Morrison, C., & Reese, L. C. (1988). Lateral load behavior of pile group in sand. *Journal of Geotechnical Engineering, 114*(11), 1261-1276.

Chen, W. F. (1975). Limit analysis and soil plasticity. *Elsevier Science Publishers*, B.V., Amsterdam, the Netherlands.

Clough, G. W., & Duncan, J. M. (1971). Finite Element Analyses of Retaining Wall Behavior. *J. Soil Mechanics and Foundations Division, 97*(12), 1657-1673.

Coulomb, C. A. (1776). An attempt to apply the rules of maxima and minima to several problems of stability related to architecture. *Mémoires de l'Académie Royale des Sciences*, **7,** 343-382.

Das, B. M. (2004). *Principles of foundation engineering.* Pacific Grove, CA, Thomson/Brooks/Cole.

Dave, T. N. (2012). Assessment of portable traveling pluviator to prepare reconstituted sand specimens. *Geomechanics and Engineering, 4*(2), 79-90.

Duncan J. M., & Chang C. Y (1970). Non-linear analysis of stress and strain in soils. *Journal of Soil Mechanics and Foundations Division, 96*(5), 1629-1653.

Dunnavant, T. W., & O'Neill, M. W. (1989). Experimental p-y Model for submerged, stiff clay. *Journal of Geotechnical Engineering, 115*(1), 95-114.

Dutta, S., & Roy, R. (2002). A critical review on idealization and modeling for interaction among soil-foundation-structure system. *Computers and Structures*, *80*(20-21), 1579-1594.

Elchiti, I., Saad, G., Najjar, S. & Nasreddine, N. (2017). Investigation of Active Soil Pressures on Retaining Walls Using Finite Element Analyses. *Geotechnical Frontiers*, 159–169.

Elchiti, I., Saad, G., Najjar, S. & Alzoer, S. (2018). Numerically derived P-Y curves for rigid walls under active conditions. 9th European Conference on Numerical Methods in Geotechnical Engineering, Porto, Portugal, 25–27.

Elchiti, I., Najjar, S.S., Saad, G., and Sadek, S. (2019). Experimentally-derived cyclic p-y curves for rigid walls supporting granular backfill. *Proceedings of the seventh International Conference on Earthquake Geotechnical Engineering*, Rome, Italy.

El Ganainy, H. & El Naggar, M. H. (2009). Seismic performance of three-dimensional frame structures with underground stories. *Soil Dynamics and Earthquake Engineering, 29*(9), 1249–1261.

El Naggar, M. H., Bentley, K. J. (2000). Dynamic analysis of laterally loaded piles and dynamic p–y curves. *Can Geotech J, 37*(6):1166–83.

El Naggar, M. H., Novak, M. (1996). Nonlinear analysis for dynamic lateral pile response. *Soil Dyn Earthq Eng, 15*(4), 233–44.

Fang, Y. S., Chen, T. J., Holtz, R. D., & Lee, W. F. (2003). Reduction of Boundary Friction in Model Tests. *Geotechnical Testing Journal, 27*(1), 3-12.

Gade, V. K. (2016). Development of a Mechanized Traveling Pluviator to Prepare Reconstituted Uniform Sand Specimens. *Journal of Materials in Civil Engineering, 28*(2).

Saad, G., Saddik, F., & Najjar, S. (2012). Impact of soil structure interaction on the seismic design of reinforced concrete buildings with underground stories. In *Proceedings of the 15th World Conference on Earthquake Engineering*.

Hanna, A., & Diab, R. (2017). Passive earth pressure of normally and over-consolidated cohesionless soil in terms of critical-state soil mechanics parameters. *International Journal of Geomechanics, 17*(1).

Hanna, A., Rahman, F., & Ayadat, T. (2011). Passive earth pressure on embedded vertical plate anchors in sand. *Acta Geotechnica, 6*(1), 21-29.

Iannelli, M. (2016). *Determination of Seismic Earth Pressures on Retaining Walls through Finite Element Analysis*. [Master's Thesis, California Polytechnic State University].

Kerr, A. (1984). On the formal development of elastic foundation models. *Ingenieur-Archive, 54*(6)*, 455-464.

Kim, N.-K. B.-L. (1994). *A beam column method for tieback walls*. [Doctoral Dissertation, Texas A&M University].

Kramer, S. L. (1996). *Geotechnical earthquake engineering*. Prentice Hall, Upper Saddle River, NJ.

Kumar, J. (2001). Seismic passive earth pressure coefficients for sands. *Canadian Geotechnical Journal, 38***(4), 876-881.

Lancellota, R. (2002). Analytical solution of passive earth pressure. *Geotechnique, 52*(8), 617-619.

Finn, W. L. (2005). A Study of Piles during Earthquakes: Issues of Design and Analysis. *Bullet of Earthquake Engineering, 3*(2), 141-234.

Liu, S., Xia, Y., & Liang, L. (2018). A modified logarithmic spiral method for determining passive earth pressure. *Journal of Rock Mechanics and Geotechnical Engineering, 10*(6), 1171-1182.

Loukidis, D., & Salgado, R. (2011). Active pressure on gravity walls supporting purely frictional. *Canadian Geotechnical Journal, 49*(1), 78-97.

Maleki, S., & Mahjoubi, S. (2010). A New Approach for Estimating the Seismic Soil Pressure on Retaining Walls. *Scientia Iranica, 17*(4), 273-284.

Matlock, H. (1970). Correlations for Design of Laterally Loaded Piles in Soft Clay. *Proceedings of the 2nd Offshore Technology Conference*, Houston, 22-24 April 1970, 577-594. http://dx.doi.org/10.4043/1204-ms

Matlock, H., & Ripperger, E. A. (1956). Proceedures and intrumentation for tests on a laterally loaded pile. *Proceedings, Eighth Texas Conference on Soil Mechanics. Special Publication No. 29.* Texas: Bureau of Engineering Research.

Farrokh, N., & Whitman, R. (1983). Seismically Induced Movements of Retaining Walls. *Journal of Geotechnical Engineering, 109*(7), 915-931.

Paik, K. H., & Salgado, R. (2003). Estimation of active earth pressure against rigid retaining walls considering arching effects. *Geotechnique, 53*(7), 643-654.

PLAXIS 2D [Computer Software], (2018).

Ramberg, W., & Osgood, W. R. (1943). Description of Stress-Strain Curves by Three Parameters. Tech. Note 902, National Advisory Comm. Aeronaut., Washington, DC; 1943.

Randolph, M. F. (1981). Response of flexible piles to lateral loading. *Geotechnique, 31*(2), 247-259.

Rankine W. J. M. (1857). On the stability of loose earth. *Philosophical Transaction of the Royal Society London*.

Subba Rao, K. S., & Choudhury, D. (2005). Seismic passive earth pressures in soils. *Journal of Geotechnical and Geoenvironmental Engineering, 131*(1), 131-135.

Reese, L. C., Cox, W. R., & Koop, F. D. (1974). Analysis of laterally loaded pile in sand. *Offshore Technology Conference*, (pp. 473-483). Dallas.

Richard, R. J. (1999). Seismic Earth Pressure on Retaining Structures. *Journal of Geotechnical and Geoenvironmental Engineering, 125*, 771-778.

Saad, G., Najjar, S.S., & Saddik, F. (2016). Seismic performance of reinforced concrete shear wall buildings with underground stories. *Earthquakes and Structures*, 10(4), 965-988.

Sanchez-Salinero, I. (1982). *Static and Dynamic Stiffnesses of Single Piles*. Research Report GR82-31, University of Texas, Austin.

Scott, R. F. (1973). Earthquake-induced pressures on retaining walls. *Fifth World Conference on Earthquake Engineering* (pp. 45-54). Rome: California Institute of Technology.

Soubra, A. H., & Regenass, P. (2000). Three-dimensional passive earth pressures by kinematical approach. *Journal of Geotechnical and Geoenvironmental Engineering, 126*(11), 969-978.

Tabaroei, A. A. (2017). Comparison between Two Different Pluviation Setups of Sand Specimens. *Journal of Materials in Civil Engineering, 29*(10).

Tejchman, J., Bauer, E., Tantono, S. F. (2007). Influence of initial density of cohesionless soil on evolution of passive earth pressure. *Acta Geotechnica, 2*(1), 53.

Terzaghi, K. (1943). Theoretical Soil Mechanics. *John Wiley and Sons*, New York, 1943.

Wang, S., Kutter, B. L., Chacko, M. J., Wilson, D. W., Boulanger, R. W., & Abghari, A. (1998). Nonlinear seismic soil-pile structure interaction. *Earthquake Spectra, 14*(2), 377-396.

Wilson, D. W. (1998). *Soil-pile-superstructure interaction in liquifying sand and soft clay.* [Doctoral Dissertation, University of California, Davis].

Winkler, E. O. (1967). *Theory of Elasticity and Strength.* Prague: H. Dominicus.

Wood, John Holm (1973) Earthquake-Induced Soil Pressures on Structures. [Doctroral Dissertation, California Institute of Technology].

Wood, J. (1975). Earthquake induced pressures on a rigid wall structure. *Bulletin of New Zealand National Society for Earthquake Engineering, 8*(3), 175-186.

Yankelevsky, D. Z., Eisenberger, M., & Adin, M. A. (1989). Analysis of beams on nonlinear winkler foundation. *Computers & structures, 31*(2), 287-292.

Wu, G., & Finn, W. L. (1999). Seismic lateral pressures for design of rigid walls. *Canadian Geotechnical Journal*, *36*(3), 509–522.